Magnetic Trapping of Neutrons for Measurement of the Neutron Lifetime

A thesis presented
by

Sergei N. Dzhosyuk

to
The Department of Physics
in partial fulfillment of the requirements
for the degree of
Doctor of Philosophy
in the subject of

Physics

Harvard University
Cambridge, Massachusetts
May 2004

©2004 - Sergei N. Dzhosyuk

All rights reserved.

Thesis advisor
John M. Doyle

Author
Sergei N. Dzhosyuk

Magnetic Trapping of Neutrons for Measurement of the Neutron Lifetime

Abstract

An experiment to measure the free neutron lifetime using magnetically trapped neutrons is described. Neutrons are loaded into a 1.1 T deep superconducting Ioffe-type trap by scattering an 0.89 nm neutron beam in an isotopically pure superfluid ^{4}He bath cooled to below 300 mK. The neutron decays are detected by the scintillation light produced in the helium by the neutron decay products. The 0.89 nm neutron beam is produced by diffracting a cold neutron beam from a potassium intercalated graphite monochromator.

The measured trap lifetime at 300 mK and with no ameliorative magnetic ramping is substantially shorter than the free neutron lifetime. This is attributed to the presence of neutrons with an energy higher than the magnetic potential of the trap. Magnetic field ramping is implemented to eliminate these neutrons, resulting in an 833^{+74}_{-63} s trap lifetime, that is consistent with the currently accepted value of the free neutron lifetime.

An increase in the thermal upscattering rate is observed in the temperature range $0.5\ \mathrm{K} \leq T \leq 0.85\ \mathrm{K}$. A number of other systematic effects are studied.

Contents

Title Page i
Abstract iii
Table of Contents iv
Acknowledgments vi
Dedication viii

1 Introduction **1**
- 1.1 Neutron Beta Decay 2
  - 1.1.1 CKM Unitarity 4
  - 1.1.2 Big-Bang Nucleosynthesis 9
- 1.2 Ultracold Neutrons 12
- 1.3 Neutron Lifetime Measurements 13
- 1.4 Experiment Overview 19
  - 1.4.1 Magnetic Trapping 20
  - 1.4.2 UCN Production 22
  - 1.4.3 Decay Detection 24
  - 1.4.4 Limitations 26

2 Experimental Apparatus And Facilities **30**
- 2.1 Neutron Beam 31
  - 2.1.1 Apparatus Shielding 35
- 2.2 Neutron Monochromator 39
- 2.3 Monochromator Alignment 42
  - 2.3.1 Time-of-flight Setup 43
  - 2.3.2 Alignment Procedures 47
  - 2.3.3 Neutron Beam Filters 59
  - 2.3.4 Neutron Flux Measurements 61
- 2.4 Magnetic Trap 64
- 2.5 Cryogenic Apparatus 72
- 2.6 Detection System 88
  - 2.6.1 Material Selection for the Detector Insert 94

2.6.2 Detector Calibration Setup 97

3 Data Acquisition and Analysis 102
3.1 Experiment Control and Data Acquisition 102
3.2 Signatec Cards Data Analysis 112
3.3 KamFEE Card Data Analysis 119

4 Results and Discussion 122
4.1 Run Schedules and Data Sets 123
4.2 Backgrounds 126
4.3 300 mK Data 133
4.4 Phonon Upscattering 136
4.5 Magnet Ramp Runs 138
4.6 Natural Abundance Helium Runs 140
4.7 Gain Shifts 142
4.8 Ambient Gamma Background Monitoring 147
4.9 KAMFEE Card Data 152
4.10 Detector Calibration 155

5 Marginally Trapped Neutrons and Other Systematic Effects 159
5.1 Marginally Trapped Neutrons 159
5.1.1 Semi-stable Orbits 159
5.1.2 Confinement by the Material Walls 162
5.2 Other Systematics 167

6 Conclusions and Prospects 173
6.1 Summary of the Results 173
6.2 Future Work 175

Bibliography 182

A Superthermal UCN Production 192

B Beam Stop Activation 197

Acknowledgments

The completion of this work wouldn't have been possible without participation and support of many people.

Foremost, I thank my advisor, John Doyle, for his guidance during all these years in Graduate School and for creating such an extraordinary working environment. His approach toward solving problems, in Physics and in other areas of life, will always be an excellent example for me.

I am grateful to Paul Huffman, for his advice and help with many aspects of experimental physics. Many things that I have learned from Paul have been extremely helpful not only while working in the lab, but also during car repair and in many other situations. I also appreciate his efforts on editing this manuscript.

I feel honored for the opportunity to know and work with Robert Golub. His creativity, intellectual curiosity and breadth of knowledge deserve my utmost admiration.

I thank my former fellow graduate students, Clint Brome, Carlo Mattoni and Daniel McKinsey, with whom I spent so many days (and nights) working on the experiment. I am also very happy to have them as friends.

Special thanks are to Liang Yang who's contribution to this work is hard to overestimate. His talent, hard work, good-natured character and sense of humor made life during the last years truly a joy.

I appreciate the support of the members of NIST Neutron Interactions and Dosimetry Group and the NIST staff. In particular, Alan Thompson for his help with the data acquisition system and many other computer-related problems and Jeff Nico for his help with neutron flux measurements.

I appreciate the help of Bruce Berger in setting up the digitizing cards, Peter McClintock in preparation of the isotopically purified helium, Richard Pardo in measurements of the helium purity. I also thank Kyle Alvine, James Butterworth, Laurens van Buuren, Kevin Coakley, Antonio Copete, Klaus Habicht, Ekaterina Korobkina, Tomasz Kreft, Stephen Maxwell, and Robert Michniak for their contributions to the project and interesting discussions. Also, thanks to all those whose names are not mentioned but who contributed by their professionalism at work, or by making life enjoyable outside of the lab walls.

I am very grateful to my first Physics teacher, Dmitry Vlasov, for his encouragement and his devotion to teaching Physics.

Finally, I thank my parents and my sister. Although separated by distance, I always felt their love and support.

To my parents.

Chapter 1

Introduction

Since their discovery in 1932 by Chadwick [1], neutrons have been used in many applications in different fields of physics. The neutrons provide a valuable tool for examining the composition, crystallographic structure, and the thermal and magnetic properties of the materials. They also have become an object of intense study in themselves.

Neutrons are baryons and consist of one up quark and two down quarks. As the structure of the neutron is relatively simple compared to the structure of heavier nuclei, many properties of the neutron can be understood reasonably well using fundamental physics theory. The neutron can be used to test these fundamental physics theories and is particularly nice for this since in most cases the theoretical corrections required to extract theory parameters from the observations are fewer and smaller than those of more complicated systems. Specifically, the neutron lifetime, the subject of this work, in combination with other parameter(s) of the neutron decay, can be used to test the Standard Model, in particular Cabibbo-Kobayashi-Maskawa (CKM) matrix unitarity [2]. In addition, the neutron lifetime by itself plays a significant role in the predictions of the light element abundances from Big-Bang Nucleosynthesis (BBN) theory. Currently, the experimental precision in the neutron lifetime is the primary source of uncertainty in these predictions [3].

The neutron lifetime and other neutron decay parameters are under intense scrutiny to test the limits of the Standard Model and answer some of the most intriguing questions about the Universe. Similarly, the search for a neutron electric dipole moment [4] and time-reversal violating processes in neutron beta decay [5, 6] are aimed at finding CP-violation that may be relevant to the explanation of the baryon matter/antimatter asymmetry in the Universe. Finally, the search for the $n \rightarrow \bar{n}$ transitions serves as a test of $\Delta B = 2$ baryon number nonconservation [7].

1.1 Neutron Beta Decay

The free neutron is unstable. Once a neutron leaves the nucleus and is not subject to gluon exchange, the neutron decays into an electron, a proton and an antineutrino, releasing about 782 keV of energy

$$n \rightarrow p + e^- + \bar{\nu}_e + 782\,\mathrm{keV}.$$

This process is schematically shown in Figure 1.1. The currently accepted value of the mean lifetime of a free neutron is (885.7 ± 0.8) s [8].

In classical weak interaction theory, the Lagrangian density is [9, 10]

$$\mathcal{L} = -\frac{G_F}{2\sqrt{2}}(J_\mu J^{\mu\dagger}) + h.c.,$$

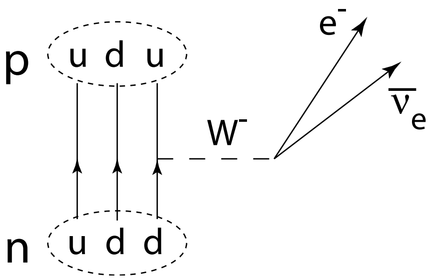

Figure 1.1: The beta decay of a neutron.

where G_F is the Fermi coupling constant and J_μ is the weak current that has both leptonic and hadronic components

$$J_\mu = j^l_\mu + j^h_\mu.$$

The leptonic part couples the leptonic doublets and has the form

$$j^l_\mu = \bar{e}\gamma_\mu(1-\gamma_5)\nu_e.$$

The hadronic part couples the quarks,

$$j^h_\mu = \bar{d}'\gamma_\mu(1-\gamma_5)u,$$

where d' is the weak eigenstate of the down quark. The weak quark eigenstates are related to the mass eigenstates by the Cabibbo-Kobayashi-Maskawa (CKM) mixing matrix,

$$\begin{pmatrix} d' \\ s' \\ b' \end{pmatrix} = \begin{pmatrix} V_{ud} & V_{us} & V_{ub} \\ V_{cd} & V_{cs} & V_{cb} \\ V_{td} & V_{ts} & V_{tb} \end{pmatrix} \begin{pmatrix} d \\ s \\ b \end{pmatrix}.$$

Due to the quark structure of the neutron and the proton, one may consider the most general Lorentz-invariance preserving form of the hadronic amplitude of the weak interactions, but in the framework of the V-A theory, only vector and axial vector components are present:

$$G_F\langle p\,|j^h_\mu|\,n\rangle = \bar{p}(g_V\gamma_\mu + g_A\gamma_\mu\gamma_5)n = V_{ud}G_F\bar{p}(\gamma_\mu + \lambda\gamma_\mu\gamma_5)n,$$

where $\lambda = g_A/g_V$ is the ratio of the axial vector and vector coupling constants. The Lagrangian density for the neutron decay is then

$$\mathcal{L} = -\frac{V_{ud}G_F}{2\sqrt{2}}\bar{p}(\gamma_\mu(1+\lambda\gamma_5))n\bar{e}\gamma_\mu(1-\gamma_5)\nu_e + h.c.$$

The neutron decay rate can then be expressed as [11]

$$\frac{d^3\Gamma}{dE_e d\Omega_e d\Omega_\nu} = \Phi(E_e)G_F^2V_{ud}^2(1+3\lambda^2)\Big(1 + a\frac{\vec{p_e}\cdot\vec{p_\nu}}{E_eE_\nu} + \vec{\sigma}\cdot\big[A\frac{\vec{p_e}}{E_e} + B\frac{\vec{p_\nu}}{E_\nu}\big]\Big),$$

where $\Phi(E_e)$ is a phase space factor, $\vec{p_e}$, E_e, $\vec{p_\nu}$, E_ν are the momenta and the energies of the electron and the antineutrino respectively, $\vec{\sigma}$ is the neutron spin. The asymmetry coefficients a, A, and B can be written in terms of λ:

$$a = \frac{1-\lambda^2}{1+3\lambda^2}, \tag{1.1}$$

$$A = -2\frac{\lambda+\lambda^2}{1+3\lambda^2}, \tag{1.2}$$

$$B = -2\frac{\lambda-\lambda^2}{1+3\lambda^2}. \tag{1.3}$$

A measurement of the neutron lifetime and one of the asymmetry coefficients provides information about both the vector and axial vector coupling constants g_V and g_A and can be used to calculate the CKM matrix element V_{ud}.

1.1.1 CKM Unitarity

In the assumption that there are only three generations of quarks, the CKM matrix must be unitarity. A unitarity condition, $|V_{ud}|^2 + |V_{us}|^2 + |V_{ub}|^2 = 1$, can be checked experimentally by measuring the individual elements of the matrix. Present values, quoted by the Particle Data Group [8] are:

$$|V_{ud}| = 0.9740 \pm 0.0008, \tag{1.4}$$

$$|V_{us}| = 0.2196 \pm 0.0026, \tag{1.5}$$

$$|V_{ub}| = 0.0038 \pm 0.0010. \tag{1.6}$$

They indicate that

$$\Delta_{CKM} = |V_{ud}|^2 + |V_{us}|^2 + |V_{ub}|^2 - 1 = -0.0032 \pm 0.0019, \tag{1.7}$$

2.2σ discrepancy from unitarity. Currently the CKM unitarity problem stimulates a great deal of activity on both experimental and theoretical fronts [2].

The uncertainty in $|V_{ud}|$, the largest element in the first row of the matrix, dominates the uncertainty in Eq. (1.7). The value of V_{ud} is proportional to the value of the vector coupling constant, $V_{ud} = g_V/G_F$, where $G_F = (1.16637 \pm 0.00001) \times 10^{-5}$ GeV^{-2} is the Fermi coupling constant known from muon decay [8]. The value of g_V can be obtained from superallowed $0^+ \rightarrow 0^+$ Fermi transitions, free neutron beta decay and pion beta decay. A comparison of the limits on g_V from different systems is shown graphically in Figure 1.2 and discussed in detail below.

Superallowed $0^+ \rightarrow 0^+$ nuclear beta decays at the moment yield the smallest experimental uncertainty, $V_{ud} = 0.9740 \pm 0.0005$ [12], but the magnitude of the theoretical corrections is substantial. The value of V_{ud} is obtained from the experimentally determined *ft* values of the various nuclei using [13]:

$$V_{ud}^2 = \frac{K}{2G_F^2(1+\Delta_R^V)(1+\delta_R)(1+\delta_{NS}-\delta_C)ft},$$

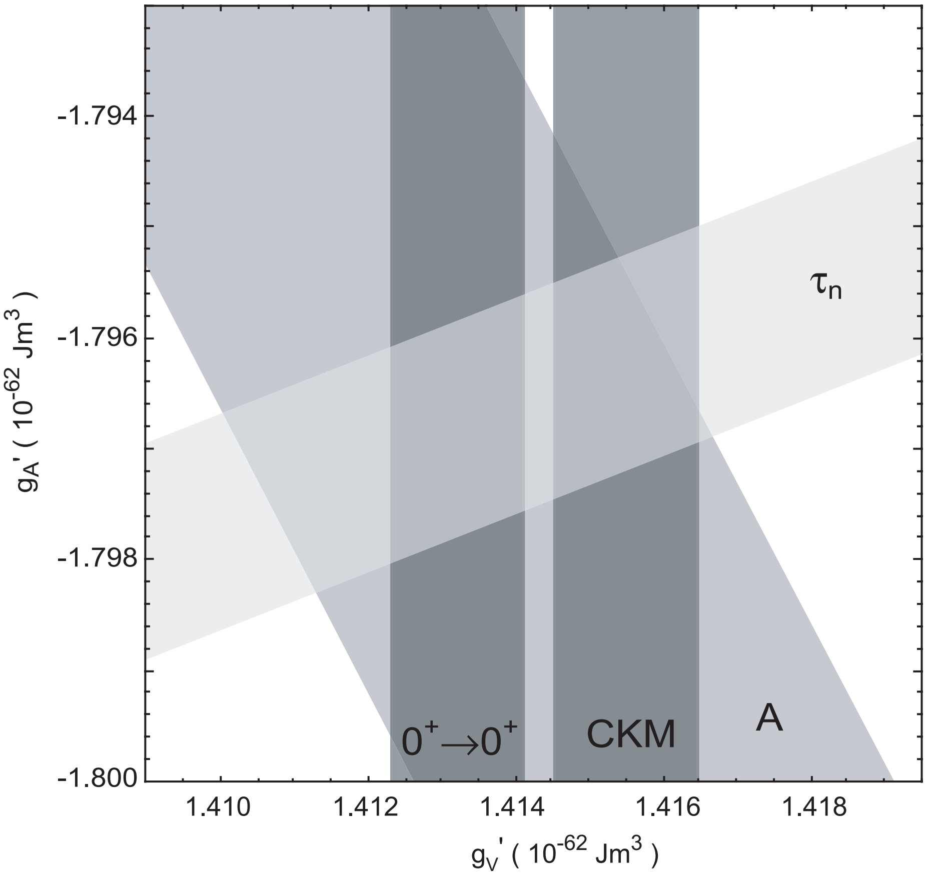

Figure 1.2: The experimental limits on g'_A and g'_V (see text for details) set by $0^+ \rightarrow 0^+$ Fermi transitions and neutron beta decay. The CKM unitarity condition is calculated from Eq. (1.7) in the assumption of $\Delta_{CKM} = 0$ and values of V_{us} and V_{ub} from Ref. [8]. The present limits for the pion decay are too large to fit on this graph.

where $K = 2\pi^3(\hbar c)^6\hbar \ln 2/(m_e c^2)^5$, f and t are the experimentally measured statistical rate function and the partial half life of the transition, δ_C is a isospin-symmetry breaking correction, Δ_R^V is a transition-independent radiative correction, and δ_R and δ_{NS} are both transition-dependent radiative corrections (δ_R is independent of the nucleus structure while δ_{NS} is structure-dependent) [12]. The *ft* values for nine isotopes spanning the range of masses from $A = 10$ to $A = 54$ are measured to better than 0.1 % and, after appropriate corrections, give consistent values of g_V as expected by the Conserved Vector Current (CVC) hypothesis. This also gives some confidence in the evaluation of the corrections, with typical values of $(\delta_{NS} - \delta_C) = (0.5 \pm 0.04)$ %, $\delta_R = (1.40 \pm 0.02)$ %, $\Delta_R^V = (2.40 \pm 0.08)$ % [12]. Nevertheless, due to difficulties in the estimates of the corrections, the Particle Data Group doubles the uncertainty in the estimates of the V_{ud} obtained from the nuclear $0^+ to 0^+$ beta decay data to 0.001 [8].

The theoretical uncertainties in V_{ud} calculated for the case of neutron beta decay are substantially smaller since the nuclear-structure dependent corrections are not needed. As was mentioned in Section 1.1, since neutron beta decay depends on both the vector and axial vector components. One thus needs to measure two parameters of neutron beta decay in order to determine both g_V and g_A. The spin-electron asymmetry coefficient A and the neutron lifetime τ_n presently provide the most stringent limits and are typically used for the estimates of V_{ud} [13]:

$$V_{ud}^2 = \frac{K/\ln 2}{G_F^2(1+\Delta_R^V)(1+3\lambda^2)f(1+\delta_R)\tau_n},$$

where δ_R is the nucleus dependent radiative correction, $\lambda = g'_A/g'_V$ is the ratio of the effective axial-vector and vector coupling constants measured experimentally[1] and Δ_R^V is a nucleus-independent radiative correction. The value of $f(1+\delta_R)$ is evaluated as 1.71489 ± 0.00002 [14].

The situation is somewhat complicated by the fact that the most recent measurement quoting the smallest error bar on the A coefficient [15] results in a value of λ that is 2.4σ different from the previous measurements [8]. Abele *et al.* [15] argue that their new measurement is more reliable since the total experimental corrections to

---

[1] $g_A^{'2} = g_A^2(1+\Delta_R^A)$, $g_V^{'2} = g_V^2(1+\Delta_R^V)$.

the raw data is 10 times smaller than that of earlier experiments. If one uses the new experimental result, the estimated value of the V_{ud} from neutron beta decay is $V_{ud} = 0.9713 \pm 0.0013$. Averaging all the previous measurements of the A coefficient, the Particle Data Group quotes $V_{ud} = 0.9725 \pm 0.0013$, in agreement with the $0^+ \rightarrow 0^+$ result.

Currently the uncertainty in the experimental value of A dominates the error in V_{ud} from neutron decay. An experiment using highly polarized ultracold neutrons to improve the measurement in A by a factor of 3 is currently on-line at Los Alamos National Laboratory. With these improvements, the uncertainty in the neutron lifetime will become the limiting factor in the evaluation of V_{ud}. With advances in the experimental measurements, Δ_R^V, currently contributing to the uncertainty of V_{ud} at the level of ± 0.0004, will become a limiting theoretical uncertainty.

Pion beta decay $\pi^+ \rightarrow \pi^0 e^+ \nu$ is a pure vector transition and allows one to extract $|V_{ud}|$ with combined theoretical corrections of about 3.3 % that are controlled to an uncertainty of smaller than 0.1 % [16]. Currently the experiments are limited by the experimental uncertainty due to the small branching ratio of the decay ($\approx 10^{-8}$). Using the result for the π_{e3} branching ratio from the PIBETA experiment [17], one obtains [18] $|V_{ud}|_\pi = 0.9716 \pm 0.0039$. As in the case of neutron beta decay, the pion beta decay result will be limited by the same theoretical uncertainty in Δ_R^V [13].

Since V_{us}, obtained from K_{e3} decays, is smaller than V_{ud} and has a quoted uncertainty low enough not to dominate the error in the CKM unitarity check, most of the efforts were turned towards improving V_{ud}. A recent result by the E865 Collaboration at Brookhaven [19] brought V_{us} back into the spotlight; the value obtained from this experiment gives V_{us} to 0.2272 ± 0.0030, different by about 2σ from the PDG value quoted in Eq. (1.5). Although this new measurement brings the CKM matrix into consistency with unitary, it raises questions of inconsistencies not only between the new and old K^+_{e3} results, but also between K^+_{e3} and K^0_{e3} data [18]. Several new K_{e3} decay experiments are currently underway to help resolve these inconsistencies [19].

The element V_{ub}, obtained from B meson decays, is small and is unlikely to play a major role in testing the CKM matrix unitarity.

To summarize, the question of CKM unitarity is still open and one needs to improve the uncertainty on both V_{ud} and V_{us} to clarify the current situation. The value of V_{ud} extracted from neutron beta decay is currently limited by the measurement uncertainties. Theoretical uncertainties, currently dominating the accuracy of the V_{ud} evaluation from the nuclear beta-decays, are smaller for the neutron decay. Thus the improvement in the measurements of the parameters of the free neutron beta decay will result in more stringent limits on CKM unitarity.

1.1.2 Big-Bang Nucleosynthesis

The neutron lifetime also plays an important role in the theory of Big-Bang Nucleosynthesis (BBN). Models of BBN predict the abundances of D, ^{3}He, ^{4}He and ^{7}Li several minutes after the Big Bang. The model predictions can be tested through comparison with present day observations[2]. Currently, the theoretical uncertainty in the calculations of the primordial abundance of ^{4}He is dominated by the uncertainty in the neutron lifetime [3].

---

[2] To measure the light element abundances close to their primordial values one usually seeks the sites with low heavy element presence since heavy element formation may alter the abundances [8].

During the initial stages of its creation, the Universe began expanding and cooling. Following the creation of the baryonic matter, the neutrons and protons are converted into each other through $\mathrm{n} \leftrightarrow \mathrm{p} + \mathrm{e}^- + \bar{\nu}$; $\mathrm{n} + \nu \leftrightarrow \mathrm{p} + \mathrm{e}^-$; $\mathrm{n} + \mathrm{e}^+ \leftrightarrow \mathrm{p} + \bar{\nu}$. As long as the rate of these reactions is greater than the rate of the expansion, the ratio of neutrons to protons is given by its thermal equilibrium value: $n/p = e^{-(m_n - m_p)/T}$. The interconversion rates become slower than the rate of expansion at a temperature $T \sim 0.8$ MeV and the neutron to proton ratio "freezes-out" at about 1/6 [20]. The neutron lifetime is used to normalize the weak reaction rates and thus to determine the moment when this "freeze-out" occurs [3].

Until the creation of deuterium begins through the reaction $p + n \rightarrow D + \gamma$, (about 3 minutes after the Big Bang)[3] neutrons beta decay at a rate of τ_n^{-1} and the n/p ratio drops to about 1/7. The creation of deuterium leads to the production of stable ^{4}He and currently most of the neutrons remaining in the Universe exist in the helium nuclei. Thus, the neutron lifetime comes in once again in the calculations of the n/p ratio and for the estimation of the ^{4}He abundance.

In addition to the ^{4}He abundance, one can study the abundances of the other light elements, such as D, ^{3}He and ^{7}Li. The abundances predicted by BBN depend on the baryon to photon ratio η. Due to the strong dependence of the deuterium abundance on η, the most stringent limits on η are provided by the observations of the abundance of this element (D) and, recently, by studies of the anisotropy of the Cosmic Microwave Background Radiation, especially by the WMAP mission. The results essentially agree, $\eta = (5.9 \pm 0.5) \times 10^{-10}$ [21] to $\eta = (6.8 \pm 0.4) \times 10^{-10}$ [22], for the deuterium

---

[3] Although the deuterium binding energy is roughly 2.2 MeV, due to the high photon to baryon ratio of $\sim 10^9$, the deuterium does not become stable against photodissociation until the temperature drops to about 80 keV [20].

measurements, (depending on the astrophysical site), and $\eta = (6.14 \pm 0.25) \times 10^{-10}$ [23] for CMBR anisotropy. The value of the parameter η can then be used to calculate the abundances of ^{4}He, ^{3}He, and ^{7}Li.

The calculated ^{4}He to Hydrogen ratio $Y_P = {}^4\mathrm{He/H}$, is $Y_P = 0.2491 \pm 0.0005$ [24]. The theoretical uncertainties in these calculations are less than 0.0002, with the uncertainties arising from the experimental uncertainty in the neutron lifetime, $\delta Y_P / Y_P = 0.8 \delta\tau_n / \tau_n$ [3], and due to the estimate of the baryon to photon ratio η. The calculated value of Y_P can also be used to constrain the effective number of light neutrinos during the BBN to $N_{eff,\nu} = 3.02^{+0.85}_{-0.79}$ [24], consistent with the value of 3 in the Standard Model.

Although the statistical uncertainty in recent direct measurements of Y_P is $\leq$ 1 %, the reported results are not statistically consistent, covering the range from $Y_P = 0.2452 \pm 0.0015$ [25] to $Y_P = 0.2391 \pm 0.0020$ [26]. The results depend on the treatment of various systematic corrections and the discrepancy between the results suggests that the systematics are larger than the quoted errors and need further explorations. Nevertheless, the estimate for the lower bound on the systematic error of $\sigma_{sys} \geq 0.005$ [27] brings the experimental observations of Y_P marginally into accordance with the calculated value.

The improvements in the measurements of the baryon to photon ratio from the data obtained by the Sloan Digital Sky Survey and by the planned Planck satellite mission [28] will make the neutron lifetime the leading experimental uncertainty in the ^{4}He abundance calculations.

1.2 Ultracold Neutrons

Neutrons with kinetic energy below $\sim 10^{-7}$ eV are called ultracold neutrons (UCN). Typical velocities of ultracold neutrons are below 5 m/s, corresponding to a wavelength of roughly 80 nm and a temperature of 1 mK. Such low velocities provide long interaction times of the UCN with matter and fields which greatly improves the accuracy of certain experiments. Excellent reviews of the history of UCN research, production methods and applications may be found in Refs. [29, 30].

The energy of an UCN is so small that it may experience total internal reflection from material walls, independent of the incident angle [31]. The interaction between UCN and the nuclei in materials may be described in terms of an effective potential:

$$V = \frac{2\pi\hbar^2}{m_n} N a,$$

where m_n is the neutron mass, N is the number density of the nuclei in the material, and a is the coherent scattering length of the bound atom. Values of the potential range from -48 neV for Ti to 335 neV for ^{58}Ni [30][4]. Total internal reflection of UCN from materials can be used to transport and then store neutrons in closed containers, one of the techniques used for measuring the neutron lifetime (see Section 1.3) and other parameters of neutron beta decay.

The strength of the interaction between UCN and the Earth's gravitational field is comparable to the effective potential for most materials; a UCN descending by 1 m gains roughly 102 neV in kinetic energy. The gravitational potential is often used to accelerate UCN and thus decrease the backscattering in UCN detectors and also to

---

[4] The high potential of ^{58}Ni makes this isotope an attractive material for the construction of the neutron guides (see Section 2.1).

make traps with open tops, where the neutrons are confined vertically by gravity.

The interaction between the neutron magnetic moment and an external magnetic field produces a potential energy equivalent to 60 neV/T. Thus, a magnetic field on the order of several Tesla can be effectively used as the walls of the material traps in terms of their ability to confine neutrons. The magnetic trapping techniques are described in more detail in Sections 1.3 and 1.4.

To date, most experiments with ultracold neutrons are limited by the available neutron fluxes. Although the interest in more intense UCN sources is unlikely to disappear, several new sources that are coming online or being proposed aim to increase the UCN densities by orders of magnitude [32, 33, 34, 35].

1.3 Neutron Lifetime Measurements

There are multiple experiments, some completed and others still in progress, that seek to measure the lifetime of a free neutron. The results of the experiments with quoted errors of less than 10 s are summarized in Figure 1.3.

The neutron lifetime experiments can be generally categorized into three types. The first type of experiments detects the neutron decay products from a cold neutron beam traversing a well-defined decay region. The time it takes for a neutron with the velocity v to pass through a region of length L is $t = L/v$. For a typical cold neutron beam ($\lambda \approx 0.4$ nm), and a typical trap length of 30 cm, t/τ_n is roughly 3×10^{-7}. Then the number of neutrons that decay in this region per second is $N_d = (t/\tau_n)\Phi$, where Φ is the number of neutrons entering the region per second. The value of Φ may be determined using a neutron monitor installed at the end of the flight path.

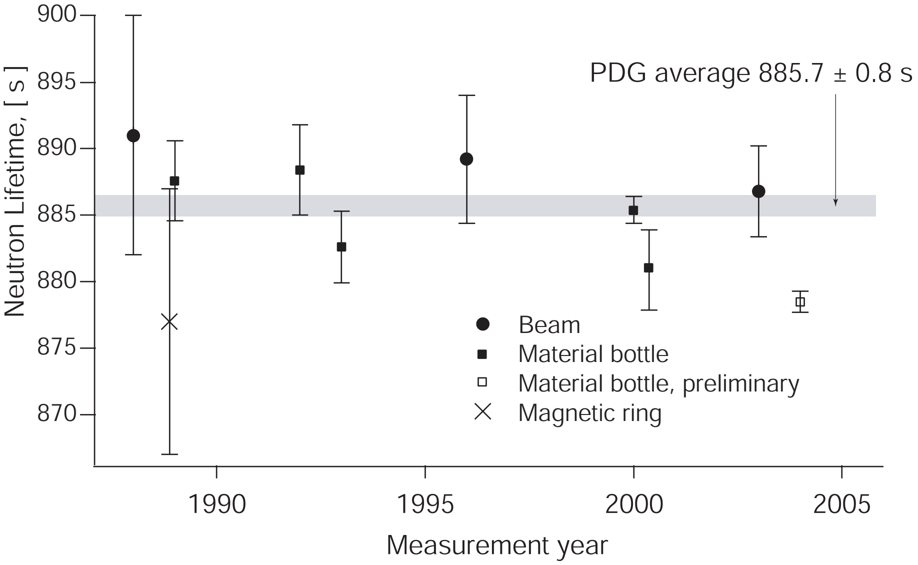

Figure 1.3: History of neutron lifetime measurements.

Since the neutron capture cross section is proportional to $1/v$, the neutron flux Ψ measured by a thin (small absorption) detector is $\Psi = \varepsilon\Phi/v$. Then

$$\tau_n = \varepsilon\Psi\frac{L}{N_d},$$

and thus one must measure the absolute values of N_d, ε, Ψ and L to determine τ_n.

In an experiment recently completed at NIST [36] (shown schematically in Figure 1.4), a Penning trap was been used to accumulate protons from neutron decays and then periodically release them. The released protons are accelerated by an electric potential and guided by a magnetic field into the proton detectors. This technique greatly increases the signal to noise ratio since the measurement time is decreased compared to the proton accumulation time. Great care must be taken to characterize the charged particle detectors because of the possibility of proton backscattering from the detector surface. The Penning trap is divided into identical sections so

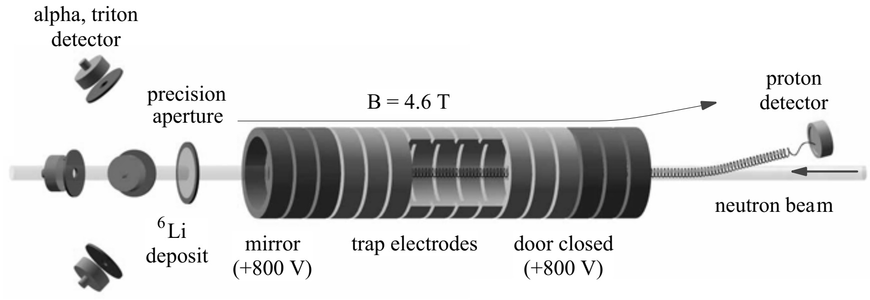

Figure 1.4: Schematic of the setup of the NIST neutron lifetime experiment. Details can be found in the text and in Ref [36]. Picture is courtesy of Fred Wietfeldt.

that it is possible to change the length of the trap and thus minimize systematic effects due to not well defined length of the trap. The current result of this experiment, $\tau_n = [886.8 \pm 1.2(\text{stat}) \pm 3.2(\text{syst})]$ s [36] is limited by the error in the neutron flux measurement that relies on the knowledge of the mass density of the ^{6}Li deposit. Although work calibrating the detector with a neutron radiometer [37] continues, measuring the neutron lifetime to below several seconds accuracy using the cold beam technique seems problematic.

A second type of experiments uses a storage bottle with material walls or a combination of material walls and the gravitational potential to confine ultracold neutrons. The bottle is typically filled with UCN from an external source and then after a fixed time, the number of UCN remaining in the bottle is measured by opening the counting the UCN with UCN detector. The population of neutrons in the trap changes because of neutron beta decay and losses due to collisions with the container walls. The measured bottle lifetime is thus

$$\frac{1}{\tau_{\text{bottle}}} = \frac{1}{\tau_n} + \frac{1}{\tau_{\text{loss}}}.$$

Neutron losses depend on the trap geometry, the wall materials, and the neutron energy spectrum. Thus the material selection for the walls of the bottle becomes extremely important. In addition to having high wall potential, the materials must have a very small neutron loss probability per bounce and have a form such that the container can be made to not have any gaps through which neutrons can escape. It has been determined that most materials exposed to atmosphere develop a layer of hydrogen on their surface that significantly increases the loss of UCN upon collisions with the surface. The history of the development of material UCN bottles, including different cleaning techniques and attempts to cool bottles to reduce thermal upscattering of UCN, is described in multiple texts (see for example Refs. [29, 30]). The majority of contemporary experiments that implement the material storage technique use a fully fluorinated polyether ($(F_3CCF_2OCF_2CF_5)_n$, also known as Fomblin) oil to cover the walls of the container.

In any case, the loss of UCN during storage is not a negligibly small correction and one must change the experimental conditions and extrapolate the value of the trap lifetime to the case of zero losses. One may change the geometry of the bottle to determine the trap lifetime at a different surface area to volume ratios and then extrapolate the result to the limit of an infinitely large trap [38, 39]. Since the energy spectrum of the neutrons inside the trap may also change over time, introducing a time-dependent loss rate, (neutrons with a higher kinetic energy collide with the walls more often and have a higher loss probability per bounce), several experiments apply procedures to “clean” the spectrum [39]. One approach is to place at some elevation inside the trap a material that absorbs or upscatters neutrons that have an energy high enough to reach this material [39]. In the ideal case, the kinetic energy of the neutron will be limited to the gravitational potential energy between the bottom of the trap and the absorber. Another method is to design the trap so that is open at the top to "spill" the energetic neutrons out [40]. One can vary the height of the opening by tilting the bottle. The extrapolation can then be made to the case of zero kinetic energy.

In the experiment currently quoting the smallest experimental error with a result of $\tau_n = (885.4 \pm 0.9_{\rm stat} \pm 0.4_{\rm syst})$ s [41], the upscattered neutrons are detected by external neutron detectors, to provide better control over UCN losses from the trap. This, however, requires knowledge of the relative efficiencies of the detectors, a parameter that in general is not easy to determine.

In all neutron lifetime experiments with material bottles the trap must be loaded with a consistent number of UCN with a consistent spectral density, since variations in the original population and spectrum may introduce errors in the measurements.

The number and magnitude of the corrections that must be made in order to extract the value of the neutron lifetime makes advancing the type of experiments using materially bottled neutrons very difficult.

A third type of measurements uses magnetic fields to confine neutrons. This technique eliminates the wall loses inherent in material bottles; the interaction of the neutron magnetic moment with the magnetic field gradient acts as a repulsive potential. The idea of confining neutrons in a magnetic field was proposed by Vladimirskiĭ in 1961 [42]. He also proposed several configurations of magnetic fields that can be used to confine neutrons, such as a straight-line current field, multipole traps, a toroidal trap and a "magnet mirror".

Several experiments have demonstrated or attempted to observe magnetic confinement of neutrons [43, 44, 45, 46]. One of the successfully completed experiments (Ref. [45]) utilized a toroid storage ring where collisions of orbiting neutrons with the walls of the apparatus were prevented by a sextupole magnetic field. In this configuration, however, the total kinetic energy of the neutron is larger than the magnetic potential depth and the neutrons can escape if their longitudinal momentum gets transferred into the transverse momentum. This effect, known as betatron oscillations, limited the accuracy of this experiment to 10 s [47].

In the experiment where a combination of magnetic fields and the gravity was used to confine neutrons [43] the potential of the trap was not high enough to trap more than 4 neutrons per loading cycle. In an early experiment [44], a spherical hexapole trap had a superfluid-helium-filled region where UCN were produced using the superthermal method. The temperature of the helium bath in this experiment, roughly 1.2 K, was high enough to cause large upscattering of the neutrons by phonons in the helium.

Magnetic trapping in a node-free Ioffe-type superconducting trap was demonstrated by our group in the year 2000 [46, 48]. One advantage of this technique is that spin-flip losses (Majorana transitions) are strongly suppressed due to the absence of zero-field regions in the trap. An overview of the experiment is given in Section 1.4. Significant progress has been made to both increase the number of trapped neutrons and decrease the backgrounds on the road towards improving the precision of the neutron lifetime measurement.

Magnetic trapping, although difficult experimentally, has smaller systematic errors as compared to the other methods. There are several groups pursuing ideas for constructing magnetic traps for neutrons, both with permanent [49] and with superconducting magnets [50, 51]. Although the effects of spin-flip losses, marginal trapping and loading efficiencies in these experiments should not be overlooked, the magnetic trapping technique now attracts a lot of experimental attention and appears to offer the best prospects for improving the accuracy in the neutron lifetime.

Consistency between values of the neutron lifetime obtained from the beam, material bottle, and magnetic trapping experiments, all with a different set of systematics, ultimately serves as a confirmation of the understanding and proper handling of an systematic errors and give us confidence in the obtained results.

1.4 Experiment Overview

One may create a magnetic field configuration that confines neutrons in space. If beta decay is the only escape process for the confined neutrons, then the population of neutrons inside a trap is decreasing exponentially as $N(t) = N(0)\exp(-t/\tau_n)$. If one uses a detector with an efficiency ϵ to observe the decay events then the detector counting rate will also be exponential: $N_d(t) = -\epsilon dN/dt = (\epsilon N(0)/\tau_n)\exp(-t/\tau_n)$. The value of τ_n can be extracted using a two-parameter fit to the experimentally observed counting rate $N_d(t)$, independent of the initial number of neutrons in the trap or the detector efficiency[5]. Although simple conceptually, the experiment poses many experimental challenges. The basic idea of the experiment was proposed in 1994 by Doyle and Lamoreaux [52]. The original apparatus used to demonstrate the

---

[5] The detection efficiency, however, must not change during the course of one measurement.

magnetic trapping is described in the Ph.D. thesis of Brome [53]. A new magnet, neutron monochromator and detection system are described in theses of Mattoni [54] and McKinsey [55].

1.4.1 Magnetic Trapping

A neutron has a magnetic moment. When placed in a magnetic field **B** it precesses around the local direction of the field with a Larmor frequency $\omega_L = \gamma B$, where $\gamma = 183$ MHz/T is the gyromagnetic ratio. A neutron moving in an inhomogeneous static magnetic field observes the time-varying magnetic field. However, if the rate of change of the field as seen by the neutron $|\dot{\mathbf{B}}|/B$ is much smaller than the Larmor precession frequency (the so-called adiabatic approximation), the magnetic moment will keep its orientation with respect to the field and the neutron energy in the magnetic field may be written as

$$E = E_{\text{kin}} \pm \mu |\mathbf{B}(r)|. \tag{1.8}$$

The inhomogeneous magnetic field acts like a potential for the neutron. A local magnetic field minimum presents a trapping potential for the low-field seeking spin-state, corresponding to the plus sign in Eq. (1.8).

The adiabaticity condition is violated in the regions where the magnetic field is close to zero (nodes of the trap). In these regions the neutron can spin flip and be ejected from the trap. The probability of these transitions goes as $\exp(-\pi\gamma B^2/\dot{B})$ [29] and becomes small in node-free trap configurations.

There are a number of configurations that can be used to a produce a magnetic field minimum in free space. Some of these are mentioned in Section 1.3 – straight-line

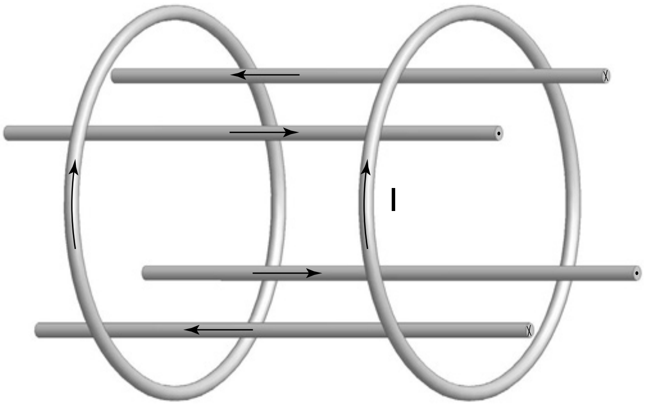

Figure 1.5: Conceptual drawing of an Ioffe-type trap.

current field, multipole traps, toroidal trap and the “magnet mirror”. In our work we use an Ioffe-type trap schematically shown in Figure 1.5. Four parallel current bars with an alternating direction of the current produce a quadrupole field that is linear in distance from the central axis of the trap $B(r) \propto r$. Two solenoids “close” the trap axially. The details of the construction of the magnet can be found in Section 2.4. The advantage of using an Ioffe configuration is that there are no zero-field regions in the trap, making spin-flips highly unlikely. The trap depth of our current trap is 1.1 T, corresponding to a potential of 66 neV. In current configuration, about 4000 UCN are confined inside a trapping of volume 1.5 liters. In a new trap design (see Chapter 6), it should be possible to increase the trap depth to 3.1 T and increase the size of the trapping region.

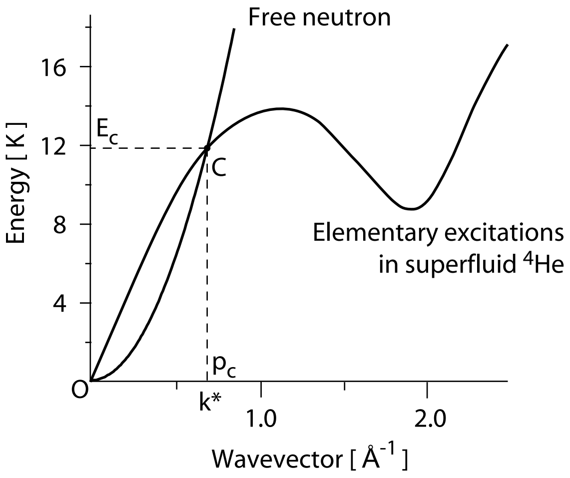

Figure 1.6: Spectrum of the elementary excitations in superfluid helium and the dispersion curve of a free neutron.

1.4.2 UCN Production

In order to become confined by the static magnetic field of the trap, neutrons must lose some of their energy inside the trap after penetrating the magnetic barrier. Without a mechanism for energy dissipation inside the trap, UCN with a "trappable" energy do not have enough energy to penetrate the magnetic potential from the outside. Neutrons that do enter the trap have enough energy to leave the trap as well. Neutron inelastic scattering in superfluid helium provides such an energy dissipation mechanism required for loading the trap.

The properties of superfluid helium can be explained in terms of the properties of "elementary excitations" [56] having the dispersion curve shown in Figure 1.6. The dispersion curves of the excitations and free neutrons ($E = p^2/2m_n$) intersect at two points: O and C. According to the momentum and energy conservation laws, the neutron with the momentum p_c and energy E_c may produce an excitation (phonon) in the helium with the same momentum and energy and scatter to near rest, becoming an UCN. The inverse process, the up-scattering of the UCN by the phonon absorption is suppressed by the Boltzman factor $\exp(-E_c/k_BT)$, where k_B is a Boltzman's constant and T is a temperature of the helium bath. This UCN production technique, proposed by Golub and Pendlebury [57], is called a superthermal UCN production as it can produce UCN density higher than implied by the Liouville's theorem. At temperatures below 0.9 K, the multi-phonon processes, involving the scattering of the phonons rather than their absorption, are dominating the UCN up-scattering in the helium. The total up-scattering rate is then proportional to T^7 [58, 59], and becomes about $10^{-5}\tau_n^{-1}$ at $T \approx 150$ mK [52].

The production of UCN by superthermal method was confirmed experimentally [60, 61, 46]. Most recently, the production of the UCN was measured as a function of the wavelength of the incoming neutron beam, exhibiting a strong peak in production at the wavelength of 0.89 nm corresponding to the energy E_c in spectrum in Figure 1.6 [62]. The contribution of the multi-phonon production depends on the spectrum of the incoming beam and was estimated at 25 % at the cold neutron guide at ILL, Grenoble. This result is in general agreement with the calculations [35] (see also Appendix A). In order to reduce the neutron-induced backgrounds we use a monochromator (see Section 2.2) to select only the neutrons in the wavelength band of 0.89 ± 0.02 nm. Although we lose the UCN that would be produced by the multi-phonon processes, the signal to noise ratio is improved by a factor of 30 [54].

In addition to ^{4}He, the natural abundance helium contains roughly 3×10^{-7} of ^{3}He isotope. Unlike the ^{4}He that does not absorb neutrons, the ^{3}He nucleus captures the neutron by $^3\mathrm{He}(n,p)^3\mathrm{H}$ reaction. The helium that fills the trapping region in our experiment is isotopically purified to have $^3\mathrm{He}/^4\mathrm{He}$ ratio of smaller than 2.5×10^{-13} (see Section 2.6).

The cryogenic environment also eliminates the impurities that can cause absorption of UCN in the trapping region – most materials become solid at liquid helium temperatures and precipitate on the walls.

In brief, the experiment works as follows. We fill the trapping volume with isotopically pure $^4\mathrm{He}$ that is cooled to below 300 mK by a dilution refrigerator. The magnetic trap is energized and the neutron beam enters the trapping region. The energy of the neutrons ($E_c \approx 12$ K) is much larger than the trap depth (0.8 mK) and neutrons easily penetrate the magnetic barrier. Most of the $\sim 10^8$ s^{-1} neutrons that enter the trap pass through the helium and are absorbed by the beam stop located at the end of the trapping region. About 2 % of the incoming 0.89 nm neutrons are scattering in the trapping region [63], and they are predominantly absorbed by the neutron shields. Fewer than ten neutrons per second are produced with the energy low enough to be trapped by the magnetic field, and only half of them is in the low-field seeking spin state. After roughly 4000 neutrons are accumulated in the trap, the neutron beam is blocked and the beta decays of the neutrons in the trap are observed.

1.4.3 Decay Detection

Generally, there are two basic approaches that can be used to measure the neutron decay rate. The “load and dump” approach involves loading the trap, waiting for certain period of time and then counting the number of neutrons left by emptying the trap. The other, “eyes open” approach uses the continuous detection of the decay events. The second approach has a benefit of being more sensitive to the detection of any deviation of the decay rate from an exponential. Such deviation may be an indication of the additional neutron loss mechanism from the trap. It is essential to identify and handle such effects properly in a precision measurement of the neutron lifetime.

The neutron decays can, in principle, be detected by observing the neutron decay products: electron, proton and antineutrino. Helium, in addition to its role as a UCN production media, serves as a scintillator for detecting the charged particles produced during neutron beta decay. The antineutrino escapes undetected due to its extremely small cross section for interaction with matter. More detailed description of the detector can be found in Section 2.6.

The electron and proton decelerate in the liquid helium, ionizing the helium atoms that then recombine to form the excited atoms and He_2 molecules. Within 10 ns the molecules in the singlet state undergo transition into the ground state with the emission of the UV photon with the wavelength of 60–100 nm. As much as 35 % of the energy of primary electron is emitted in UV, corresponding to roughly 22 UV photons per keV of primary electron energy. It is this burst of photons that serves as a signature of the neutron decay event inside the cell.

Due to the difficulties with the transmission of the UV from the trapping region into the light detectors (photomultiplier tubes) at room temperature, we use organic wavelength shifter, tetraphenyl tutadiene (TPB). A layer of TPB is evaporated onto a light reflecting Gore-Tex tube that is located inside the liquid helium and surrounds the trapping region radially. The UV light produced in the helium is converted by the TPB into visible light that subsequently passes through the optically clear neutron beam stop and is guided to the light detector through a series of acrylic light guides and windows. In order to reduce the backgrounds the light is split between two photomultiplier tubes and a coincidence between the tubes is required to acquire the signal from the PMTs. The acquired signal is then time tagged and is used to extract the time dependance of the neutron decay rate.

1.4.4 Limitations

Though the experiment offers many features that are extremely valuable experimentally such as elimination of the wall collisions and continuous detection, there are certain systematic effects and limitations that need to be considered.

Manufacturing of a large and deep magnetic trap is difficult. For a fixed trap geometry, the number of trapped neutrons goes as $B^{3/2}$, but the energy stored in the magnet and the forces on the magnet form scale as B^2. Currently the neutron trap designs are limited by the technology available for building the large quadrupole coils and the progress towards much larger traps will rely on the innovations that may occur in this field.

The production of UCN inside the detector region puts stringent requirements on the materials present in the cell. All materials need to be non-magnetic, compatible with low temperature environment, do not activate after neutron exposure and do not luminesce. After an extensive search we found a combination of materials that mostly satisfies the above mentioned criteria. Though we do have some neutron-induced luminescence and activation inside the cell, it is not effecting the results of the measurements at the current level of accuracy (~ 10 s). It may become an issue after the bigger trap is constructed and more precise measurements become possible. One might have to consider the alternative loading schemes in order to cope with the issue of the time-varying backgrounds produced by the neutron beam.

The properties of the liquid helium make it a good scintillating detector for the charged particles. The energetic electrons in the helium may be produced not only by the neutron beta decay, but also, for example, by the Compton-scattering of gammas. If the energy of the Compton electron is similar to the energy of the electron produced in the neutron beta decay, the gamma event is indistinguishable from the neutron event. Thus gamma shielding of the apparatus becomes essential. Currently the shielding is done by surrounding the apparatus with a layer of lead, but even with the shielding the backgrounds present the biggest impediment towards improving the statistics of the measurement.

Though we do not need to know the absolute detection efficiency to measure the neutron lifetime, the detection efficiency must remain constant during the course of one measurement. The gain of the PMT does drift with time, but this effect is small at the current precision level. However, it might become important as the precision of the measurements improves.

The isotopic purity of the helium on the level of $x = {}^3\mathrm{He}/{}^4\mathrm{He} \sim 10^{-15}$ is needed for the neutron capture on the ^{3}He to introduce the shift in the lifetime estimate on the order of $10^{-5}\tau_n$. The preliminary results from the accelerator mass spectroscopy measurements of the sample of helium used in our experiment gave a higher number,

$x \sim 10^{-13}$ [64]. Though the “heat flush” technique used for purifying the natural helium is believed to be able to produce helium with $x \sim 10^{-16}$ [65], the prevention of the cross-contamination of the “ultrapure” and natural helium is important.

There are neutron orbits in the magnetic trap where neutrons have energy higher than the magnetic trap depth, but are still confined by the magnetic field for an extended period of time. The loss of neutrons from these orbits by, for example, collisions with the walls, leads to the non-exponential decay of the neutron population in the trap and thus introduces an error in the estimates of the neutron lifetime. In addition, the surface of the detector acts as material wall for the neutrons that have energy higher than the trap depth (above-threshold neutrons). The probability of the neutron reflection from the wall depends on the material of the wall and the kinetic energy of the neutron at the moment of the collision, but in general may be very high (loss probability $\sim 10^{-5}$ per collision at the TPB coating of the detector). Thus, some neutrons are trapped by a combination of the magnetic potential and the material walls. The escape of these neutrons from the trap through the wall collisions, again leads to an error in the neutron lifetime estimates. In order to eliminate the above-threshold neutrons, one may lower the magnetic field of the trap by 50 % and then bring it up. The calculations show that this ramping, at least in the case of the sufficiently deep trap, completely eliminates the above-threshold neutrons, but also inevitably reduces the number of the neutrons that are trapped solely by the magnetic field (see Section 5.1.1). The current experimental data does not contradict these conclusions, but one will need to perform a series of ramps to get an experimental confirmations of these findings in the pursuit of a more precise measurement with a new setup.

The fact that the neutron decay occurs not in the vacuum but in the helium alters the neutron decay rate at a level of $10^{-5}\tau_n^{-1}$ [53], mostly due to the change in the phase space available for the decay products. The effect of the depolarization of the UCN on the electrons and triplet helium molecules that are present in liquid helium is also smaller than $10^{-5}\tau_n$ (see Section 5.2).

Currently the experiment is statistics-limited. The known systematic errors can be controlled at $10^{-5}\tau_n$ level.

Chapter 2

Experimental Apparatus And Facilities

This chapter describes the neutron production facilities and experimental apparatus used for neutron trapping. The neutron source and neutron transport from the source into the experimental area are described in Section 2.1. Section 2.2 discusses the design of the 0.89 nm neutron monochromator. The procedures implemented for alignment of the monochromator are given in Section 2.3. The superconducting magnetic trap is described in Section 2.4. Section 2.5 describes the cryogenic apparatus that houses the magnet and the detection cell. Details of the detection of the neutron beta decay events inside the trapping region and the detector itself are given in Section 2.6.

2.1 Neutron Beam

The neutron beam used in our experiment is provided by the National Institute of Standards and Technology (NIST) Center for Neutron Research (NCNR) 20 MW research reactor operating in Gaithersburg, MD. Neutrons are produced in the reactor core as a result of ^{235}U nuclear fissions and have energies of order 1 MeV. Following their release from the nuclei, they lose energy ("thermalize" to about 26 meV) by scattering in a heavy water (D_2O) bath surrounding the core of the reactor (26 meV corresponds to 300 K, temperature of the D_2O bath. A number of instruments at the NCNR make use of thermal neutrons for material studies and imaging [66]. An additional set of instruments utilize lower energy ("cold") neutrons since their longer wavelength ($\lambda \gtrsim 0.2$ nm) is better matched to the characteristic size of certain condensed matter systems. These cold neutrons are produced by scattering (and thus cooling) thermal neutrons by a liquid hydrogen-filled shell (the so called "cold source") [67] that is positioned next to the reactor core. The spectrum of neutrons exiting the cold source is roughly Maxwellian characterized by a temperature of 30 K. A cutaway view of the reactor with the cold source is shown in Figure 2.1. One unique feature of the NIST reactor is its split core – the fuel elements are located above and below, but not at the elevation level of the neutron beam ports. This allows for a large decrease in gamma background at the instruments without a large sacrifice in neutron flux.

A neutron guide is used to transport the neutrons from the cold source to the trapping apparatus, about 60 meters from the reactor. The NIST neutron guides are rectangular in cross-section and are made of 1 m long sections of ^{58}Ni-coated[1] glass

---

[1] The top and bottom plates are made of multilayered coating that has an effective reflection potential twice of the natural Nickel.

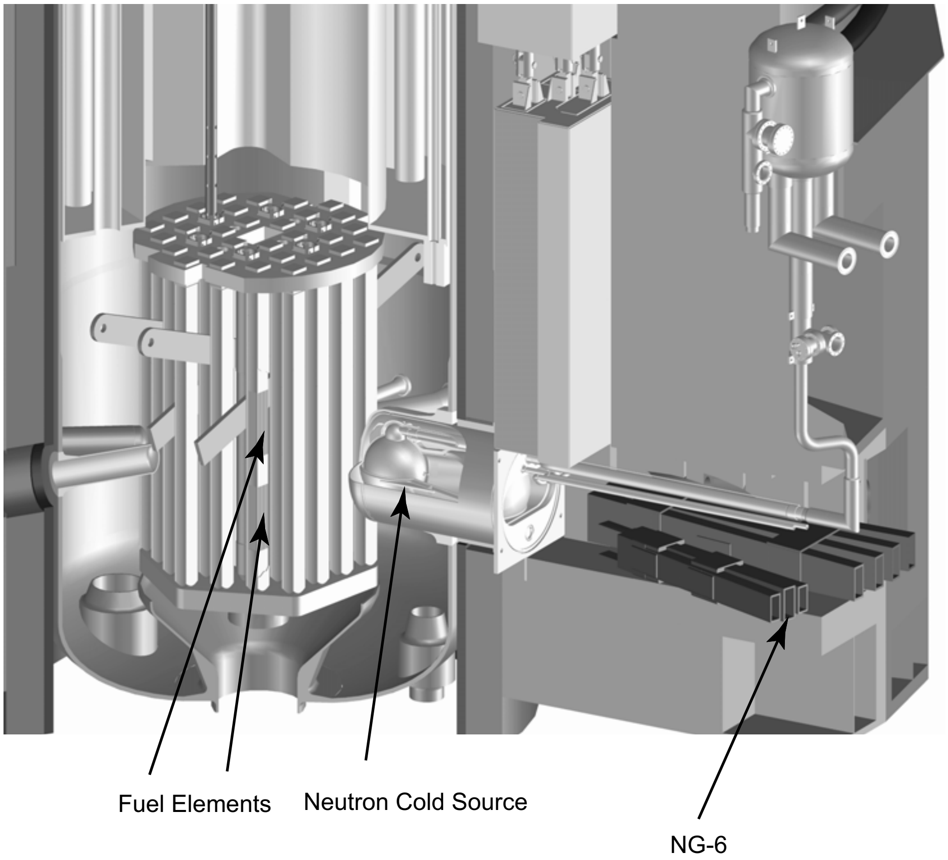

Figure 2.1: Cut-away view of the NCNR reactor core showing the neutron cold source and sections of the neutron guides (NG) used to transport neutrons to the experimental hall.

plates glued together[2]. The guide delivering neutrons to our experiment (NG-6) is 6 cm wide and 15 cm high. It is evacuated to minimize neutron scattering in the air, and has 0.25 mm thick magnesium alloy AZ31B exit window. As mentioned in Chapter 1, neutrons with the perpendicular component of the energy less than the potential of the guide wall will be reflected (ignoring absorption) upon collision with the wall and thus can be "piped" to the experiment. Nickel is used as a coating material since it has one of the highest neutron reflective potentials, while the under-

---

[2] The two-component epoxy adhesive APPLIKA 241 and silicon glue Tecsil 2034 are used.

lying glass surface provides the defining smoothness necessary for efficient neutron transport.

The reactor operates in cycles, typically 39 days of operations followed by 10 days for refueling and maintenance.

As mentioned in Chapter 1, substantial improvement in signal-to-noise ratio in our experiment can be achieved by selecting only the 0.1 nm wide band of the spectrum centered at about 0.89 nm. The selection is achieved by means of a neutron monochromator. The monochromator reflects this band away prom the primary beam at approximately 60° angle. A more detailed description of the monochromator is given in Section 2.2 and in Refs. [54, 68]. Here we present only the general layout of the beam.

The 0.89 nm monochromator is installed in the lower half of the beam delivered by the NG-6 guide, about 60 cm downstream from the exit of the guide as shown in Figure 2.2. The neutron beam reflected by the monochromator is labeled NG6-U, short for NG6-Ultracold. The upper half of the main NG-6 beam is used for a different experiment. The monochromator is located inside a biological shield constructed of steel plate enclosures filled with steel shot and paraffin. The monochromator resides inside the shielding and is enclosed by an aluminum box lined with boroflex[3]. The Boroflex captures scattered neutrons and the steel/paraffin shields attenuate gammas and fast neutrons. In addition to the NG6-U monochromator, there are two more graphite monochromators installed inside the shielding. One of them is used to filter out the $\lambda/2$ component of the NG6-U beam (see Section 2.3.3). The

---

[3] Boroflex is a material used for neutron shielding. It contains boron carbide (B_4C) powder that attenuates the neutron flux due to a high neutron absorption cross section of boron.

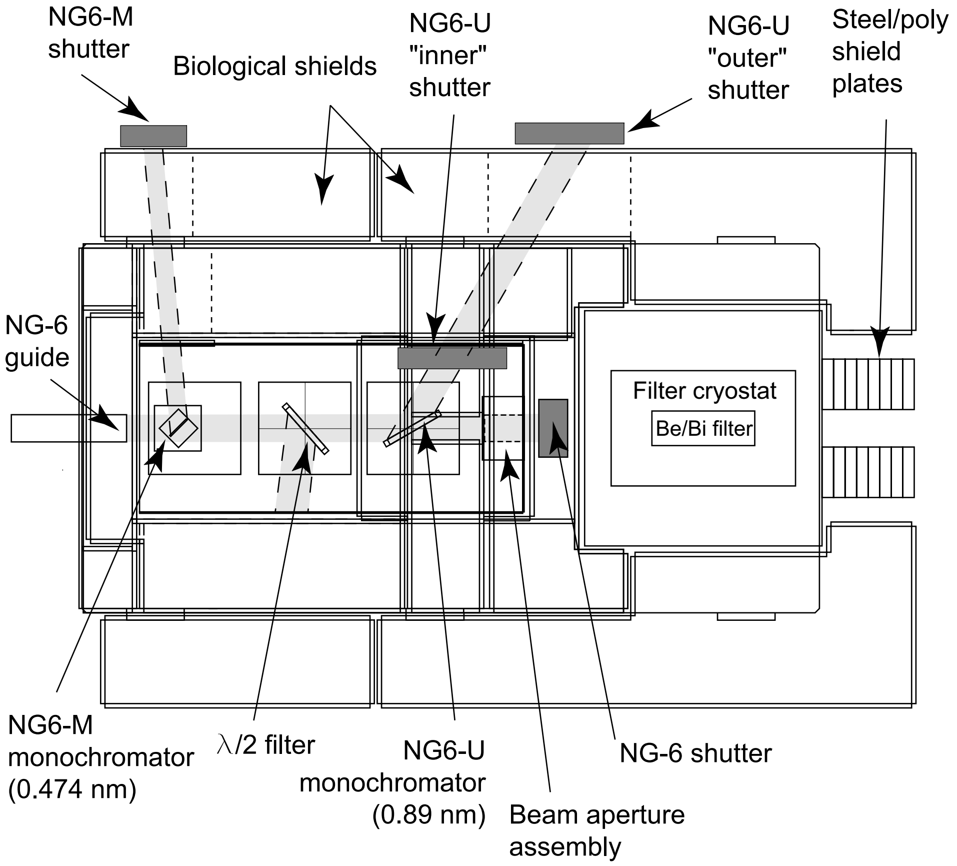

Figure 2.2: Schematic view of the NG-6 monochromator installations and neutron shields. Top view.

NG6-M monochromator, is used to produce a 0.49 nm monochromatic neutron beam for neutron radiometry and ^{3}He polarimetry. These two upstream monochromators have a minimal effect on 0.89 nm neutron flux due to their high transmission at this wavelength (greater than 99 %). The neutron beam reflected by the NG6-U monochromator emerges from the shields through an exit port 9 cm high, 12 cm wide and roughly 60° with respect to the direction of the NG-6 beam.

Two neutron shutters, denoted “inner” and “outer” in Figure 2.2, are used to open and block the NG6-U beam. Only when both shutters are open can neutrons be delivered to the apparatus.

The “inner” shutter is located inside the biological shields. It consists of a 5 cm thick tungsten block mounted on a linear motion stage. The block can be moved in and out of the neutron beam horizontally by a linear actuator. When the shutter is in the “closed” position, the neutron beam is captured by a borated aluminum plate attached to the front surface of the tungsten block. Tungsten is the material used for the shutter because of its high electron density, the essential property for a good gamma shield. The position of the inner shutter may be controlled manually or automatically by computer.

The “outer” shutter, made of steel, has a layer of lithium plastic covering its side facing the beam. It is mounted on the outside of the shields. The outer shutter can be controlled independently of the inner one and can only be operated manually. It serves as a back-up in case of inner shutter failure. During the computer-controlled data taking routine the outer shutter stays open.

Two visual signs are installed to indicate the status of both shutters and warn about potential human exposure to the neutron beam.

The experimental layout showing the position of the apparatus with respect to the shields and monochromators is shown in Figure 2.3.

2.1.1 Apparatus Shielding

Even with both NG6-U shutters closed, the gammas created from neutron capture on the monochromator, monochromator holder and surrounding shields produce an increased background in the detector. In order to shield the apparatus from this

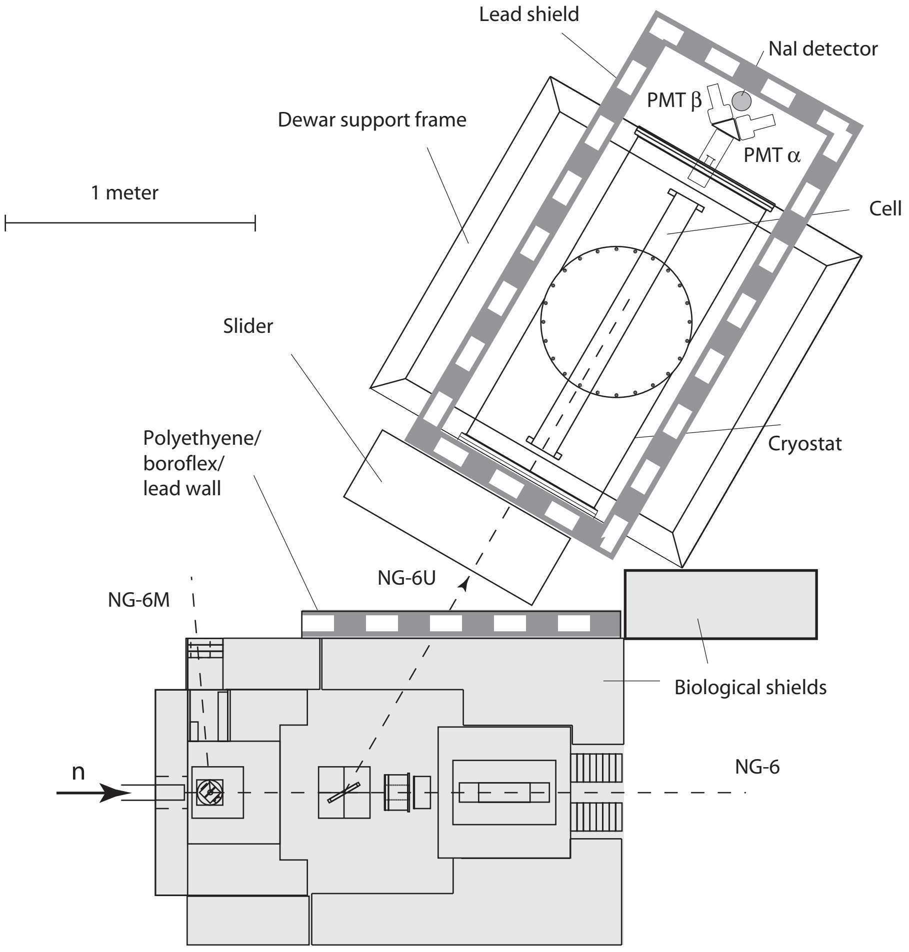

Figure 2.3: Top view of the layout of the experimental apparatus.

radiation, a “slider” was constructed and installed in front of the apparatus. The idea behind the slider is to have a 30 cm thick lead block that can be moved out of the neutron beam path when neutrons enter the apparatus, and moved into this path to block the background radiation. The neutron beam itself is blocked by the shutters described above. Space constraints[4] lead to a design schematically shown

---

[4] The apparatus has to be positioned as close as possible to the neutron exit port to minimize neutron flux loss in the divergent neutron beam. The proximity to the NG6-M beam poses additional limits on the amount of available space.

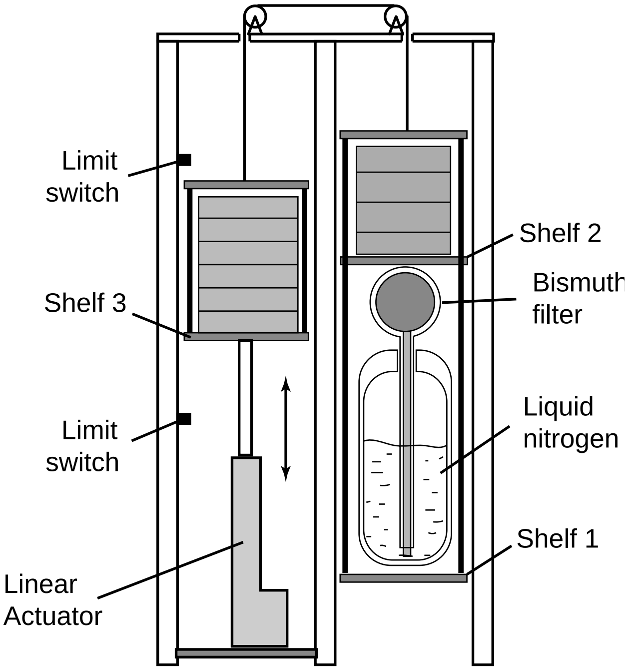

Figure 2.4: Schematic construction of the slider used to block gammas produced by the monochromator.

in Figure 2.4. Three aluminum shelves connected by a steel cable can be moved vertically with the aid of a linear actuator. The travel distance up to a maximum of 30 cm can be set by positioning two limit switches as shown. The lead block consists of 24 bricks (5 cm by 10 cm by 20 cm each) stacked on shelf 2. The total weight of the lead shielding is about 285 kg. In order to decrease the maximum load requirements for the actuator, a counterbalance technique was implemented by stacking lead bricks on shelf 3. The lead block can be moved in and out of the neutron travel path in about 2 seconds. Shelf 1 can be used to support the liquid nitrogen cryostat for a polycrystalline Bismuth block (see Subsection 2.3.3). The slider can be controlled either manually or by computer.

Gamma shielding was also constructed around the apparatus and detectors. These shields consist of a ”floor”, ”roof” and six ”walls”. Each is constructed from a stack of lead bricks and is 10 cm thick. It consists of a 10 cm thick lead “floor”, “walls” and “roof”, stacked of individual lead bricks. The imperfections in the lead brick shapes leave some small gaps in the coverage. The vertical section of the apparatus, see Figure 2.23, however presents a much larger opening that can not be easily covered.

The optimal thickness of the lead shielding depends on the ambient gamma spectrum. The minimum and necessary thickness in our setup was determined in a separate experiment conducted in the vicinity of the trapping apparatus. In this experiment two photomultipliers were detecting the coincidence pulses produced by gamma rays scattering in an acrylic cylinder approximately the size of the acrylic light guide used in our experiment. An increase in lead wall thickness from 10 cm to 20 cm did not change the counting rate, indicating that doubling the lead wall thickness around the trapping apparatus is not likely to lead to a further reduction in the backgrounds.

The apparatus is also surrounded by sheets of boroflex that attenuate the neutrons that are scattered by the nearby instruments. The boroflex sheets are placed on the outside of gamma shield of the apparatus, so that prompt 480 keV gammas from the $^{10}\mathrm{B}(\mathrm{n},\alpha)^{7}\mathrm{Li}+\gamma$ reaction will be absorbed by the shield. The attenuation coefficient of lead for 480 keV gammas is about 1.5 cm^{-1}.

A 5 cm thick layer of polyethylene lined with boroflex is placed outside of the biological shields as shown in Figure 2.3. It serves as a shield from epithermal neutrons that may be scattered from the NG-6 beam towards our apparatus.

The neutron and gamma shields around the apparatus dramatically reduce the backgrounds; the coincidence rate between two cell PMTs (see Section 3.1) drops from 280 Hz to 37 Hz. However, the experiment remains sensitive to the activities of the adjacent neutron beams. To better understand the effects of gammas and neutrons from the guide hall, a NaI gamma detector (see Section 3.1 for more details) is installed inside the shields. Also, the state of the beam shutters of NG-6 and NG-6M was monitored and recorded to make sure that the data was taken under the same operating conditions.

2.2 Neutron Monochromator

An improvement in the signal to noise ratio in our experiment can be achieved by directing only the part of the polychromatic neutron spectrum into the apparatus. While all neutrons contribute to neutron-induced backgrounds in the cell, more than 50 % of the neutrons are available for UCN production are in a ≈ 0.1 nm wavelength band of the spectrum, centered at 0.89 nm (see Appendix A). Several neutron filtering techniques have been considered: mechanical velocity selectors, polycrystalline materials with Bragg edges, thin-film multilayer structures, and crystal monochromators. TA crystal monochromator offers the benefits of high reflectivity, compact size and good utilization of the reactor resources by creating an additional neutron beam and is superior for our experimental setup.

A potassium Graphite Intercalated Compound (GIC) neutron monochromator is installed at the exit of the NG-6 neutron guide as described in Section 2.1.

For any monochromator crystal, Bragg's law must be satisfied: $2d\sin\theta = n\lambda$, where d is the crystal lattice spacing, θ is the angle between the incident neutron beam and the crystal planes, λ is the neutron wavelength and $n = 1, 2, ...$ is the reflection order. The layout of the experimental area restricts the angle of the reflected neutron beam (twice the Bragg angle) to a range of 50° to 130°. Since the wavelength band that contributes the most to the UCN production is centered at $\lambda = 0.89$ nm, the ratio d/n is constrained to the range of 0.49 nm to 1.05 nm. The choice of crystals with such interplanar spacing is very limited. In our previous work [54], we reported detailed studies of fluorophlogopite ($KMg_3(Si_3Al)O_{10}F_2$) and stage-1 and stage-2 potassium intercalated pyrolytic graphite. Potassium intercalated stage-2 pyrolytic graphite was chosen based on its high reflectivity and its mosaic that matches the divergence of the neutron beam emerging form the neutron guide. Monte-Carlo simulations were used to predict UCN production rates inside the experimental cell for different monochromator materials. The detailed description of the intercalation process, crystal characterization and Monte-Carlo simulations may be found in Refs. [54] and [68]. Here we will present a summary of these studies and describe the final monochromator and its alignment (Section 2.3).

The monochromator consists of 9 pieces of stage-2 potassium intercalated crystals (2 cm by 5 cm by 2 mm thick) tiled in a 3×3 array. The assembled monochromator is 6 cm high and 15 cm wide. The term stage-n means that there are n layers of carbon atoms between the consecutive layers of potassium atoms as shown in Figure 2.5.

The graphite crystals were obtained commercially[5], and intercalation was performed in-house. The intercalation is done by sealing the graphite crystal and metallic potassium inside the two ends of an evacuated glass ampule as shown in Figure 2.6. The ampule is heated in a two-zone furnace for a period of 4-5 days while maintaining the potassium at $T_K = (206 \pm 2)$ °C and graphite at $T_G = (318 \pm 2)$ °C.

---

[5] Grade ZYB crystals are purchased from Advanced Ceramics Corp., Lakewood, OH.

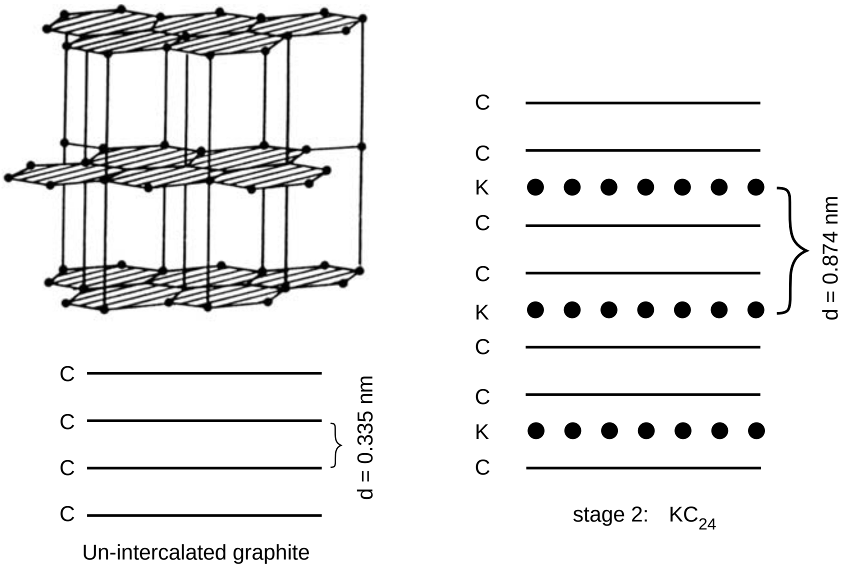

Figure 2.5: Structure of the graphite (left) and intercalated (stage-2) graphite (right). Carbon layers are represented by solid lines, intercalant layers – by circles.

Figure 2.6: Ampule used for intercalation of the graphite with the potassium.

In order to achieve the required temperature difference between the potassium and the graphite[6], the ampule was 35 cm long, with the potassium and graphite placed at opposite ends, as shown in Figure 2.6. The potassium atoms diffuse between the layers of graphite and stay there after the temperature is reduced to the normal room temperature. Due to the high chemical reactivity of potassium, intercalated crystals must be handled in an inert atmosphere or in vacuum. For the same reason, the assembled monochromator is installed in an air-tight aluminum housing filled with

---

[6] The temperature difference $T_G - T_K$ for a fixed T_G determines the final stage of the intercalated material – stage-2 crystals may be obtained for $100\ ^\circ\text{C} < T_G - T_K < 180\ ^\circ\text{C}$ [69].

helium gas at 1 atm. In order to prevent mechanical deformations, the walls of the aluminum holder neutrons have to penetrate to reach the monochromator are relatively thick, 3 mm. This attenuates the neutron flux by about 8 % due to direct neutron capture of the aluminum.

The crystallographic parameters such as interplanar spacing, mosaicity and stage purity of each crystal used in the final assembly were tested on the triple axis spectrometer (BT-7) at the NCNR. The typical mosaicity of the crystals after the intercalation is about 1.5°. As was mentioned earlier, this mosaics nicely matches the 1° divergence of the 0.89 nm neutrons emerging from the neutron guide. Nine crystals of the highest quality have been selected from a total of 15 crystals produced.

Time-of-flight measurements with a setup similar to that described in Section 2.3.1 were performed to measure the average reflectivity of the monochromator assembly. The spectra of the transmitted and reflected beams, shown in Figure 2.7, allow one to determine that the neutron reflectivity in the UCN production band (0.89 ± 0.01) nm is 85 %. The $\lambda/2$ filter (see Section 2.3.3) used in this initial setup that resulted in the spectra shown in Figure 2.7, has a mosaic that is not broad enough to completely filter the $\lambda/2$ peak. This gives rise to the double-peaked structure seen in the reflection at 0.445 nm.

2.3 Monochromator Alignment

After the initial tests, the monochromator was installed in its permanent location inside the biological shields at the end of the NG-6 guide. Once installed, the monochromator required aligning so that it reflected neutrons of the desired spectrum

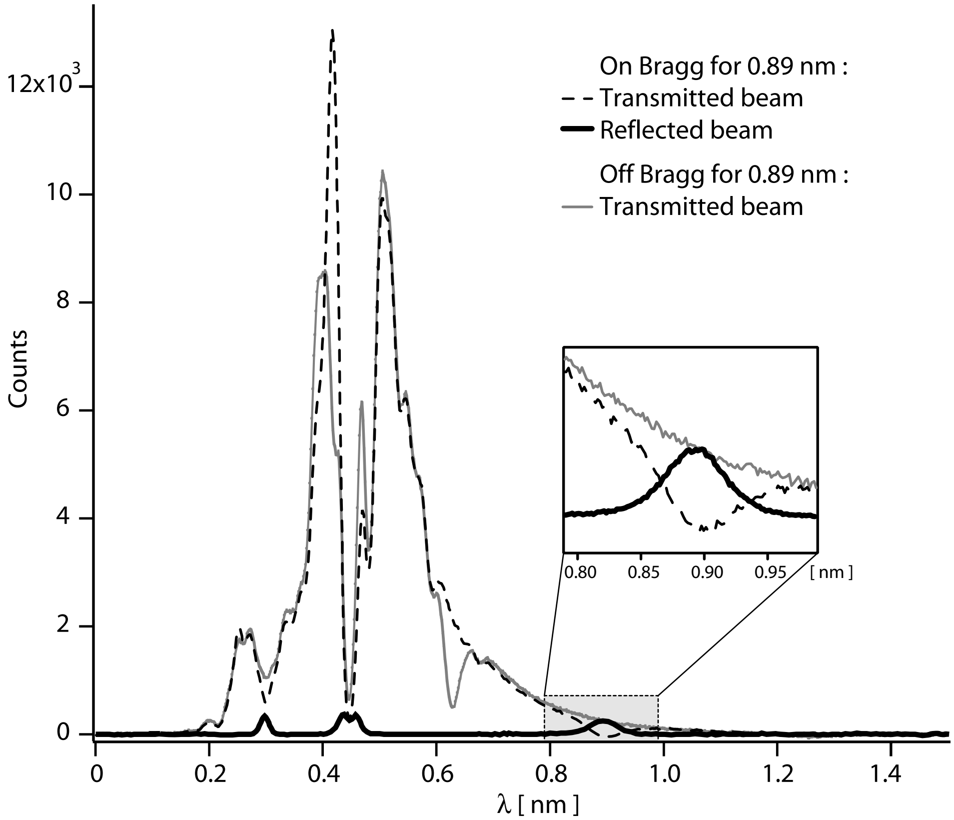

Figure 2.7: Time-of-flight spectra of the monochromatic beamline with $\lambda/2$ filter installed.

band.

2.3.1 Time-of-flight Setup

Since UCN production strongly depends on the neutron wavelength, it is crucial to know the spectrum of the beam reflected by the monochromator. This measurement was performed using a time-of-flight (TOF) setup schematically shown in Figure 2.8. The neutron beam is collimated by an aperture of diameter d located distance l_1 from the monochromator. A neutron chopper, consisting of a spinning disk of neutron-

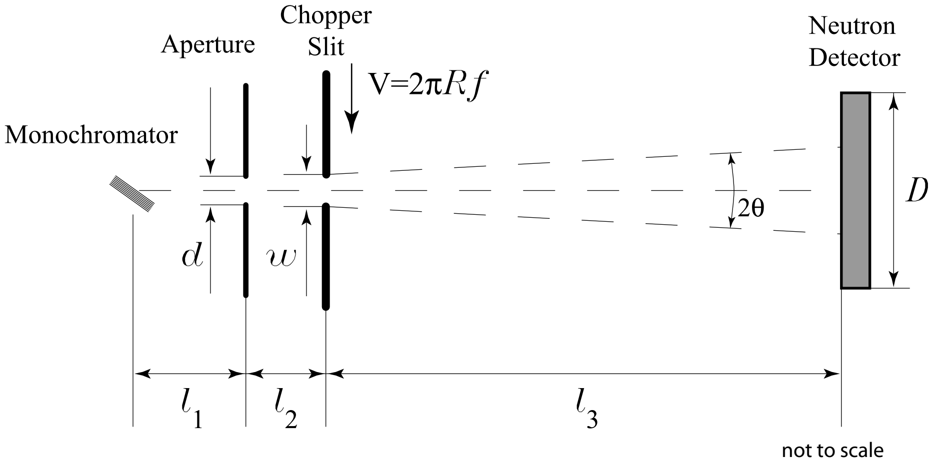

Figure 2.8: Sketch of the time-of-flight setup used to measure neutron beam spectrum.

absorbing material with a slit width w cut radially in the disk, is placed close to the aperture, a distance l_2 from the aperture. When the chopper slit passes behind the aperture, it opens the neutron beam and the detector with active area D positioned a distance l_3 from the copper registers the neutrons arrival. The time delay between the opening of the beam and neutron detection depends on the neutron velocity, thus providing information about the beam spectrum.

If λ is the wavelength of a neutron, then its velocity is given by

$$v = \frac{h}{m_n \lambda},$$

where m_n is a neutron mass and h is Plank's constant. The time-of-flight between the chopper and the detector is then

$$t_f(\lambda) = \frac{l_3}{v} = \frac{m_n}{h} l_3 \lambda = \alpha l_3 \lambda \tag{2.1}$$

The resolution of the wavelength measurement is given by

$$\frac{\delta\lambda}{\lambda} = \frac{\delta t}{t_f}. \tag{2.2}$$

The frame-to-frame variation δt in the time of arrival for a neutron of wavelength λ arises from the finite opening time of the chopper slit and from the variation in distance traveled by the neutron from the aperture to the detector due to the non-zero divergence θ of the neutron beam. If R is the radius of the chopper and f is the chopper frequency, then δt is given bi

$$\delta t = \frac{w+d}{2\pi R f} + t_f(\lambda)\frac{\theta^2}{2}. \tag{2.3}$$

The expression for the second summand is valid if

$$2\theta l_3 \leq D. \tag{2.4}$$

Substitution of Eq. (2.3) into Eq. (2.2) gives:

$$\frac{\delta\lambda}{\lambda} = \frac{\hbar}{m_n}\frac{w+d}{Rfl_3}\frac{1}{\lambda} + \frac{\theta^2}{2}. \tag{2.5}$$

The number of the neutrons reaching the detector per unit time is roughly

$$\Phi \propto A\frac{w+d}{2\pi R}, \tag{2.6}$$

where $A \approx (\min(w,d))^2$ is a characteristic beam cross section area. Generally, it is advantageous to maximize Φ to get a larger signal-to-noise ratio.

If the wavelength of the neutrons lies within a certain band of the spectrum $\lambda_{min} \leq \lambda \leq \lambda_{max}$, the condition for no overlap between the successive neutron pulses is $t_f(\lambda_{max}) - t_f(\lambda_{min}) < 1/f$, or, using Eq. (2.1),

$$l_3 f < \frac{h}{m_n}\frac{1}{(\lambda_{max} - \lambda_{min})}. \tag{2.7}$$

Conditions (2.4)−(2.7) set limits on the parameters of the TOF system and allow us to make an estimate of its resolution. The parameters of the NG6-U time-of-flight

Table 2.1: Parameters of the time-of-flight setup used to measure the NG6-U spectrum.

Parameter	Value
Chopper radius	$R = 15$ cm
Chopper frequency	$f = 60$ Hz
Aperture diameter	$d = 3.8$ mm
Slit width	$w = 3.8$ mm
Diameter of the detector active area	$D = 12.4$ cm
Monochromator–Aperture distance	$l_1 = 60$ cm
Aperture–Chopper distance	$l_2 = 1$ cm
Chopper–Detector distance	$l_3 = 241$ cm
Neutron beam divergence	$\theta \approx 1.5°$
Neutron spectrum width	$\lambda_{max} - \lambda_{min} \approx 10$ nm

setup used to measure neutron beam spectrum are listed in Table 2.1. Substitution of these parameters into Eq. (2.5), gives an instrumental resolution of $\delta\lambda/\lambda \approx 0.025$.

Neutrons are detected using a Burle 8854 photomultiplier tube (PMT) coupled directly to the thermal neutron-sensitive scintillator (Bicron BC-702). The scintillator, an improved version of that described in Ref [70], contains ^{6}Li dispersed in a powder. The ZnS(Ag) is used as a phosphor that converts the energy of the alpha particles and tritons produced in $^6\mathrm{Li}(\mathrm{n},\alpha)^3\mathrm{He}$ reaction into light. The scintillator is "black" (i.e. it has a near zero transmission) within the wavelength of interest.

The cathode of the PMT is biased at +1670 V. The anode signal is amplified by a x10 voltage amplifier (LeCroy 612) and then passes to a discriminator. Pulses are then stretched by a Gate and Delay module to a width of 250 ns. These pulses are recorded by a multi-channel analyzer (MCA). The timing signal for each neutron pulse is generated by a photoemitter/photodetector pair mounted on the chopper to produce a TTL pulse for each revolution of the chopper. The pulse width of the Gate and Delay output was set in a region such that the detector count rate does not change with the width. It is large enough to eliminate double-counting of neutron pulses due to the afterpulsing in the scintillator, but small enough not to introduce large dead times. The diameter of the detector was sufficient for accepting all unscattered neutrons that pass through the slit and chopper aperture.

2.3.2 Alignment Procedures

The monochromator housing is mounted on a computer-controlled rotation (vertical axis) and tilt (horizontal axis) stages. During the reactor shutdown period, the center of the monochromator was positioned on the optical axis of the bottom half of the guide. Then the tilt of the monochromator was adjusted so that the surface of the monochromator housing is vertical. Both rotation and tilt angles have subsequently been fine-tuned as described later in this section. The rough alignment was done by first leveling the rotation stage, then attaching a flat mirror to the surface of the monochromator housing and adjusting the rotation and tilt angles so that the image of the lens of the horizontally-aligned theodolite[7] produced by the mirror was centered in the theodolite viewfinder. After the completion of this procedure, the monochromator was rotated to approximately 30° with respect to the NG-6 beam.

After the reactor startup, the monochromator rotation angle was adjusted to maximize a count rate in the TOF setup with a detector-aperture line at a 60° angle with respect to the NG-6 beamline. Given the interplanar spacing of the stage-2 potassium GIC, the monochromator is roughly in the desired orientation. A typical TOF spectrum for this configuration is shown in Figure 2.9. As one might expect,

---

[7] The theodolite was positioned in such way that the angle between its line-of-sight and the NG-6 beam was roughly at 60°.

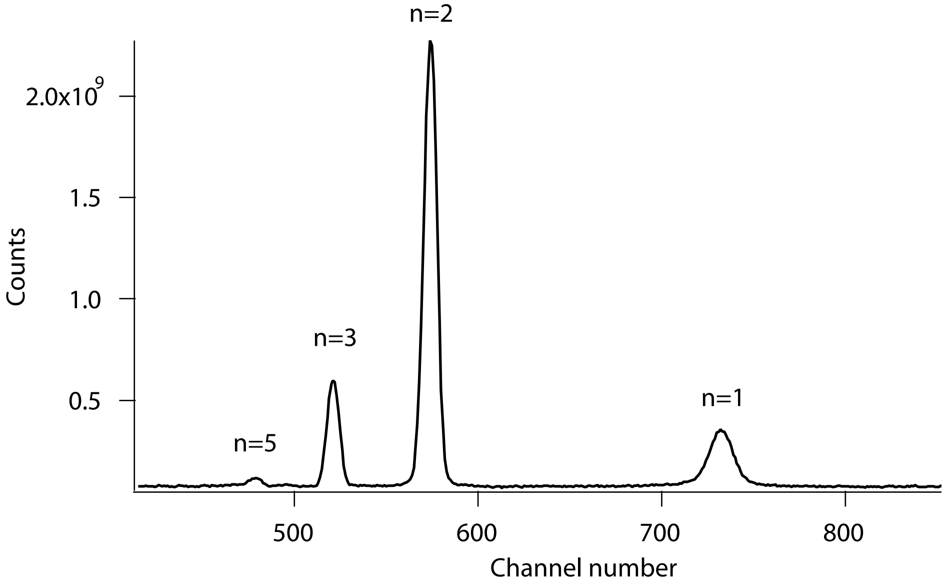

Figure 2.9: Typical TOF spectrum of the reflected neutron beam.

since the Bragg condition $2d\sin\theta = n\lambda$ is satisfied for all positive integer n, in addition to the primary $n = 1$ peak, higher order peaks are also present[8].

There are several ways to convert the MCS "channel number" used as an abscissa in Figure 2.9 into a more meaningful parameter – the neutron wavelength. One approach is to use the Bragg condition $2d\sin\theta = n\lambda$ and measure θ to obtain λ. The obvious problem with this method is that neither d nor θ are well known, so in practice it can be used only to make a rough estimate.

A second approach is to find positions N_n of $n = 1, 2, ...$ peaks corresponding to wavelengths $\lambda_n = \lambda_1/n$ and then perform a linear fit of $N_n(1/n)$ dependance. Indeed, if t_d is the MCS channel dwell time and t_0 is an instrumental time delay, then a

---

[8] The absence of $n = 4$ peak in a TOF spectrum is due to a very small structure factor for this reflection.

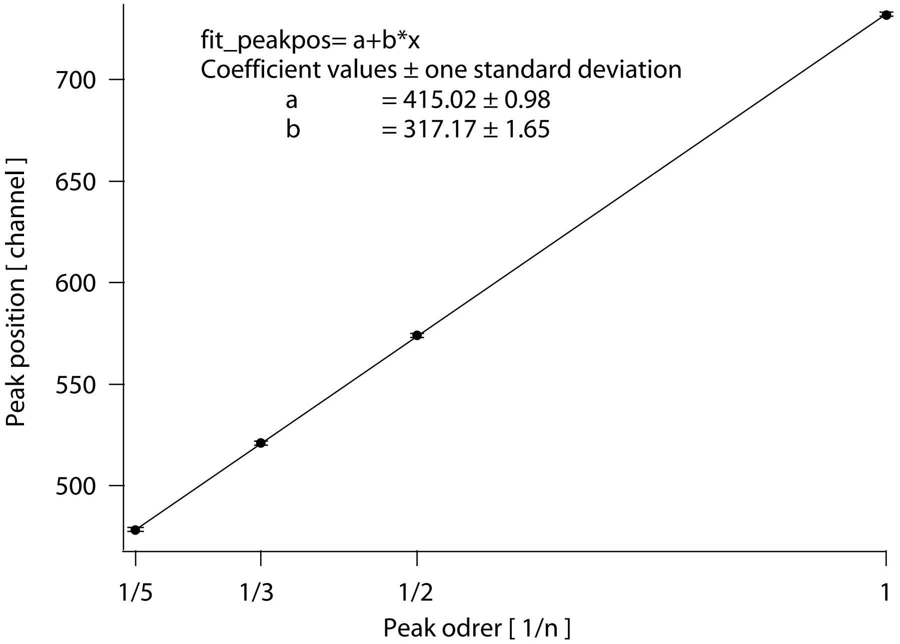

Figure 2.10: Diffraction peak position as a function of the inverse of peak order and results of a linear fit.

neutron with wavelength λ_n should fall into a bin N_n given by:

$$t_d N_n + t_0 = \alpha l_3 \lambda_n,$$

that can also be rewritten as:

$$N_n = \frac{\alpha l_3 \lambda_1}{t_d}\frac{1}{n} - \frac{t_0}{t_d}. \tag{2.8}$$

Coefficient α, defined in Equation 2.1, is known with high accuracy, so the error in measuring λ_1 depends mostly on the precision of l_3 and t_d.

This approach is illustrated in Figure 2.10. Here the positions of the peaks from Figure 2.9 are plotted versus $1/n$. Peak positions were obtained by fitting the spectrum to either Gaussian or Lorentzian shaped functions. The exact shape of the fitting function is not essential - the central values of both fits are the same within the un-

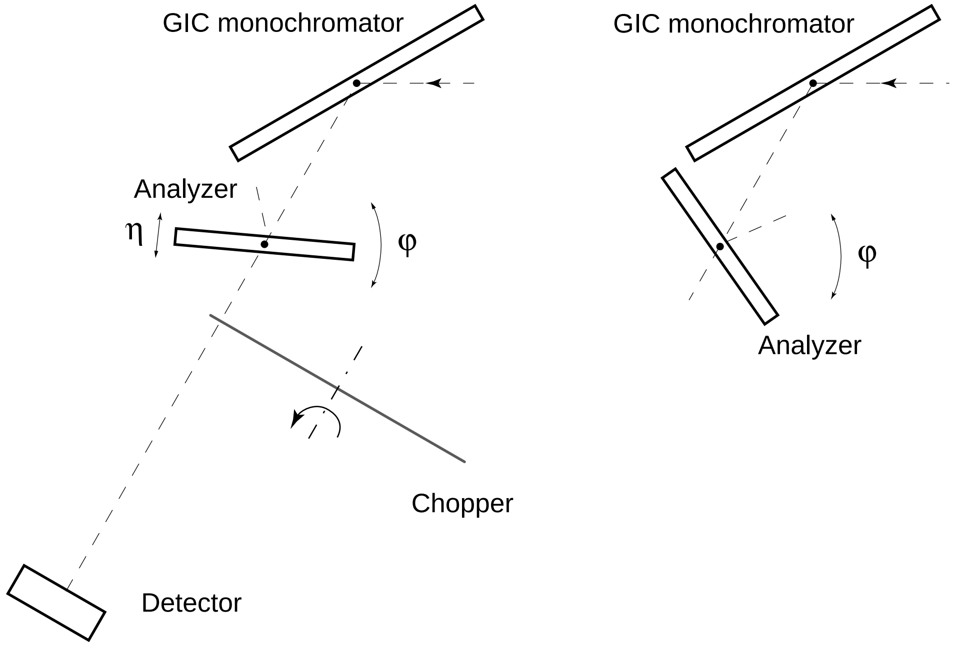

Figure 2.11: Analyzer crystal setup. The GIC and analyzing monochromators may be either in a "parallel" (left) or "anti-parallel" (right) configurations. φ is a rotation angle of the analyzing crystal, η – its tilt.

certainty of the fit. The data fits well to a linear model with a slope of 317.2 ± 1.65. After substitution into Eq. (2.8), one obtains a value of the primary peak wavelength of $\lambda_1 = (0.890 \pm 0.005)$ nm. Estimating the uncertainty in the measurement of l_3 to be approximately 5 mm and the manufacturer's specified uncertainty in the channel width of 1%, the error on the wavelength becomes ±0.011 nm.

In a third approach to calibrate the wavelength, schematically shown in Figure 2.11, an analyzing crystal with a known d-spacing is placed in the reflected beam from the potassium GIC monochromator. Rotation of the analyzing crystal may bring it into an orientation such that the Bragg condition is satisfied for neutrons with wavelength λ_n corresponding to the n-th order peak of the GIC monochromator. In this orientation the flux of the transmitted neutrons in the n-th order peak is in its minimum. This can be observed in the time-of-flight neutron spectrum. The wavelength of the neutrons then can be calculated based on a known analyzing crystal d-spacing and the angle between its on-Bragg orientations for various n, independent of the parameters of the TOF setup. Of three approaches described, this approach is believed to be the most precise method to measure the wavelength.

Although identical for perfect crystals, the "parallel" and "anti-parallel" orientations of the GIC and Si crystals shown in Figure 2.11 produce very different TOF spectra in the case of finite mosaicity crystals. The distinction can be understood by analyzing Bragg reflection in k-space, as shown in Figure 2.12. Here the flux of incoming neutrons has a finite divergency and momentum spread (region I). The Bragg law in k representation may be expressed as

$$\tilde{\mathrm{k}}_{\mathrm{i}} - \tilde{\mathrm{k}}_{\mathrm{r}} = m\vec{G}, \tag{2.9}$$

where m is an integer, and $\tilde{\mathrm{k}}_{\mathrm{i}}$, $\tilde{\mathrm{k}}_{\mathrm{r}}$, and $\vec{G}$, are the incident wavevector, reflected wavevector and reciprocal lattice vector respectively. For simplicity, consider the case of $m = 1$. For mosaic crystals with a small d-spacing variance, instead of a single vector $\vec{G}$, a continuum of reciprocal lattice vectors should be used, all with the same length and with an angular spread equal to the crystal mosaicity. Given the k-space region of $\tilde{\mathrm{k}}_{\mathrm{i}}$ and $\vec{G}$, the k-space region of the reflected beam (region III) can be obtained geometrically. For each $\vec{G}$, plot a perpendicular surface from its endpoint. According to Eq. (2.9), the reflection produced by the vector $\vec{G}$ is a mirror image of the intersection between this surface and region I with respect to $\vec{G}$. Region III is then a combination of thus obtained reflections for all $\vec{G}$. The non-zero crystal mosaicity increases the divergence of the reflected beam. From (2.9) it also follows that only

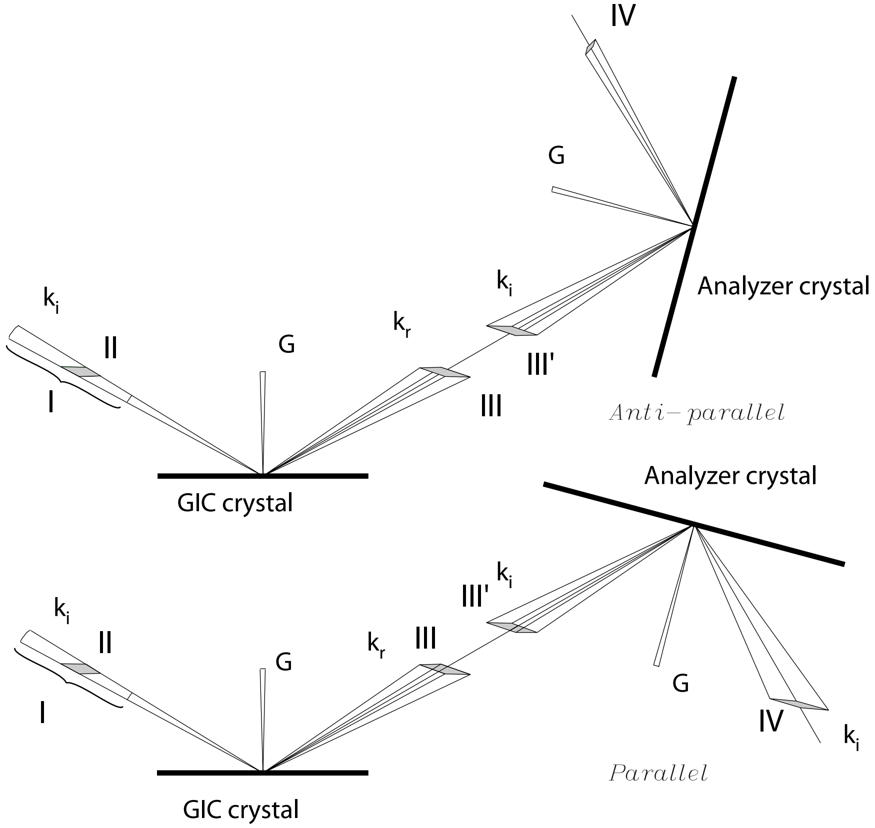

Figure 2.12: K-space diagram of the Bragg reflections from the potassium GIC monochromator and the analyzing crystal in parallel and antiparallel orientations.

a part (region II) of the incoming flux will be reflected by the monochromator. A similar construction for the reflection from the analyzing crystal puts some neutrons into region IV. As shown in Figure 2.12, the divergence of the neutron beam in region IV is larger in the parallel configuration compared to the antiparallel case. This was observed experimentally.

A Silicon crystal with a diameter of 75 mm and thickness of 9 mm was used as an analyzer. The crystal had a mosaicity of 0.4° with its crystallographic [111] planes parallel to the surface. The interplanar spacing of the Si [111] planes at 300 K is

$d_a = 3.1385(56)$ Å [71]. The analyzing crystal was mounted on a rotation-tilt stage between the chopper and the GIC monochromator as shown in Figure 2.11. Since $\lambda_1 > 2d_a$, neutrons with wavelength λ_1 can not Bragg scatter in the Si crystal. Let φ_n and φ'_n be rotational angles of the analyzing crystal such that the n-th peak of the TOF spectrum is in its minimum in antiparallel and parallel orientations respectively. Let us define η as a tilt angle of the analyzing crystal, that is the angle between the normal vector of the 111 planes of the silicon and the horizontal plane. Measuring $\Delta\varphi_n = \varphi_n - \varphi'_n$ in case of $\eta = 0$ give the value of λ:

$$\lambda = 2nd_a \sin(\Delta\varphi_n/2).$$

As will be seen later, in practice we found that this method gives larger errors due to the uncertainty in determining the peak positions for the anti-parallel configuration.

Since the peaks in the parallel configuration are narrower, they alone can be used to measure the wavelength. The incident angle of the neutron beam θ_n can be expressed in terms of rotation angle φ_n and tilt η as:

$$\cos\theta_n = \cos\varphi_n \cos\eta \tag{2.10}$$

The Bragg condition of for the $n = 2, 3$ (here n is referring to the order of the reflection of the GIC monochromator; we assume the primary reflection from the analyzing crystal) is then:

$$\begin{aligned} 2d_a \sin\theta_2 &= \lambda/2, & (2.11) \\ 2d_a \sin\theta_3 &= \lambda/3. & (2.12) \end{aligned}$$

Expressed in terms of $\delta \equiv \varphi_2 - \varphi_3$, the parameter that is directly measured in the

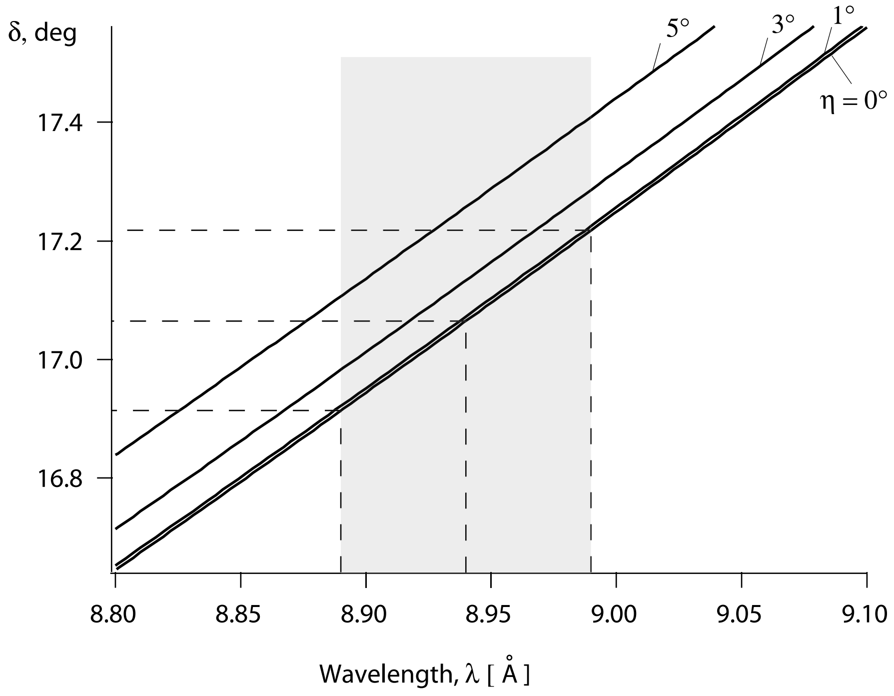

Figure 2.13: Solutions of the Equation (2.13) for several values of the tilt angles η. The shaded area shows the 1σ uncertainty in the calculation of the peak position of the UCN production band (see Appendix A). The width of the production band for our trap is roughly 0.07 Å.

experiment, Equations (2.10) to (2.12) can be reduced to:

$$\delta = \arccos\sqrt{\frac{1-9x^2}{\cos^2\eta}} - \arccos\sqrt{\frac{1-4x^2}{\cos^2\eta}}, \tag{2.13}$$

where $x = \lambda/12d_a$. The inverse function, $\lambda(\delta)$ for $\eta = 0$ has a simple form:

$$\lambda = 12d_a\frac{\sin\delta}{\sqrt{13-12\cos\delta}}. \tag{2.14}$$

In the general case of $\eta \neq 0$, the analytical solution is a bit more complicated. It is represented graphically in Figure 2.13 for several η.

According to Appendix A, the desired wavelength band for superthermal neutron production is about 0.01 nm wide with central value of 0.894 nm. As can be seen

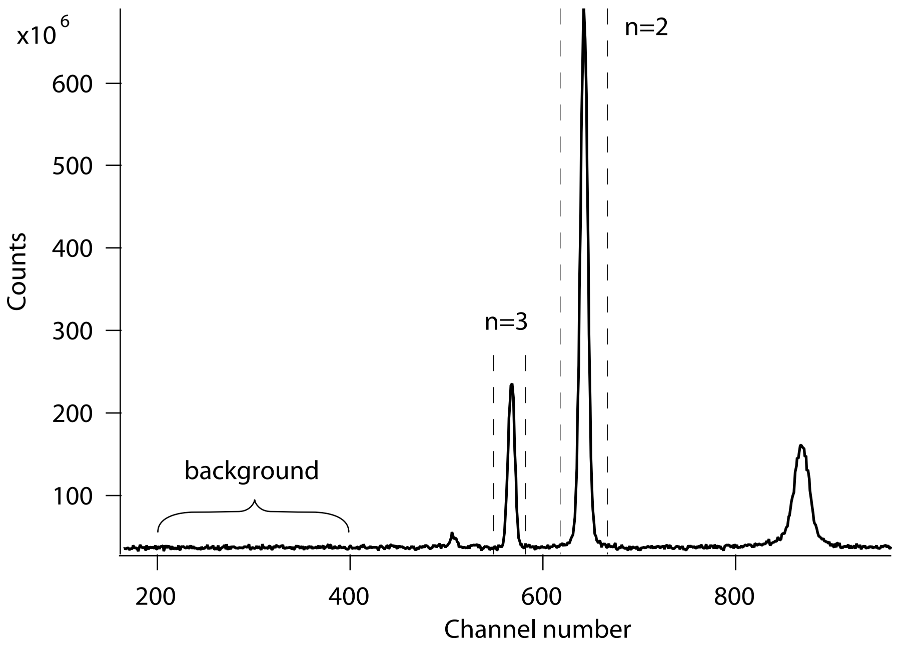

Figure 2.14: The TOF spectrum with an analyzing Silicon crystal in the beam. The area between channels 200 and 400 is used to determine the background. The $n = 2, 3$ peak areas are obtained as the integral under the curve between the dashed lines, with the background subtracted.

from Figure 2.13, it implies that we need to know δ to better than 0.1°and the tilt of the analyzing crystal should not exceed several degrees.

A typical TOF spectrum is shown in Figure 2.14. For all channels P_n laying between the dashed lines marking the $n = 2$ and $n = 3$ peaks in the spectrum, we calculate the size of a peak as:

$$S_n = \sum_{i \in P_n} (N_i - b), \tag{2.15}$$

where N_i is a number of counts in the ith channel and background b is calculated for each spectrum as

$$b = \frac{1}{201} \sum_{i=200}^{400} N_i.$$

Because of the subtraction of the background, the value of S_n does not depend strongly on the choice of the summation range P_n.

In addition to the peak size, we will also define the adjusted peak size as:

$$S'_n = S_n \frac{< S_k >}{S_k}, \tag{2.16}$$

where $< S_k >$ is an average off-Bragg ($k = 2$ for $n = 3$ and $k = 3$ for $n = 2$) peak size, averaged over all orientations of the analyzing crystal in the vicinity of the on-Bragg peak n. S_k is shown to vary by less than 3%; this may be due to the variation in neutron the flux reaching the detector caused by the chopper vibrations.

The dependance of S_n and S'_n on the rotation angle φ_n of the analyzing crystal is shown in Figure 2.15. The central values of Gaussian fits are used as an estimate of the position of the peaks. The instrumental error in determining the rotational angle of the crystal is about 0.05° and must be added to the error of the fit.

The angle δ defined by Eq. (2.13) is then $\delta = (17.02 \pm 0.07)^\circ$. According to Eq. (2.14) this corresponds to a wavelength of $\lambda = 0.892 \pm 0.002$ nm. The tilt of the analyzing crystal is measured to be less than 0.5°, thus presenting a negligibly small correction to the wavelength measurement.

This value of the wavelength was obtained after fine-tuning the rotation and tilt of the GIC monochromator to reflect the desired wavelength band. The tilt adjustment is made by analyzing neutron beam images taken at two distances from the monochromator. When the monochromator is vertical, the initially horizontal beam emerging from the neutron guide should stay horizontal after the Bragg reflection from the monochromator. The fact that the beam is not monoenergetic and quite wide presents certain challenges to this measurement. We used the $\lambda/2$ and Bismuth

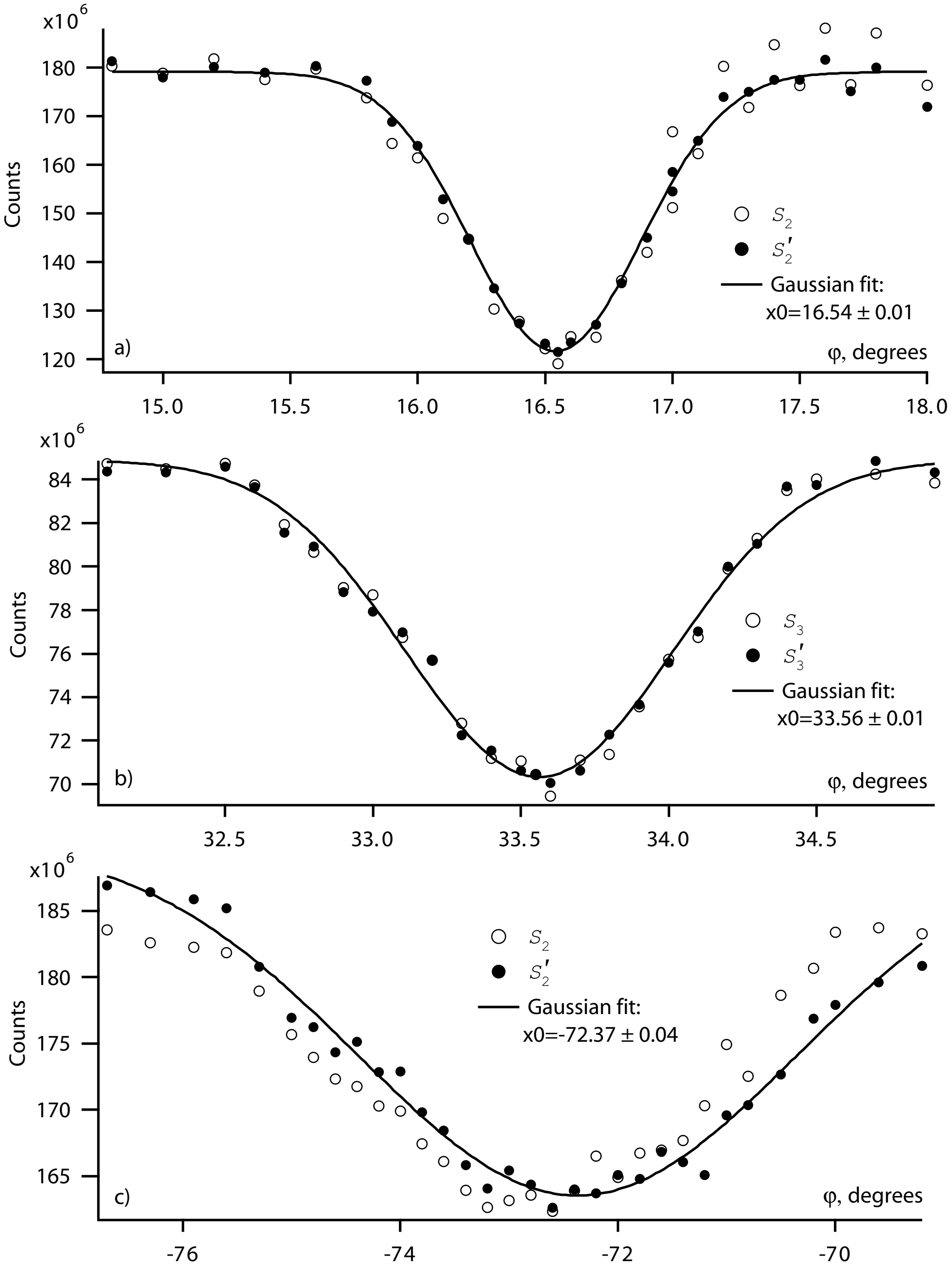

Figure 2.15: The dependance of the peak size defined by Equations (2.15) and (2.16) on a rotational angle of the Silicon analyzing crystal. a) Primary monochromator $n = 2$ peak in a parallel orientation of the crystals, b) Primary monochromator $n = 3$ peak in a parallel orientation of the crystals, and c) Primary monochromator $n = 2$ peak in an anti-parallel orientation of the crystals. Also shown are Gaussian fits and their central values.

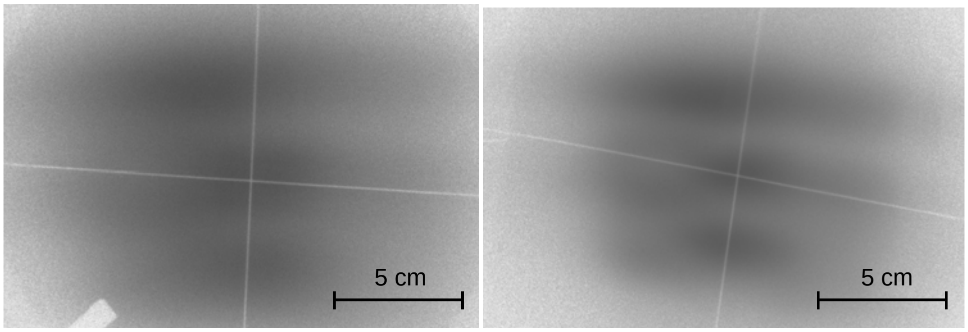

Figure 2.16: Neutron images obtained using a neutron sensitive image plate placed behind the Cd-containing wires. These images are used for adjusting the tilt of the potassium GIC monochromator. The distance between the monochromator and the imaging plate for the image on the left is roughly 2.3 m, for the image on the right – about 1 m.

filters (at 300 K) described in Section 2.3.3 to filter out most of the neutrons in the higher order reflections. Then, two crosses of 1 mm diameter wire rich in Cadmium are used to create masks in front of a neutron sensitive image plate[9]. Both crosses are mounted on the linear 2D translation stages attached to a horizontal rail allowing the adjustment of the position of one cross without disturbing the position of the other. The distance between the crosses was set to about 125 cm. After a 10 s exposure to the neutron beam, the stored, slowly-decaying luminescence of the material covering the surface of the neutron image plate is read by a scanner, producing images similar to those shown in Figure 2.16.

Based on the beam images, the crosses are aligned in such way that the center of the beam coincides with the center of the wire crosses. The center of the beam is defined as the position on the center of a 10 cm diameter circle that maximizes the number of neutron counts inside that circle. The tilt of a theodolite sighted through

---

[9] BAS-ND imaging plate manufactured by Fuji Photo Film Co., Ltd.

both crosses was less than $7'30''$, corresponding to a upward shift of the beam of less than 2 mm per 1 m travel path. Since the diameter of the trapping region is 8.6 cm and the neutron travel distance inside the cell is less than 1 m, this deviation is quite acceptable.

2.3.3 Neutron Beam Filters

As mentioned earlier, we are primarily interested in the $\lambda = 0.89$ nm band of the reflected neutron spectrum for UCN production. As shown in Figure 2.9, the flux of neutrons in the $n \geq 2$ peaks with wavelength equal to λ/n exceeds the flux in the primary ($n = 1$) peak. In order to remove neutrons in the $n \geq 2$ peaks we use two filtering techniques: reflections from the pyrolytic graphite and polycrystalline bismuth.

The first technique consists of placing a pyrolytic graphite crystal with a mosaic of approximately 3.5° (grade ZYH) upstream of the potassium GIC monochromator. The d-spacing of the graphite, roughly 0.335 nm [72], does not allow Bragg reflections of 0.89 nm neutrons[10]. The graphite crystal can however be aligned to reduce the amplitude of the $n \geq 2$ and $n = 4$ peaks, although the later one is small to begin with. We refer to this crystal as the $\lambda/2$ filter.

The second technique consists of placing polycrystalline bismuth into the beam. Bragg cutoff of Bismuth is 0.65 nm [73], implying that, at least in theory, all neutrons with the wavelength smaller than 0.65 nm will find a properly oriented bismuth monocrystal to be Bragg-scattered. Space constraints do not allow us to place this

---

[10] According to Bragg's law, the maximum neutron wavelength that can be reflected from a graphite crystal is $2d = 6.7$ nm.

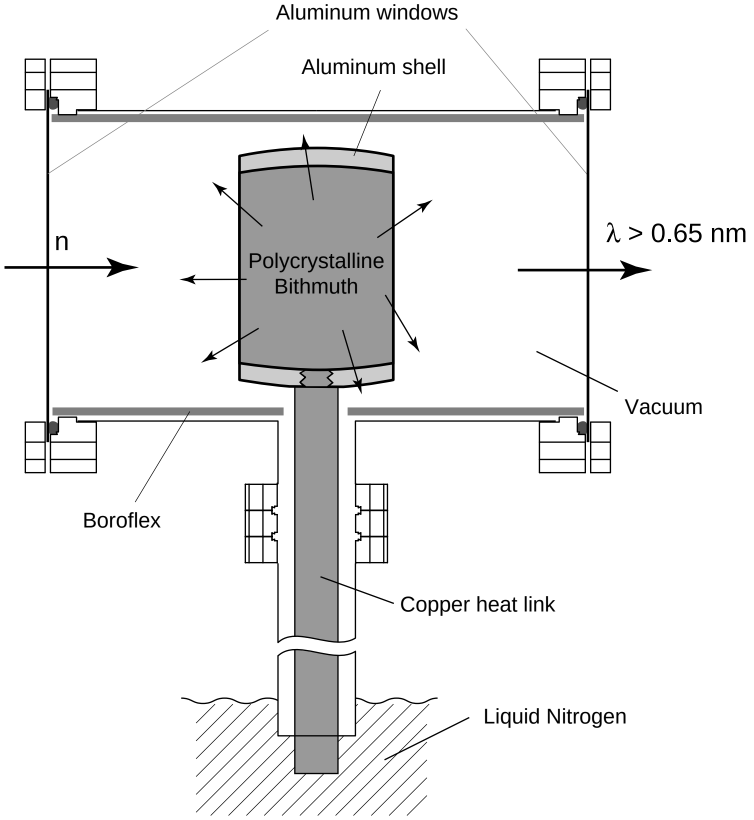

Figure 2.17: Side view of a cryostat used to cool the Bismuth polycrystalline block to 90 K.

filter inside the biological shielding, so it is positioned between the NG6-U outer neutron shutter and the trapping apparatus (see Figures 2.3 and 2.4). The polycrystalline bismuth filter used in the experiment is 10 cm in diameter and 5 cm thick. It is prepared by compressing water quenched 99.9 % pure bismuth shot with a typical grain size of 2 mm. The shot is compressed at a pressure of 200 MPa inside an aluminum tube with wall thickness of 1.2 cm. A thin layer of borated aluminum lines the inner surface of the tube to reduce the neutron activation of the aluminum tube. The filter is placed in a vacuum chamber schematically shown in Figure 2.17 and cooled to 90 K to minimize Debye scattering. The cooling is provided through a

2.5 cm diameter copper rod attached to the aluminum tube surrounding the bismuth filter. The other end of the copper rod is immersed in liquid nitrogen (see Figures 2.4 and 2.17). The filter and the liquid nitrogen dewar are installed on the slider and can be moved in and out of the beam (see Section 2.1.1). The bismuth block is wrapped in three layers of 6.5 μm thick aluminized mylar to reduce the radiative heat load. In order to prevent neutron activation of the cryostat, the inner wall of the cryostat is lined with boroflex. The temperature was measured with a silicon diode mounted on the aluminum tube. Although the temperature of the bismuth block itself may be higher than the temperature of the aluminum tube, the Debye scattering in the filter is observed to be substantially smaller than at 300 K. The neutron entrance and exit windows are made from 0.5 mm thick aluminum sheets sealed using Viton Conflat gaskets.

The reflected neutron spectra from the monochromator, with and without the higher order peaks filtered are shown in Figure 2.18. The graphite filter reduces the $\lambda/2$ peak by 95 % with negligible attenuation of the 0.89 nm peak. The Bi filter reduces it further, to roughly 1 % of the initial value. The attenuation of the $n = 3$ reflection peak by the Bi filter is about 76 %, while the attenuation of the 0.89 nm peak is only about 5 %, attributed primarily to Debye scattering and absorption by impurities in the bismuth.

2.3.4 Neutron Flux Measurements

To measure the flux of the neutrons in the reflected beam we used a fission chamber containing a 503 ng ^{235}U deposit with active area of about 1 cm^2. Following a neutron-

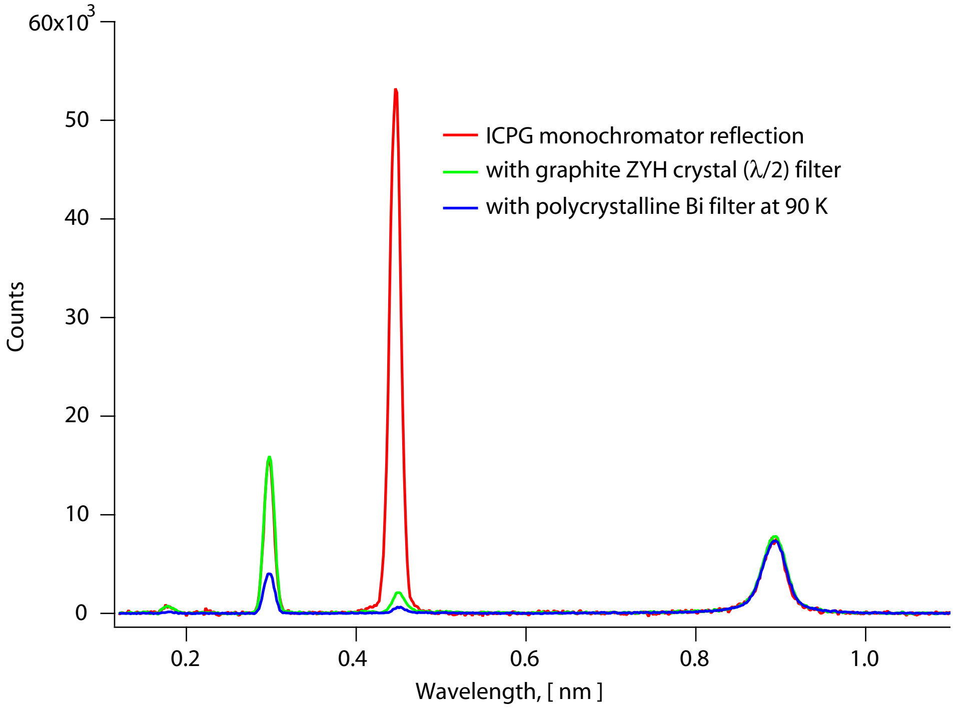

Figure 2.18: TOF spectrum of the reflected beam with and without high order peak filters.

induced fission event in the chamber, the fission products are accelerated by the electric field of the ion chamber and can be detected with nearly 100 % efficiency.

The fission chamber counting rate when the chamber is placed in a neutron beam of flux density $\Phi(\lambda)$ is

$$F = \int \Phi(\lambda) n \sigma_f(\lambda) d\lambda = \frac{N_A m}{A} \int \Phi(\lambda) \sigma_f(\lambda) d\lambda, \tag{2.17}$$

where n, A, and m are the number density, atomic mass and total mass of ^{235}U deposit respectively, N_A is Avogadro's number, and $\sigma_f(\lambda)$ is the fission cross section. Values of $\sigma_f(\lambda)$ are tabulated in Ref. [74] and can be approximated by $\sigma_f(\lambda) \approx 348\lambda - 37.4$ b for λ [Å] in the 1.8 $\mathring{A}$ to 10 $\mathring{A}$ range.

Equation (2.17) is used to normalize the TOF spectrum flux density $\Psi(\lambda)$ shown

Table 2.2: Measurements of the neutron flux using a fission chamber installed in front of the neutron entrance window of the trapping apparatus. Measurements are performed with two filter setups. Neutron fluxes are quoted in units of $10^6\,\text{cm}^{-2}\text{s}^{-1}$. The uncertainty in the total flux measurements are about 10 %.

	Bi and $\lambda/2$ filters	$\lambda/2$ filter only
0.89 nm peak	3.9	3.7
0.45 nm peak	0.26	0.7
0.22 nm peak	0.75	2.6
0.18 nm peak	0.04	0.17
Total	4.9	7.1

in Figure 2.18. Under the assumption that the efficiency of the TOF detector is independent of the wavelength, which is a reasonable assumption for a "black" detector, the true flux density is proportional to the measured spectrum: $\Phi(\lambda) = \epsilon\Psi(\lambda)$. The total neutron flux can be calculated as:

$$\Phi_0 = \int \Phi(\lambda)\,d\lambda = F\frac{A}{N_A m}\frac{\int \Psi(\lambda)\,d\lambda}{\int \Psi(\lambda)\sigma_f(\lambda)d\lambda},$$

and the flux in peak k as:

$$\Phi_k = \Phi_0\frac{\int_k \Psi(\lambda)\,d\lambda}{\int \Psi(\lambda)\,d\lambda},$$

where $\int_k$ means integration over the neutron wavelengths corresponding to peak k.

The neuron flux measured with the fission chamber positioned in front of the 300 K neutron entrance window (160 cm downstream of the center of the monochromator and 75 cm upstream from the center of the trapping region), is shown in Table 2.2. The values of the 0.89 nm flux calculated from these measurements are quite consistent. The neutron flux measured at the edges of the neutron beam entrance window, roughly 6 cm off-center, is found to be about 40 % smaller than the value quoted in Table 2.2.

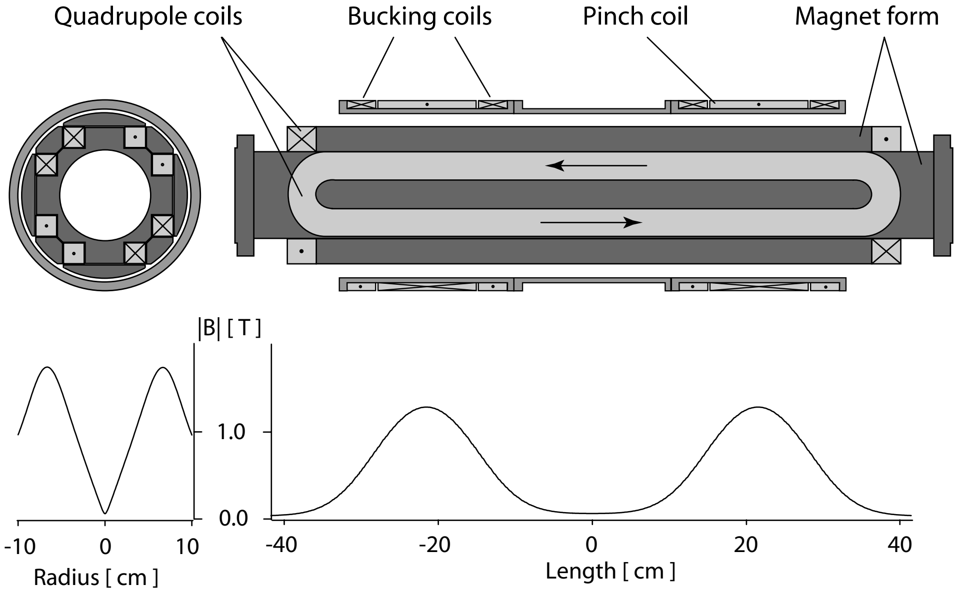

Figure 2.19: The design of a racetrack magnet coil.

2.4 Magnetic Trap

The magnetic field of the UCN trap is produced by an Ioffe-type superconducting magnet assembly. This section provides an overview of the magnetic trap. A more detailed description of the magnet construction and its training behavior can be found in Refs. [54] and [55].

An Ioffe-type configuration consists of four quadrupole racetrack-shaped coils and two solenoid assemblies (denoted as "bucking" and "pinch" coils), as shown in Figure 2.19. The quadrupole coils provide a radial field gradient, while the solenoid assemblies "close" the trap axially. Together, they create a magnetic field minimum in space that makes neutron trapping possible.

Each coil is wound using a single strand of a multifilament copper-stabilized NbTi wire. The copper is used to protect the superconductor by carrying current during a magnet quench. The wire is wound under tension and is embedded in epoxy that is applied during the winding process. The epoxy serves to minimize wire movement under the action of an Ampere force. Fiberglass sheets of 0.5 mm thickness are placed between the each wire layer during the coil winding in order to prevent crack propagation in the epoxy.

The two solenoid assemblies are of the same design and consist of three solenoids. The large central solenoid (the “pinch coil”), creates the field maximum at the end of the trap. The two smaller solenoids (“bucking coils”), are wound in the opposite direction such that the field from the bucking coil cancels the field from the pinch coils thus increasing the length of the trapping region and decreasing fringe field in the “turn-around” region of the quadrupole coils. The lower field in the “turn-around” region is necessary to prevent quenching of the wire in the high field. The currents in the two pinch coils flow in the same direction (Helmholtz configuration), creating a non-zero magnetic field at all points inside the trap, thus suppressing Majorana spin-flip losses [75].

The overall size of the magnet was the largest that could still fit in the existing cryostat. Several parameters were optimized in the magnet design: the geometrical dimensions of the coils, the superconducting wire diameter, and the copper to superconductor ratio. The optimization parameter is the number of trapped neutrons. This number grows both with an increase in trap volume and trap depth. Magnetic field calculations were performed using Biot-Savart integration by the computer program “Biot-Savart”[11]. The optimal parameters of the trap are listed in Table 2.3.

---

[11] Ripplon Software Inc. Burnaby BC, Canada

Table 2.3: Magnetic trap parameters.

Parameter	
Bore diameter, mm	105
Solenoid form outer diameter, cm	24.7
Quadrupole coil length, cm	81
Distance between solenoid centers, cm	42
Wire diameter, μm	740
Wire Cu:NbTi ratio	2:1
Wire insulation	Formvar
Load line limit, A	320
Operating current, A	160
Trap depth at 160 A, T	1.1

The quadrupole coils were tested individually and reached a maximum current equal to at least 85 % of their load line (the maximum possible value of the current based on the superconductor critical field). The four quadrupole coils were then attached to the titanium magnet form as shown in Figure 2.19.

An important question in magnet assembly design is how to support the coils. In order to prevent coil movements that can cause the magnet to quench, coils are typically prestressed (that is the external “holding” force is larger than the Ampere force acting on the conductor). In our setup, prestressing is achieved by relying on the difference in thermal expansion coefficients for different materials. First, several titanium spacers have been machined in order to make the quadrupole assembly cylindrical. Then aluminum collars are placed around the quadrupole with a clearance of less than 25 μm. When cooled, the aluminum tubes contact more than the titanium form and the magnet coils [55]. The differential contraction prestresses the magnet coils radially. The aluminum collars always remain in an elastic regime, which guarantees operation of this scheme even after multiple cooling cycles. Although it provides radial prestressing, this scheme does little to prevent axial movement of the coils. This may be one of the reasons responsible for the sub-par performance of the magnet.

The solenoid assemblies and connected in series with the quadrupole coils. The current for the magnet is supplied by a HP-6680A DC power supply and is conducted to the magnet through AWG 3/0 welding cable and through vapor-cooled current leads that penetrate into the main bath of the cryostat (see Section 2.5).

In order to reduce the magnetic fringe fields that could potentially interfere with other equipments in the experimental hall, compensating coils have been designed and built. Far-fields originating from the trap are primarily due to the solenoid assemblies and thus fall off with distance as $\sim 1/R^3$. This field can be canceled to first order using a set of external coils to create a magnetic field flux of the same magnitude, but in the opposite direction.

Each of the two compensating coils consists of three rectangular 1.4 m wide and 3 m high "loops" of copper bus bar. The coils are attached to two sides of the frame supporting the trapping apparatus, in the plane perpendicular to the axis of the trap. The bus bars are 5 cm by 6 mm in cross section. A DC power supply[12] providing the current for the compensating coils operates in "auto-sense" mode in which the output current is proportional to the current of the superconducting trap. This mode of operation ensures that the field from the trap is properly compensated at any trap depth. A ratio of 3.28 between the current of the compensating coils and the superconducting trap current has been experimentally determined to provide the optimum compensation for the spin-echo instrument located roughly 15 m away

---

[12] Hewlett Packard 6681A.

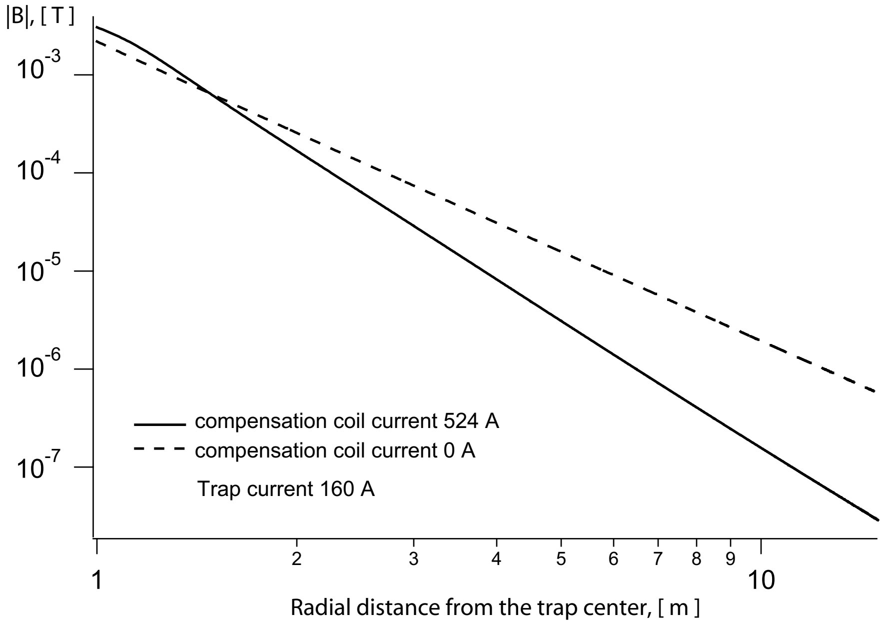

Figure 2.20: Calculations of the magnet far field with and without compensation coils.

from the trapping apparatus. The calculation of the magnetic field amplitude as a function of the distance from the center of the trap, perpendicular to the trap axis, is shown is Figure 2.20. Compensating coils are connected to the power supply by two AWG 3/0 welding cables connected in parallel. Due to the high current through the compensating coils, care should be taken not to restrict their convective cooling.

Even in the most careful design, there is always the possibility of a magnet quench. A quench occurs when part of the superconducting wire goes to the normal resistive state and starts dissipating energy. This process may be caused by a variety of factors, for example by the motion of a loose wire or by an imperfection in the wire or joints. The energy dissipation increases the local temperature of the wire, that in turn increases its resistance and causes even faster energy dissipation in the region. Of course, the normal phase starts propagating throughout the magnet, both along the

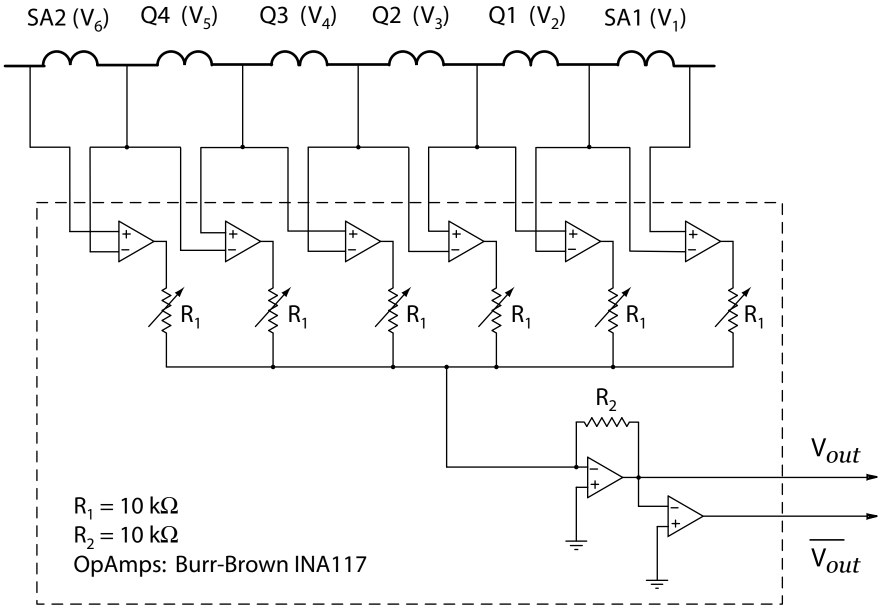

Figure 2.21: Quench detection circuit diagram.

wire (copper cladding of the superconductor facilitates this propagation) and across the turns. If the propagation is slow, a large portion of the magnet's stored energy could be released in a small volume. For large, high-field magnets, the energy is so large (typically more than 50 kJ) that it may damage the wire insulation or even melt the wire and thus destroy the magnet. In order to protect the magnet, we implemented a scheme to detect the quench and then to initiate a "quench protection" circuit to dissipate part of the stored energy into an external resistor outside the magnet.

The quench detection circuit is shown in Figure 2.21. For quench detection purposes, the three coils of each solenoid assembly are considered as one coil (SA1 and SA2 in Figure 2.21). The voltages V_1 through V_6 across each quadrupole coil (Q1 through Q4) and solenoid assembly (SA1 and SA2) consist of the resistive and inductive components $V_i = V_i^R + V_i^I$, $i = 1, .., 6$. In the superconducting state, the resistive component is zero. The inductive component is non-zero if the magnetic flux through the coil is changing, as happens during the magnet ramp-up or ramp-down. Since all coils are connected in series, and due to the symmetry of the magnet, the flux penetrating the coils opposing each other is practically the same and can be canceled out by subtraction. The output voltage of the circuit shown in Figure 2.21 is proportional to the sum of the input voltages:

$$V_{out} = \sum_{i=1}^{6} \alpha_i V_i,$$

where α_i (positive for odd i and negative for even) are proportionality constants that also compensate for a small asymmetry between the coils.

When the magnet is superconducting and the inductive voltages across the coils are balanced, $V_{out} \approx 0$. If a quench starts in one of the coils (j), the non-zero resistive component V_j^R will produce an output voltage $V_{out} = (-1)^{j+1} V_j^R \neq 0$, that serves as an indication of a quench. As will be described, the unipolar discriminators used in the system also require the inverse output, $\overline{V_{out}}$.

The outputs of the quench detection circuit, V_{out} and $\overline{V_{out}}$ are directed to the trigger circuit shown in Figure 2.22. The combination of two discriminators, logic converters and an “OR” produces a TTL pulse whenever $|V_{out}| > V_t$, where V_t is the discriminator threshold. This pulse is stretched to a width of 75 μs and then buffered through a unity gain amplifier and transistor follower to produce a quench detection circuit trigger.

The quench protection circuit, shown in Figure 2.22, is designed to initiate the energy dissipation in the resistor R_D once a quench detection trigger occurs. Under normal operation, current flows through the power supply, Silicone Controlled Recti-

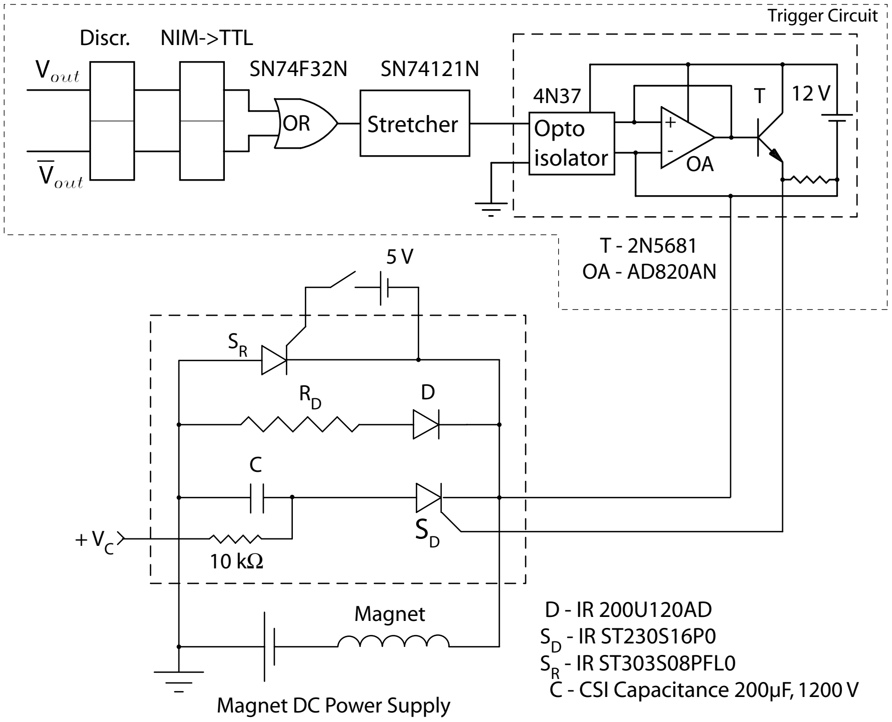

Figure 2.22: Quench protection circuit.

fier (SCR) S_R and the magnet[13]. A capacitor C, charged by an external power supply to $V_C = 100$ V, is prevented from discharging by an SCR S_D. The arrival of a quench detection trigger on the gate of S_D initiates a discharge of the capacitor C through the magnet for some period of time. While the capacitor is discharging, the SCR S_R is inversely biased, bringing it into a non-conducting state. Diode D prevents the capacitor from discharging through resistor R_D. Following the discharge of the capacitor, the current flows through the magnet, resistor R_D and the diode.

The training curve (dependance of the quench current on the quench number) of quadrupole coils, quadrupole assembly, solenoids and the assembled magnet is

---

[13] A small portion of the current also frows through the resistor R_D and diode D, due to a somewhat larger potential drop across the S_R in its open state.

described in Ref. [55]. The magnet has never reached its design load line of 320 A. The efficiency of the quench detection circuit drops with increased operating current, reaching about 55 % for the maximum achieved current of 180 A.

During the latest operation cycle, the magnet quenched multiple times at 160 A and this value was used as an operation current for all trapping data described in this thesis.

2.5 Cryogenic Apparatus

As was mentioned in Chapter 1, the experimental cell must be cooled to a temperature below 300 mK. This temperature can be achieved through the use of a dilution refrigerator. Excellent reviews of the physics behind the operation of a dilution refrigerator as well as numerous practical examples can be found in Refs. [76] and [77]. Dilution refrigerators were originally developed in late 1960s and are now available commercially for general laboratory use. The refrigerator design can be customized to satisfy a wide variety of experimental requirements. The dilution refrigerator that is used in this experiment[14] is a continuous flow refrigerator specified to have a cooling power of 400 μW at 120 mK.

The dilution refrigerator resides inside the vertical section of the cryostat (see Figure 2.23). The cryostat design consists of several vacuum-insulated nested shells, with each inner shell at a succeedingly lower temperature. In any design, significant consideration must be made to address the issue of heat loads. There are several sources of heat. First, heat is conducted through the materials connecting pieces

---

[14] Kelvinox 400 manufactured by Oxford Instruments.

of the apparatus at different temperatures. To minimize these loads, one must select materials that have low heat conductivity (such as plastics, glasses, and “dirty” metals) and reduce the cross section of the interconnections or increase their length. Secondly, heat is conducted through the residual gas between the shells. The pressure in the vacuum space between the shells is lowered to below 1 Pa before cooldown. Charcoal sorbs are also installed in the vacuum chamber to absorb gas in th event that a small leak develops during the initial cooldown. A third source of the heat is black-body radiation. To reduce this component, one must use shells at intermediate temperatures in addition to reducing their wall emissivity. The reduction in emissivity is accomplished by wrapping the shells with several layers of aluminized mylar film, also known as “superinsulation”. The problems with black-body heating become especially acute at the large aperture optical access into the apparatus.

The cryogenic apparatus used in our experiment is shown in Figure 2.23. The details of the seal design, including the design of the sliding seals in the vertical section of the apparatus, can be found in Ref [53]. The dilution refrigerator is located in the vertical section of the inner vacuum chamber (IVC). The experimental cell is placed in the horizontal section, centered along the neutron beam path. The cell is filled with isotopically pure ^{4}He, also serving as the heat link to the mixing chamber of the dilution refrigerator. Several bellows are incorporated in the heat link design in order to allow position adjustment of the cell and to relieve thermal stresses during the cooldown.

Surrounding the IVC is the liquid-helium filled bath (main bath) housing the superconducting magnet assembly. The temperature of this bath is close to the

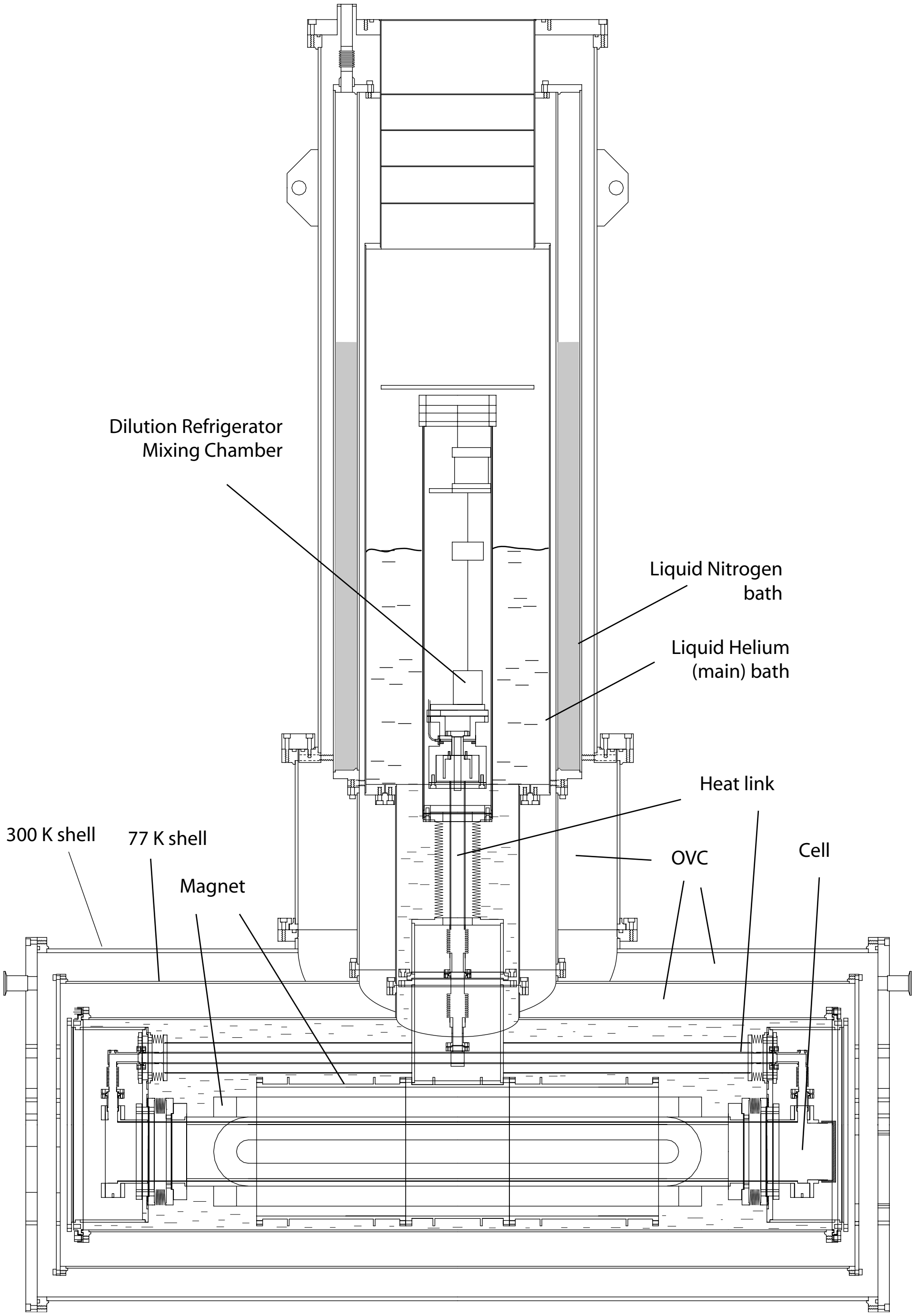

Figure 2.23: Sketch of the cryogenic apparatus. Details of the design can be found in text.

equilibrium temperature between the liquid helium and its vapor at atmospheric pressure, about 4.2 K. Main bath has several access ports on the top for liquid helium transfers, helium gas exhaust, and for insertion of cold traps for cleaning the helium mixture circulating through the dilution refrigerator.

Liquid nitrogen, extending throughout most of the vertical section and into the 2.5 cm diameter copper tubing extending to the end flanges of the horizontal section, maintains the temperature of the nitrogen shield close to 77 K, thereby reducing the heat load on the helium bath. Although the nitrogen shield is made of aluminum, a material that has a high heat conductivity, “direct” cooling of the end flanges through the copper tubing proved to be essential to avoid large temperature gradients in the shield [54].

The outer (300 K) shell, also constructed from aluminum, is designed to maintain vacuum in the outer vacuum chamber (OVC), a space between the 300 K shell and the main bath.

In order to bring neutrons into the trapping region, they must pass through a set of windows. These windows must satisfy several criteria: they need to pass the 0.89 nm neutron beam, be vacuum-tight, not transmit infrared black-body radiation, not contain materials that will activate under neutron irradiation , especially with a lifetime similar to that of the neutron lifetime and not have strong neutron-induced luminescence properties. These criteria substantially limit the choice of available materials. In fact, we have not been able to identify a single material that satisfies all of the above mentioned requirements. We have determined, however, that a combination of teflon and beryllium provides an acceptable solution. Perfluoro alkoxy

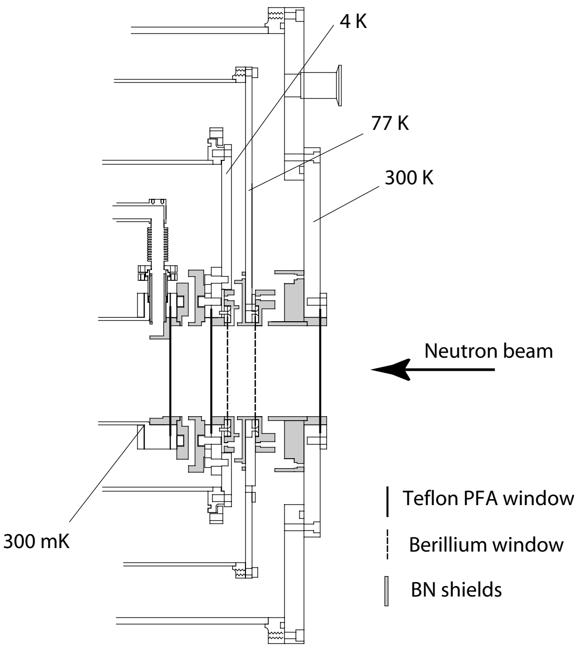

Figure 2.24: Sketch of the neutron entrance windows and the neutron absorbing BN shields used to protect flanges of the apparatus from neutron-induced activation.

alkane (PFA) Teflon, with a stoichiometry $(C_2F_3OR_f[C_2F_4]_n)_m$, satisfies all the criteria, except blocking infrared radiation. The infrared radiation is blocked by a separate 0.05 mm thick beryllium foil. Since beryllium (and beryllium monoxide which is easily formed on the surface of the beryllium after its exposure to the atmosphere) is extremely toxic through inhalation and ingestion and harmful through skin contact, it is enclosed inside a 25 μm thick teflon film. Beryllium neutron entrance windows are used on both the 77 K flange and the 4 K flange (see Figure 2.24).

In order to prevent activation of the cryostat end flanges on the neutron entrance side of the apparatus, several neutron absorbing boron nitride[15] shields are used. The configuration of these shields is shown in Figure 2.24. The shields guarantee

---

[15] BN Grade AX05, purchased from Saint-Gobian Advanced Ceramics Corp.

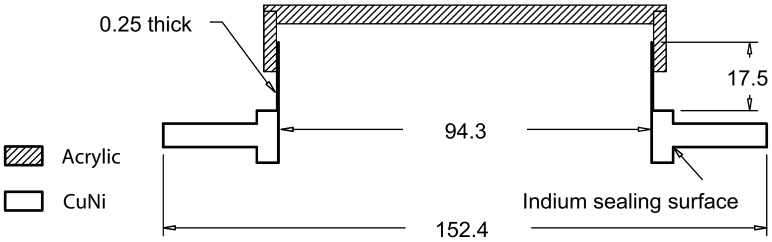

Figure 2.25: Drawing of the snout installed on the detector side of the cell. All dimensions are in mm. Both the acrylic-acrylic and the acrylic-metal joints are made with Stycast 1266 epoxy. The clearance between the acrylic and metal fin is 0.05 mm.

that no neutron in the beam or scattered by the windows can reach the flanges of the apparatus without making at least two reflections off the boron nitride, where most likely it will be absorbed.

The experimental cell is placed inside a 1 mm thick 1.13 m long 70-30 copper-nickel tube. Two identical end caps, also made from copper nickel, are soldered to both ends of the tube, providing sealing flanges. Copper nickel is chosen for its solderability and high resistivity that is necessary to reduce eddy current heating while ramping the magnetic field. A compression seal is made on the neutron entrance side of the apparatus between the 0.5 mm thick teflon window and the end cap [78]. The copper nickel tube is suspended from 0.4 mm diameter kevlar strings attached to the 4 K housing. The cell positioning system is identical to the one described in Ref [54]. The heat load onto the cell due to the kevlar strings is about 15 μW [54], well below the cooling power of the refrigerator at our operation temperatures.

On the opposite side of the cell, an indium seal is made between the endcap of the copper-nickel tube and the "snout" shown in Figures 2.25 and 2.26. A glue joint between the acrylic window and a thin metal fin is made using Stycast 1266 epoxy. The surfaces are roughened with sand paper before gluing to provide better glue bonding. When cooled, the acrylic contracts more than most metals, but the flexibility of the fin allows the seal to remain intact. We have used snouts made from copper nickel, stainless steel and aluminum. It was observed that the glue joints made to copper nickel and stainless steel snouts have a tendency to partially delaminate after the first cooldown, thereby exhibiting higher failure rate on successive cooldowns. The aluminum snout does not exhibit such behavior, most likely due to the better match between the thermal expansion coefficients of aluminum and acrylic.

Inside the copper nickel tube, there are closely fitting concentric tubes of boron nitride and graphite as shown in the inset in Figure 2.31. These tubes are made of interlocking sections that are machined from a solid cylinder. The length of each BN section is roughly 30.5 cm,and the thickness is 3.4 mm. Boron nitride is used to absorb scattered neutrons; the absorption length for 0.89 nm neutrons is about 60 μm. The graphite tubes, about 15 cm long and 1 mm thick, are used for blocking the luminescence produced by the boron nitride following neutron absorbtion [79]. A detector insert defining the detection region of the trapped neutrons is placed inside the graphite tubes and is centered axially in the copper nickel tube with respect to the magnet assembly. The detector insert and the material selection process are described in additional detail in Section 2.6.

A 40.6 cm long, 8.6 cm diameter ultra-violet transmitting (UVT) acrylic light guide extends from the end of the detection region to the snout window (see Figure 2.26). A boron oxide disk[16] of the same diameter and thickness of 1.2 cm is attached to the end of the light guide, opposite to the snout. This disk acts as a neutron

---

[16] Boron Trioxide (B_2O_3), 99.9999 % pure, purchased from All-Chemi Ltd., Mt. Pleasant, SC.

beam stop; most neutrons entering the cell reach the disk and are absorbed. Boron oxide is optically transparent, but also hygroscopic. Within minutes after exposure to the atmosphere it reacts with the atmospheric water forming boric acid and thus clouds up the surface of the crystal and reduces the light transmission. Nevertheless, if polished and kept in a water-free environment, boron oxide remains transparent to visible light. Subsection 2.6.1 provides more detail about the requirements for the beam stop material.

The light emitted in the trapping region is transported by the cell light guide, passes through the acrylic window of the snout, through the single crystal quartz and acrylic windows at 4 K and into the acrylic light guide that extends from 77 K flange to the room temperature region, as shown in Figure 2.26. At room temperature, the light is split into two photomultiplier tubes (PMTs) (see Section 2.6).

The two windows mounted on the 4 K flange consist of a 1.5 mm thick, 15.2 cm diameter single crystal quartz[17] window and a 6 mm thick 19 cm diameter acrylic windows. In addition to providing a vacuum seal between the IVC and OVC, the acrylic window blocks black-body radiation from the 77 K light guide. Due to the large diameter of the window combined with the low thermal conductivity of the acrylic, the temperature of the center of the window without the quartz was found to be significantly higher than the temperature of the end flange, thus creating a high heat load on the cell.

Quartz also blocks black-body radiation, but not as efficiently as the acrylic. The thermal conductivity of the single crystal quartz in the 7 K to 15 K range is about $10\,\mathrm{W\,cm^{-1}\,K^{-1}}$, a factor of 10^4 larger than that of the acrylic. We thus use the quartz

---

[17] Purchased from Sawyer Research Products.

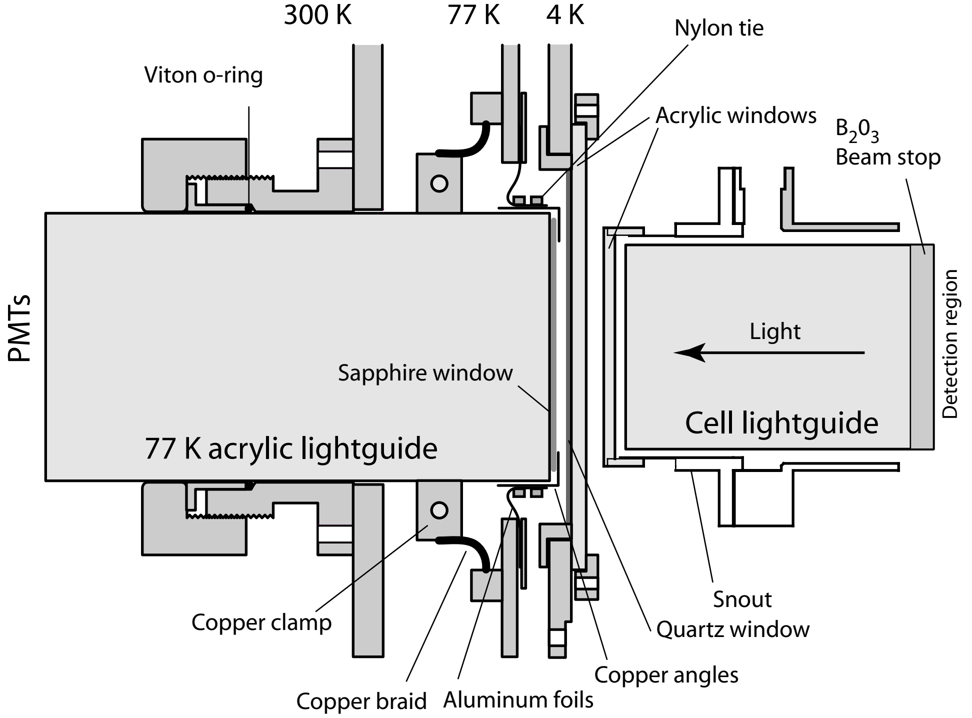

Figure 2.26: Light path from the trapping regions into the photomultipliers.

window to remove most of the black-body radiation, thereby significantly decreasing the heat load onto the acrylic.

The quartz window is thermally anchored to the 4 K end flange with twenty 0.125 mm thick, 1.5 cm wide and about 3 cm long copper foils as shown in Figure 2.27. Gore-Tex gasket material is used to maintain compression between the copper foils and quartz to minimize stresses on the quartz window. This compression scheme does not guarantee a good thermal contact between the quartz and acrylic in the center, but in this setup the quartz blocks 95 % of the infrared heat from 77 K light guide (transmission band of a single crystal quartz is 0.15 μm–3.3 μm) such that the heat load from the acrylic window allows us to cool the cell to below 300 mK.

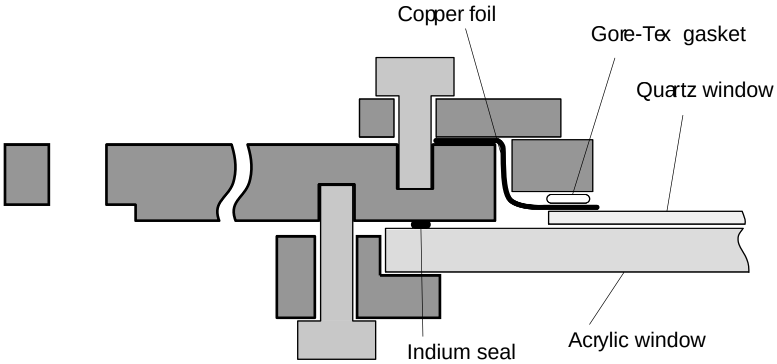

Figure 2.27: Details of the quartz/acrylic window assembly at 4 K flange.

One end of the 77 K light guide is thermally anchored to the 77 K flange as shown in Figure 2.26. As with the 4 K acrylic window, the poor thermal conductivity between the center of the guide and its edge creates an area in the center of the light guide that has an unacceptably hight temperature of 195 K. In the past, this problem was addressed by cooling the center of the guide through a “mesh” of copper wires glued into grooves machined in the front surface of the guide [54]. Although adequate for cooling purposes, the copper wires partially block light from the cell and thus reduce the detection efficiency of the cell. The need for these wires is eliminated by using a 0.5 mm thick, 100 mm diameter sapphire window[18] that is spot glued to the center of the light guide using optically clear Stycast 1266 epoxy as shown in Figure 2.28. The edges of the sapphire window are thermally anchored to the light guide by six copper angle brackets that press the window against the surface of the light guide. The brackets are attached using 4-40 nylon screws tapped into the acrylic. The copper brackets extend under the aluminum foils that are compressed

---

[18] Purchased from Valley Design Corp., Santa Cruz, CA.

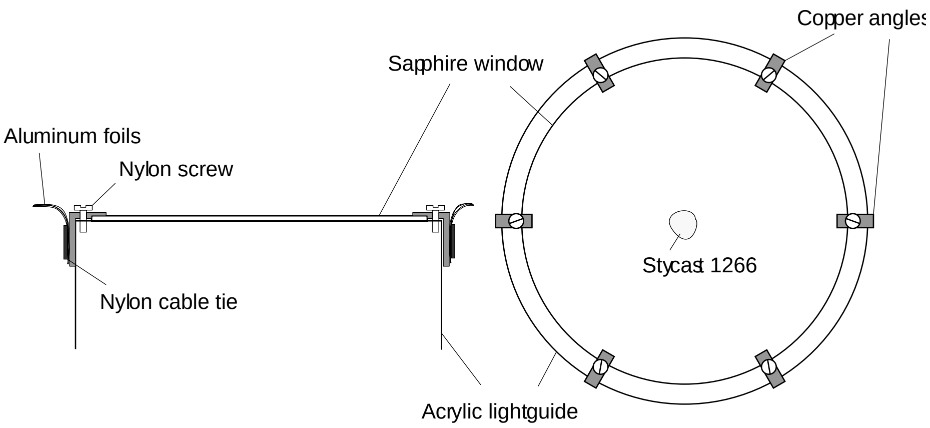

Figure 2.28: Sketch of the sapphire window attached to the 77 K light guide to cool its center.

to the radial surface of the light guide with a nylon cable tie. The aluminum foils are thermally connected to the 77 K end flange. When cooled, the nylon cable tie contracts more than the acrylic, thus improving the thermal contact between the aluminum foils and the acrylic.

The temperatures of both ends of the cell and the 4 K and 77 K end flanges on the detector side are monitored using silicone diodes that operate in 1.4 K to 300 K range. Below 1.4 K, the temperatures of the cell, heat links and the mixing chamber is determined using RuO_2 and $Bi_2Ru_2O_7$ resistors. A low-excitation four-wire AC bridge scheme used for measuring resistances allows us to avoid problems with resistive heating and the temperature dependance of the lead resistances [77]. Several resistors mounted on the cell, heat link and the buffer cell are connected in a two-wire measurement scheme and can be used as heaters.

All wiring to the thermometers is done with thin 0.1 mm diameter manganin wires. The low thermal conductivity of the manganin reduces the heat load on the cell. Both diodes and resistors are glued with Stycast 2850 to copper pieces that can be attached with a screw to the surface. Mutipin[19] electrical connectors are used to connect the leads to the thermometers.

Two charcoal sorbs with an estimated helium capacity of 2 g are installed in the OVC. In addition, there are three sorbs in the IVC. One is installed on the 1K pot and one on each side of the horizontal section of the IVC. The sorbs in the horizontal section are thermally decoupled from the main helium bath by 2.5 cm long nylon 4-40 screws. Heaters installed on these sorbs are used to "clean" them.

It takes about four days to cool down the apparatus from the room temperature to the base operating temperature. A typical cooldown starts by leak testing the apparatus at room temperature. All seals between atmosphere and the OVC and IVC and between the main helium bath and the OVC and IVC are tested using a helium leak detector. Because of the high permeability of helium through the teflon window on the cell, leak tests between the cell and the IVC are not possible at this temperature; these leak tests are performed at a lower temperature when teflon permeability becomes negligible. After the apparatus is leak tight, about 1 torr of neon exchange gas is administered into the IVC and liquid nitrogen is then transferred into the nitrogen jacket and main bath. The resistance of the magnet is a good indicator of its temperature; the resistance changes from 574 Ω at 300 K to about 70 Ω at 77 K. Typically the transfer results in an excess of liquid nitrogen in the main bath. This nitrogen is removed by sealing the main bath and pressurizing it with helium gas while the tube that extends to the bottom of the bath is left open to let the liquid nitrogen out. Small amount of liquid that remains after this process

---

[19] Purchased from Microtech Inc.

is removed by pumping on the main bath with a vacuum pump. The neon exchange gas is then evacuated from the IVC and leak checks — this time including the leak check from the cell into the IVC — are repeated. Once the leak checks are complete, about 100 mbar of isotopically pure helium is left in the cell as an exchange gas.

Helium exchange gas is put into the IVC before the liquid helium transfer to provide cooling of the cell and the dilution refrigerator. Liquid helium is then transferred from a transport dewar through a flexible transfer line into the main bath. Slow transfer, with a pressure difference between the transport dewar and the main bath of less than 0.05 bar, typically results in a more efficient helium consumption; during a transfer with a high flow rate, cold helium gas leaves the main bath without complete thermalization with the magnet and other parts of the apparatus. The initial helium transfer uses approximately 250 liters of liquid helium and lasts for about 8 hours. Two superconducting helium level meters installed in the vertical section of the main bath allow the helium level in the bath to be monitored.

Once the helium transfer is complete, the helium exchange gas is removed from the IVC using a turbo pump. In order to remove the residual helium gas, it is necessary to pump on the IVC for an extended period of time, typically about 24 hours. On several occasions when this procedure was not followed, the base temperature of the fridge could not be reached or its performance rapidly deteriorated after several days of operation, most likely due to condensation of the helium left in the IVC on the components of the dilution refrigerator. Once superfluid, this helium may thermally short parts of the refrigerator, causing a deterioration in its performance. Following the exchange gas pumping a final leak check between the cell and the IVC is performed.

The cell is filled with isotopically pure ^{4}He. The isotopic purification of natural helium was performed at the University of Lancaster, UK using a heat flush technique [65]. This technique is based on the fact that ^{3}He atoms are interacting with phonons in the superfluid ^{4}He and can be carried away by a “wind” of phonons. The remaining solution is then depleted in ^{3}He. The ^{3}He to ^{4}He ratio in the gas used in our experiments was measured at Argone National Laboratory using accelerator mass spectrometry. Although the final measurements are not completed, preliminary results indicate that the ^{3}He to ^{4}He ratio is less than 2.5×10^{-13} [64].

The isotopically pure helium is stored at room temperature in four 0.45 m^3 stainless steel tanks at a pressure of about 3 bar. All four tanks are connected in parallel to the gas handling system, as shown schematically in Figure 2.29. The gas handling system is a closed system that allows condensing of the helium into the cell and then removing it back into the storage tanks. A liquid helium cold trap is used to cryoclean the helium gas from any impurities before it enters the cell. A needle valve provides control of the helium flow when the pressure difference between the tanks and the cell is large. As condensing progresses, the pressure difference between the tanks and the cell decreases. A sealed diaphragm pump is then used to increase the gas pressure on the room temperature side. The same pump, acting like a compressor, can be used to remove the helium from the cell and back into the storage tanks. In order to prevent the failure of the snout glue joint, the pressure inside the cell is kept below 1 bar at all times.

There are three capillary tubes going into the cell. Two of them (“fill” lines) are

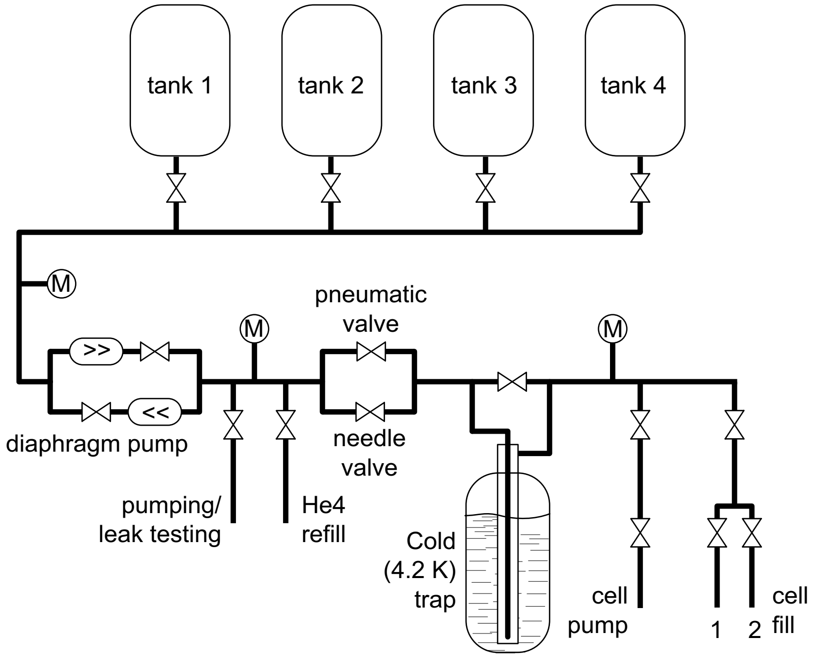

Figure 2.29: Gas handling system for the isotopically pure helium.

1.6 mm in diameter, a third one ("pump" line) has a diameter of 3.2 mm. Isotopically pure helium is condensed from the dumps into the cell through the fill line, while the bigger diameter line is used for initial leak testing and the removal of the helium from the cell. The issue of heat loads introduced by helium film dynamics inside the pump line was solved by thermal anchoring of the line and installation of a 0.6 mm diameter pinhole aperture to restrict internal gas circulation [54]. The fill and pump lines terminate into a copper "buffer volume" that is in a common volume with the cell and is attached to the bottom of the mixing chamber. A heat link consisting of several large diameter (15 mm to 22 mm) copper nickel tubes and bellows connects the buffer volume to the cell. Initially, when the heat link is filled with helium gas, the cell is cooled through convective flow. When enough helium is condensed such that

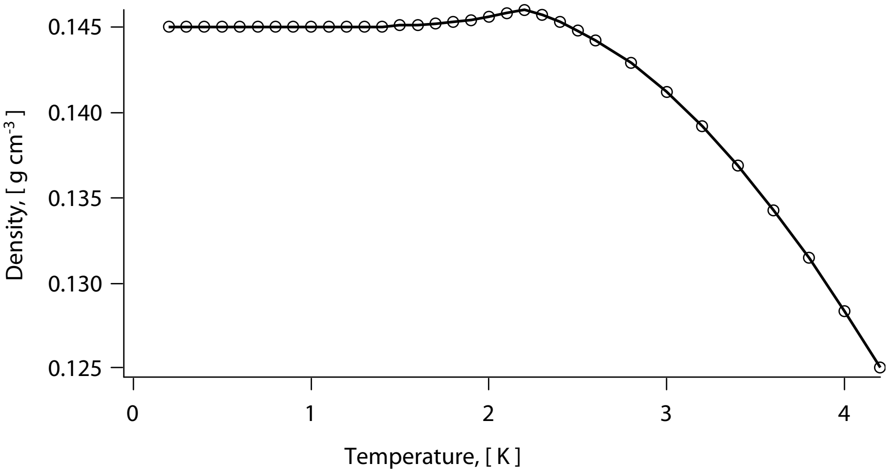

Figure 2.30: The density of liquid ^{4}He under a saturated vapor pressure as a function of temperature. Data is taken from Ref. [80].

the liquid reaches the buffer volume, cooling is provided through the liquid. The temperature dependence of the density of the helium (Figure 2.30) facilitates convective cooling at temperatures above the superfluid transition temperature; helium cooled by the mixing chamber is more dense and will have a tendency to move into the lower regions of the cell. In order to address the issue of the phonon spectrum mismatch between the solids and liquid helium at low temperatures (known as Kapitza resistance), two sintered silver fins are installed in the buffer volume [55]. Compact in size, they have large surface area to minimize the effects of this boundary resistance and thus improve the heat flow between the mixing chamber and the cell. The measured conductance of the heat link at low temperature is $(0.81 \pm 0.04)T^3$ W/K [55].

The total volume of the cell, heat link, and buffer volume is about 8 liters. Initially, the helium level in the cell can be observed through the light guide. The helium level in the heat link and the buffer volume can not be viewed optically so one must rely on other means. Although the buffer volume provides some flexibility in the amount of helium that needs to be condensed in the cell, a capacitance-based level meter is installed in the buffer volume to determine the moment when it is full. Overfilling the cell causes a thermal short between stages of the refrigerator through the pump and fill lines. The situation is complicated by the temperature dependance of the liquid helium density shown in Figure 2.30. The volume of liquid helium may change by several tenths of a liter when the cell is cooled.

In practice, the level meter proved to be unreliable due to frequent electrical shorts. Fortunately, the moment when the level of liquid helium reaches the buffer volume can be determined by the temperature behavior of the buffer volume and the cell. When there is no liquid in the buffer volume, there is a large temperature gradient between the buffer volume and the cell (the thermal conductivity through the helium gas decreases as the temperature drops). As condensing progresses, the helium liquid reaches the buffer volume and sintered fins, leading to a rapid equilibration of the temperatures of the buffer volume and the cell. This equilibrium condition serves as an indication to stop condensation.

2.6 Detection System

The detection of neutron beta-decay events inside the trapping region is based on registering the intense flashes of scintillation light from the superfluid liquid helium produced by the decay products.

A large fraction of the energy released during neutron decay is carried away by the electron and antineutrino. The electron spectrum is continuous, with an average electron energy of 270 keV and extending up to 782 keV (see Figure 2.33). Following a neutron decay, the decay electron decelerates in the liquid helium, having an average energy deposition of 50 $\mathrm{eV}\,\mu\mathrm{m}^{-1}$. The electron creates a track of excited helium atoms, ions and electrons. The dynamics inside the track is complicated, the primary electron produces secondary electrons with enough energy to ionize the helium [81, 82], but the recombination of helium ions and electrons leads to creation of He_2 molecules. Both singlet and triplet molecules can be created. Within 10 ns, the molecules in the singlet state cascade to the lowest excited state and undergo a transition into the ground state $\mathrm{He}_2(A^1\Sigma_u^+) \rightarrow \mathrm{He}_2(X^1\Sigma_g^+)$ with the emission of an ultraviolet photon with wavelength of 60 nm to 100 nm. The lifetime for radiative decay of the triplet molecules is considerably longer, roughly 13 s [83].

Since the energy of the UV photon (12 eV to 20 eV) produced during the singlet molecule decay is less than the 20 eV energy of the first excited helium state, helium is transparent for these photons.

As much as 35 % of the total energy deposited by the primary electron in helium is emitted in UV light within 10 ns of the ionization event [84, 55]. Roughly 22 UV photons per keV of primary electron energy are produced in the prompt pulse. The prompt component is followed by a “tail” of photons produced during the decays of the triplet metastable molecular and atomic helium states [81]. These events are single photon events that are typically not detected by our data acquisition system discussed in Chapter 3.

Several techniques have been considered and tried over the years for effective detection of scintillation events in liquid helium. Due to the lack of materials that can effectively transmit and reflect UV light in 60 nm to 100 nm wavelength region, all the techniques use a wavelength shifting material that absorbs the UV light emits visible light. The organic fluor tetraphenyl butadiene (TPB) is chosen as our wavelength shifting material due to its high fluorescence efficiency (1.35 ± 0.1) [85][20]. A detailed account of the history of the development of our detection system can be found in Refs. [53, 55, 86]. In the geometry of the present approach, where the length of the detection region is comparable to its diameter and an optically clear neutron beam stop is used, TPB evaporated onto a Gore-Tex tube provides the highest light output for an average neutron decay event.

TPB is evaporated onto each of two 17.5 cm by 26.5 cm by 1 mm thick Gore-Tex sheets. The Gore-Tex sheets are then rolled in a tube and placed next to each other creating a 35 cm long 8.4 cm diameter detector insert that is positioned inside the cell as shown in Figure 2.31. The density of the TPB coating is between 0.2 $\mathrm{mg\,cm^{-2}}$ and 0.4 $\mathrm{mg\,cm^{-2}}$. Once the TPB evaporation is performed, care is taken to minimize exposure to UV light, such as produced by the sun or by certain light fixtures, as it deteriorates the wavelength shifting performance of the material. Although quantitative studies of this effect have not been performed, we have observed that long-term (weeks) exposure to UV light significantly decreases the fluorescence efficiency of the TPB. We thus keep the light exposure to a minimum.

UV photons produced in the helium reach the TPB coating where they are converted into visible light with a spectrum centered at approximately 430 nm (the width of the spectrum is roughly 50 nm) [87]. A portion of this light, possibly after undergoing one or more diffuse reflections from the walls of the detector insert, passes

---

[20] Fluorescence efficiency is the ratio of the number of photons emitted by the material to the number of excitation photons.

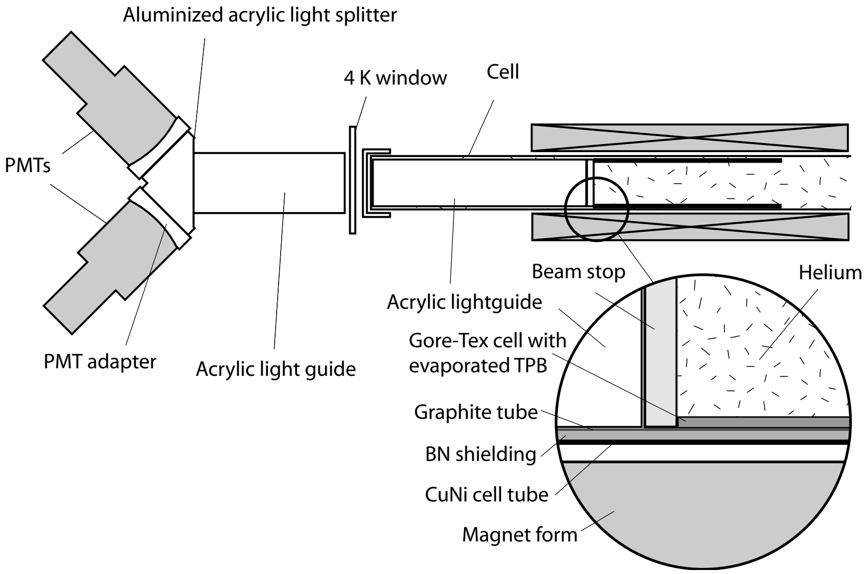

Figure 2.31: Sketch of the light detection system.

through the optically transparent neutron beam stop and into a 40.7 cm, and 8.7 cm diameter ultra-violet transmitting (UVT) acrylic light guide, where it may undergo total internal reflections before reaching the end of the cell. The reflection of light from the TPB coating is very diffuse, as shown by the reflectance factor shown in Figure 2.32. This results in a substantial decrease of detection efficiency with an increase in distance between the place of the decay and the beam stop. The efficiency of the system is determined experimentally by moving a beta-active ^{113}Sn source inside the cell and measuring the light output produced by the 364 keV electrons emitted by this source. The results of these measurements are described in Section 4.10. Light exiting the end of the cell light guide travels through the acrylic snout window separating the cell from the vacuum chamber, through the acrylic and single crystal quartz windows at 4 K and then into the 77 K UVT acrylic light guide with a sapphire window attached to its face. The design of optical windows is discussed in Section 2.5. A 77 K

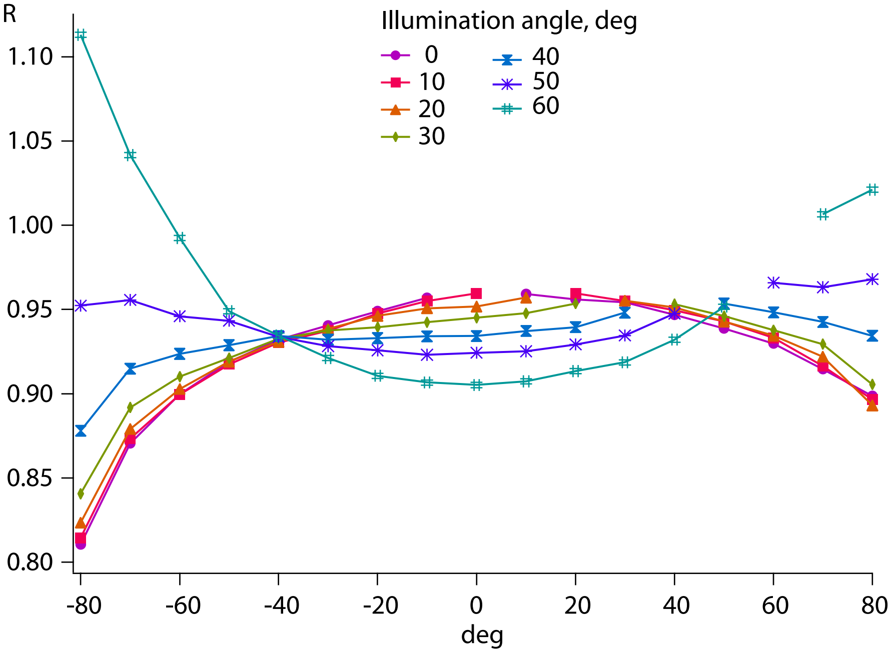

Figure 2.32: Reflectance factor of Gore-Tex with evaporated TPB for 430 nm light. The reflectance factor is defined as the ratio of the radiance of the actual surface to the radiance of an ideal Lambertian surface illuminated and viewed in the same manner.

lightguide, 35 cm long and 11.4 cm in diameter, extends outside of the apparatus and is couple to the PMTs as shown in Figure 2.31.

The light is split between two photo-multiplier tubes (Burle 8854) by an aluminized acrylic light splitter. Two plano-concave acrylic couplers are machined to match the convex windows of the PMTs and the flat surface of the light splitter. Optical grease is used between all surfaces at room temperature in order to decrease the light loss due to reflections on acrylic-air interfaces. The optical grease can not be used in vacuum or at low temperature.

The photomultiplier tubes are mounted inside light-tight aluminum cans. In order to protect the PMTs from the exposure to helium gas abundant in the ambient atmosphere due to the cryostat boil-off[21], the cans are kept overpressured by the continuous flow of nitrogen gas.

The anode current of the PMT is extremely sensitive to external magnetic fields; magnetic fields on the order of 0.1 mT can change the anode current by a factor of 2 [89]. Since PMTs are located in the proximity of the magnetic trap, measures to shield the magnetic field are necessary. Both active field compensation and passive shielding are implemented. The active magnetic field compensation is achieved by a 43 cm diameter 8.5 cm long solenoid with 400 turns of AWG14 copper wire mounted around the PMT cans so that the axis of the solenoid is collinear with the axis of the trap. The solenoid current is chosen to provide the maximum compensation as determined by the PMT pulse-height spectrum. The optimal current for our setup is 3.25 A. Passive shields are made from metal with large magnetic permeability. There are two layers of passive shielding. The first (tubular) layer surrounds the dynodes of the photomultiplier tubes. The second layer encloses the aluminum cans that house the PMTs and the light guides. A combination of these two methods reduces the effect of the changing magnetic field of the trap on the PMT counting rate to less than 5 %. Magnetic fields remain constant during the observation period of the experimental runs (see Section 4.1).

In order to veto muon events that produce scintillations in helium and acrylic, three muon detectors made from a 155 cm long, 32 cm wide, and 2.5 cm thick scintillator plates are placed under the apparatus and on its sides (forming "U" parallel to the neutron beam path). A forth muon detector covers the light splitter and part

---

[21] Helium can permeate the envelope of the PMT and produce an excessive afterpulsing due to the photocathode ion feedback or even cause a complete electrical breakdown [88].

of the 77 K light guide that extends outside of the 300 K end flange (see Figures 2.26 and 2.31). More details about the construction and placement of the muon detectors can be found in Ref. [53].

2.6.1 Material Selection for the Detector Insert

There are strict limitations on the materials that can be used inside the cell. Most of these limitations come from the necessity to minimize the neutron-induced backgrounds (i.e activation and luminescence), although other aspects are also important. All materials must be non-magnetic since the magnetic field inside the cell exceeds 1 T. In addition, materials need to be machinable and compatible with a low temperature environment since the cell is cooled to below 300 mK.

The requirements of minimizing the neutron-induced backgrounds however is the most stringent. During trap loading, $\sim 10^8$ neutrons per second enter the cell. The majority of these neutrons are absorbed by the B_2O_3 beamstop or scatter in the helium and are absorbed in the walls of the cell. Neutron activation of the beamstop and all materials present in the cell may result in higher backgrounds; the helium scintillation signals resulting from background events such as betas decays of the activated materials and gamma Compton-scattering in the helium are indistinguishable from neutron beta decay events. Any time-dependent background can give rise to a "false signal" and thus introduce a systematic error in the measurement. Especially problematic are isotopes with lifetimes comparable to that of the neutron.

In addition to activation, neutron-induced luminescence also produces light that can be detected by the photomultiplier tubes [79, 90]. Although the effect of the luminescence is significantly reduced by requiring coincidence between two PMTs, an intense luminescence may still be a concern due to accidental coincidences or PMT gain shifts. We thus either choose materials that exhibit minimal luminescence or shield the light from the materials that luminesce strongly.

To study the luminescence properties of materials present in the cell, a small test apparatus was constructed. In this apparatus, a sample of material is cooled to below 5 K and the light emerging from the sample after neutron irradiation is transported from the cryostat using an acrylic light guide and detected either by one PMT or by two PMTs in a coincidence geometry similar to that of Figure 2.31.

The following materials have been tested: boron nitride (BN), lithium fluoride (LiF), boron oxide (B_2O_3), boron carbide (B_4C), polymethyl methacrylate (PMMA or acrylic), expanded polytetrafluoroethylene (PTFE) with an evaporated coating of the TPB, boron/lithium loaded glass[22] and graphite. A detailed description of these studies can be found in Refs. [54, 90].

Strong luminescence (with an initial photon counting rate of 10^5 s^{-1}) following the capture of about 10^{11} cold neutrons, is observed for boron nitride and lithium fluoride. No luminescence was observed for boron carbide. Although we would prefer to use B_4C as a neutron shielding material in our detector, it is very difficult to machine and it is cost prohibitive to produce a tube of B_4C using other techniques. Boron nitride, on the other hand, is easily machinable. We have shown that the luminescence light emitted by boron nitride can be blocked by a 1 mm layer of graphite. Both graphite and a sample of BN enclosed in graphite have been shown to not to luminesce under

---

[22] The neutron absorbing glass was specially fabricated to have low activation. Its approximate composition is 70 % B_2O_3, 27 % Li_2O, and 3 % ZrO_2 by weight [55, 91].

neutron irradiation. Thus, a composite BN/graphite shield is chosen for shielding the copper nickel tubing and magnet from scattered neutrons.

The neutron beamstop is located at the end of the detection region must satisfy all the requirements mentioned above plus it must be optically transparent. We studied three materials for the beamstop: LiF, a B.Li glass, and B_2O_3. Lithium fluoride exhibits a strong luminescence signal and is activated by the $^{19}F(n,\gamma)^{20}F$ reaction. Although the lifetime of ^{20}F is 16 s (considerably shorter than the neutron beta-decay lifetime of 886 s), this activation is still a concern. Boron/lithium glass does not luminesce, but it is subject to activation by $^{6}Li(n,T)^{4}He$ reaction, followed by $^{16}O(T,n)^{18}F$. The count rate of the ^{18}F signal (several kHz) after the 15 minute exposure to the neutron beam, combined with its lifetime of 9500 s [55] make it a poor choice as the material for the beamdump. Boron oxide displays a weak time varying signal that could arise from either activation or luminescence. The intensity of this signal relative to lithium fluoride is about three orders of magnitude less. As all boron compounds, boron oxide may produce ^{13}N by the combination of the $^{10}B(n,\alpha)^{7}Li$ reaction with the $^{10}B(\alpha,n)^{13}N$ reaction. The ^{13}N then decays by positron emission with a lifetime of 863 s [92]. The efficiency of this process was measured in a separate set of experiments by irradiating a boron oxide sample in a neutron beam and detecting the time dependent signal from 511 MeV gamma rays produced in the positron-electron annihilation. The rate of ^{13}N production in these materials is found to be (1 to 2)$\times 10^{-10}$ per captured neutron [93]. From these three potential candidates for the beamstop, boron oxide is chosen because it shows the lowest level of activation and luminescence.

One additional possibility to stop the neutrons is to use the cell acrylic ($C_2H_8O_2$) light guide. The neutron absorption cross section on the acrylic is dominated by the absorption on hydrogen and is roughly 13.3 b for 0.89 nm neutrons. The coherent scattering cross section is 167 b. Using the density of the acrylic of 1.2 $\mathrm{g\,cm^{-3}}$, the absorption mean free path of the neutron in the lightguide may be estimated as $\lambda_{abs} \approx 10.4$ cm. The mean free path between scattering events is shorter, roughly $\lambda_{sct} \approx 8.3$ mm. Thus the diffusion length may be estimated as $\sqrt{\lambda_{abs}\lambda_{sct}} \approx 3$ cm. The neutrons scattered by the acrylic into the wall will be absorbed by the boron nitride shielding. The primary concern in this scheme is the purity of acrylic and possible long-term deterioration of its optical properties.

None of the weak neutron absorbers studied (acrylic, TPB evaporated on GoreTex) displayed any detectable neutron-induced luminescence.

2.6.2 Detector Calibration Setup

The calibration of the detection system is performed using a ^{113}Sn radioactive source. This isotope decays by electron capture, producing an excited state of ^{113}In that subsequently undergoes a transition into a stable state with an emission of a 364 keV conversion electron with a probability of 29 % (388 keV, 6 %; 392 keV gamma, 65 %) [94]. The half life of ^{113}Sn is 115 days. The source is immersed in liquid helium and is located along the center axis of the detector insert described in Section 2.6. Betas released by the source create scintillation light in the helium similar to that produced during neutron beta decay.

The energy of the emitted electrons is close to the energy of the neutron decay

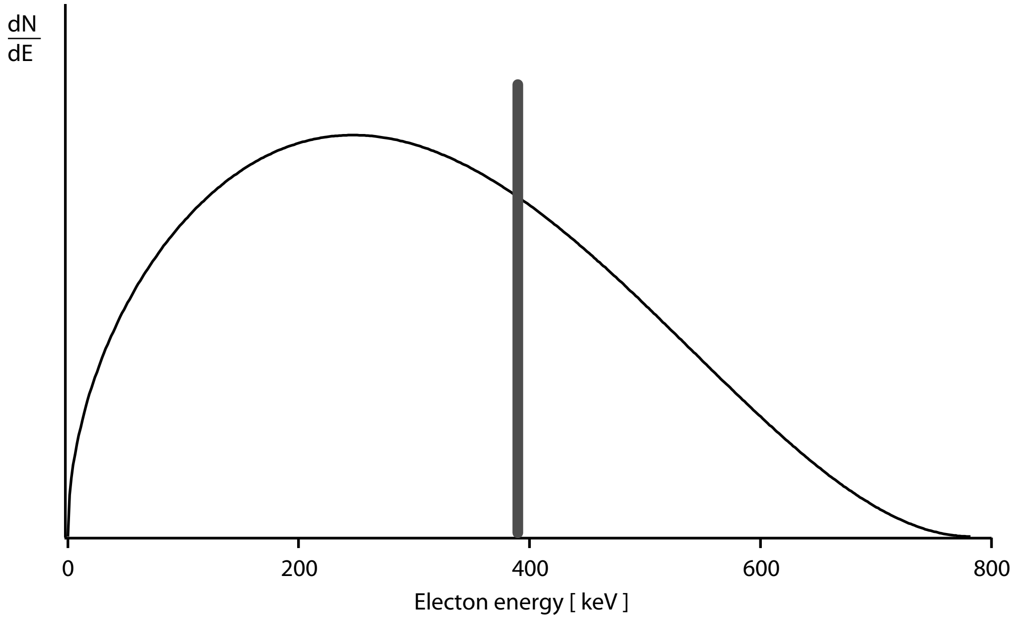

Figure 2.33: Neutron beta decay electron energy spectrum. The vertical line at 364 keV shows corresponds to the energy of the beta emitted by the ^{113}Sn source used for detector calibration.

electrons (see Figure 2.33). Since the intensity of the scintillations is proportional to the energy deposited in the helium, the neutron decay detection efficiency may be estimated based on the detection efficiency of the source electrons.

The isotope deposit[23] has a diameter of 5.08 mm. It is prepared using electroless deposition in the middle of the 2.5 cm diameter stainless steel disc and is covered by a film of acrylic with a mass density of 100 $\mu\mathrm{g}\,\mathrm{cm}^{-2}$. The activity of the source is 0.5 μCi (18.5 kBq).

The integrity of the source at low temperature was tested by rapid cooling to 77 K in a liquid nitrogen bath and comparing the source activity before and after cooling. No non-statistical discrepancies between the two measurements were observed, nor

---

[23] Purchased from Isotope Products Laboratories, Valencia, CA 91355. Catalog number ME-113.

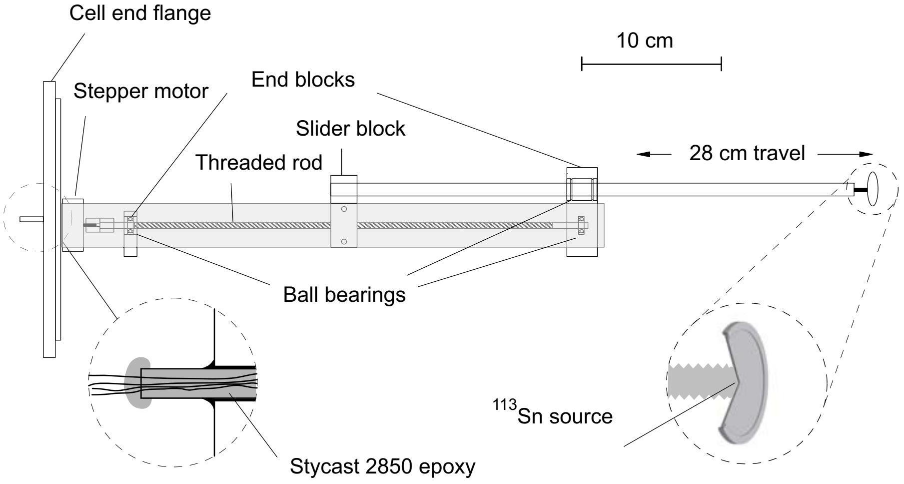

Figure 2.34: Sketch of the source mounting.

were there any traces of the radioactive material detected in the nitrogen container.

Since the neutron decay detection efficiency depends on the location of the decay event inside the cell, the calibration of the detection system is performed at several beta source positions. In order to move the source in cryogenic environment, a motorized linear motion assembly was constructed. The details of the construction are shown in Figure 2.34. The stainless steel disc with the source deposit is attached to a stainless disc of the same size that is soldered to a screw used for mounting the source. The shaft of the stepper motor is coupled to a 1/4-20 threaded brass rod. The ends of the rod are housed inside ball bearings pressed into two aluminum end blocks. The brass rod passes through the tapped hole in the aluminum slider block, thus translating rotation of the motor into linear motion of the slider. Attached to the slider is an aluminum tube that holds the source on the opposite end. When cooled, the aluminum shrinks more than the brass, thus ensuring the freedom of movement for the slider in the low temperature environment. Earlier attempts to use a steel shaft with the linear ball bearings were not successful since the ball bearing assembly contained plastic parts that shrink more than steel. In order to monitor the position of the source inside the detector insert, a rare earth magnet is attached to the threaded rod; the magnetic field measured by the Hall probe located outside of the dewar serves as an indication of the rotational position of the shaft and thus the position of the source. The assembly is supported from the cell flange with two stainless steel plates such that the source is located on the cell axis of the cell.

The coils of the stepper motor[24] are rewound with 100 μm diameter copper-clad Nb-Ti superconducting wire[25] in order to decrease the heat dissipation during the operation of the motor as described in Ref. [95]. The cell flange is modified to accommodate the electrical feedthrough for the motor current leads. A 1 cm long piece of a thin wall stainless steel tubing 3 mm in diameter is hard soldered to the flange and superconducting wires are brought through and sealed by filling the tube with Stycast 2850 epoxy as shown in the inset of Figure 2.34. A similar feedtrough is also made in the 4 K end flange. Copper wires AWG30 are used between the 300 K, 77 K and 4 K flanges.

The boron oxide beam dump in the calibration run was replaced by the same size acrylic disc. The transmission of the boron oxide was measured in a separate experiment.

Following the cooldown of the apparatus to 4 K, the cell was filled with natural abundance helium and further cooled to about 1 K for calibration measurements.

---

[24] Model PF 25-48 P4, purchased from Nippon Pulse America Inc.

[25] 55 μm diameter superconducting core wire with copper cladding to 80 μm purchased from Supercon Inc.

The results of the calibration run are presented in Section 4.10.

Chapter 3

Data Acquisition and Analysis

This chapter describes experiment control, data acquisition and the methods used to analyze the data. The electronics diagram and the data acquisition hardware are described in Section 3.1. The initial setup for digitizing PMT pulses was based solely on the Signatec PDA500 digitizing cards; the optionally of the concurrent digitization by the KAMFEE board was later added to the setup. The procedures for analyzing the Signatec cards data are presented in Section 3.2, the analysis of the KamFEE card data is discussed in Section 3.3.

3.1 Experiment Control and Data Acquisition

There are several computerized systems that monitor and maintain control of the experiment and collect experimental data.

The dilution refrigerator and some of the cryogenic and vacuum equipment are operated by several LabView routines running under SunOS 2.7 on a Sun SparcStation 5. The same computer monitors and records various operating conditions of the experiment, such as temperatures, pressures and cryogen levels in the apparatus and also the state of the NG6 and NG6-M neutron beam shutters (see Section 2.1). These parameters are typically logged every 60 seconds.

The control of the NG6-U neutron beam shutter, slider, superconducting magnet and high voltage PMT power supplies is performed by a custom-written C/C++ program running on Macintosh G3 (DAQ computer) under MacOS 9.1. The same program is running the data acquisition. The functions of DAQ code include storing the digitized PMT waveforms, recording the time information of each waveform and also recording the counting rates of several counters.

As described in Section 2.6, there are two PMTs that detect bursts of photons originating in the cell. The photons arriving at the PMT's photocathode result in a current pulse on its anode. The typical width of the anode pulse corresponding to a single photoelectron at the photocathode[1] is 20 ns. The charge at the anode is roughly proportional to the number of photons that arrive at the photocathode. In our experiment, PMT anode pulses are digitized and recorded, which allows us to perform a detailed data post-analysis. Initially, the digitization was performed by the two Signatec PDA500 waveform digitizing cards installed in the PCI extension chassis of the DAQ computer. Later, an additional scheme utilizing the KamFEE[2] board was implemented. A separate Linux PC with VME interface card[3] was used to communicate with the KamFEE board via optical link.

---

[1] Single 430 nm photon arriving at the photocathode of Burle 8854 tube knocks out an electron with probability of about 18 %. This probability is called quantum efficiency.

[2] KamFEE is a KamLand Front End Electronics board designed by LBL for the KamLand experiment.

[3] SBS 618-3 PCI to VME adapter.

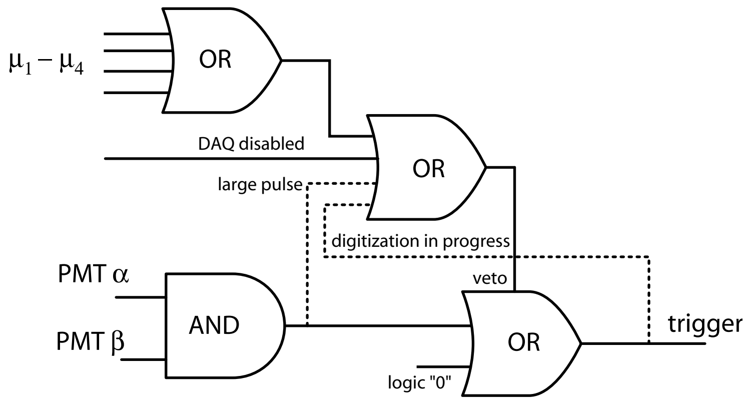

Figure 3.1: Logic schematics of the trigger circuit.

The digitization of PMT pulses occurs when the trigger signal is produced. The trigger signal is generated by a trigger logic schematically shown in Figure 3.1. According to this scheme, a coincidence between the pulses from two cell photomultipliers (denoted PMT α and PMT β) produces a trigger signal unless a) there is a simultaneous pulse on the muon detector, or b) DAQ is disabled, for example during the data transfer, or c) the "large pulse" has previously occurred and the system is still inhibited from accepting new triggers, or d) the system has not finished processing the previous trigger event. We will discuss each of these conditions as well as the signal timing characteristics in more details later in this section. Each trigger is assigned a time stamp with 1 ms resolution.

A more detailed diagram of the trigger circuit is presented in Figure 3.2. Physically all the modules are located in two NIM crates, about 5 m away from the PMTs. The $x : y$ labels near the signal lines convey the timing information of the signals, where x is the time delay (in nanoseconds) with respect to the leading edge of the PMT pulse, y is the width (also in nanoseconds) of the pulse. All pulses are NIM unless

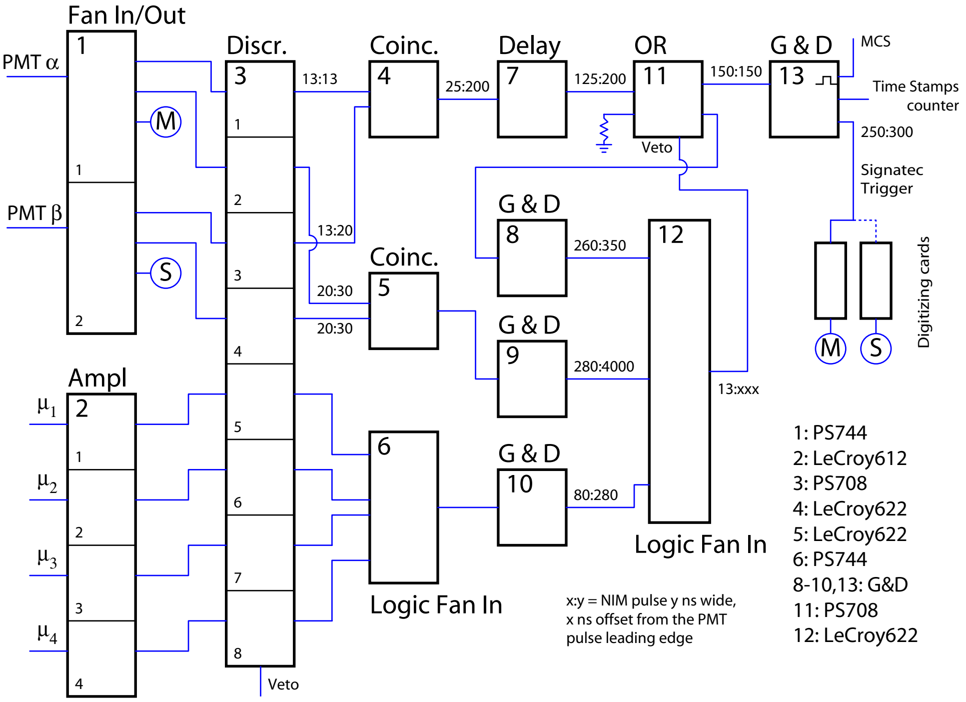

Figure 3.2: Logic schematics of the trigger circuit.

specified otherwise.

The anode signals from the two cell PMTs are buffered by the Fan In/Out module 1 before reaching the Discriminator 3. The thresholds of discriminator channels 1 and 3 are set to −28.3 mV and −30.8 mV respectively[4], corresponding to a position between the noise and single photoelectron peak of the photomultiplier[5]. A coincidence between the outputs of channels 1 and 3 of the Discriminator 3 produces a pulse on the output of the Coincidence module 4, that, after passing through a Delay line 7 made of roughly 20 m long RG-174/U cable, reaches the "OR" module 11. A second

---

[4] PMT anode pulses have negative polarity.

[5] The thresholds of the discriminators are chosen to give the same rates of the discriminator output pulses as observed in the integral of the pulse-height spectrum starting in the valley between the noise and the single photoelectron peak. The pulse-height spectrum is obtained by the Multi-Channel Analyzer.

input of the module 11 is terminated through a 50 Ω resistor and thus is equivalent to a logical "0". In this configuration, if no Veto signal for module Module 11 is set, a signal from the Delay line 7 produces a signal on the output of the Module 11, that, after passing through Gate and Delay (G&D) Module 13, generates a trigger pulse for the digitizing cards, a gate pulse for the time stamp counter and a pulse for the Multi-Channel Scaler used for concurrent monitoring on the trigger rates. A Veto signal for module 11 is produced by the Logic Fan In/Out module 12 whenever signal appears on the output of one or several of the G&D modules 8,9,10.

A signal is produced by G&D module 8 after each trigger event. It inhibits digitizing cards triggers while the digitization process is in progress[6].

A circuit that inhibits triggers for 4 μs after very large PMT pulses (amplitude of more than 1 V) consists of the channels 2 and 4 of Discriminator 3, Coincidence module 5 and G&D module 9. It was observed that such large PMT pulses are accompanied by a large number of afterpulses for a period of several microseconds. Without using this circuit, an intense afterpulsing is likely to cause an accidental coincidence on the output of module 4 and produce an additional trigger event associated with the original pulse. Note that digitization of the original large PMT pulses is still performed and pulse waveforms may be analyzed later, but such events will most likely be rejected as a candidate for a neutron decay event because of the amplitude of the pulse. The dead time introduced by the trigger inhibit for 4 μs after the arrival of a large pulse is quite small, since the rate of large pulses is typically less than 1 Hz.

Signals from the PMTs of the muon detectors μ_1–μ_4 are amplified by a factor of

---

[6] It was observed that if the length of the inhibit trigger is reduced from 350 ns to 300 ns, one of the cards starts missing the triggers which causes problems with the analysis of the data.

10 by the Amplifier 2 and then go to channels 5–8 of the Discriminator 3. The logical "OR" of the discriminator outputs, produced by the Module 6, is directed to the G&D module 10 that results in a Veto signal for Module 11 in case there is a muon pulse. The thresholds of channels 5–8 of the discriminator are chosen to maximize the coincidence rate between the cell PMTs and the muon detectors. Although the muon detector counting rate, roughly 2 kHz, significantly exceeds the expected muon flux (75 Hz for the horizontal muon detector with an area of 0.45 m^2 [8]), the dead time resulting from the false vetoing is about 0.1 %.

A Veto signal may be supplied to the Discriminator 3 by the DAQ computer to inhibit any triggers. This happens during the loading of the trap and during the data transfer between the memory of the digitizing cards and computer RAM. The inhibit signal is necessary to ensure a stable performance of the digitizing cards and correct time stamping of the trigger events.

As can be seen in Figure 3.2, there is a 250 ns delay between the trigger signal on the digitizing cards and the signal itself (M and S outputs of the Fan In/Out 1). The digitization of pulses in this situation is made possible by the pre-triggering mode of the digitizing cards. The digitization is performed continuously by 8bit ADC, with a selectable rate of 250 or 500 Msamples per second. The digitized samples are stored in a circular buffer of the card. When trigger arrives, part of the digitized waveform is extracted from the buffer and recorded into the onboard memory. Once the onboard memory is filled, DAQ computer transfers data into its RAM, clears the buffers and starts a new acquisition cycle.

Originally two Signatec digitizing cards operated in Master/Slave configuration, where the Master card provides clock and trigger signals to the Slave card. Nevertheless, problems encountered with operation of the Slave card (described in Section 3.2) made us switch to two-Master configuration[7], where each card is triggered independently by splitting a "Signatec Trigger" signal produced by G&D module 13. Even in two-master configuration we kept the old Master/Slave nomenclature for identification purposes.

The 24-bit counter on the Multifunction DAQ card[8] installed in one of the PCI slots of the DAQ computer is used to assign a time stamp to each trigger event. A square waveform with frequency of 1 kHz is supplied by the function generator[9] to the clock input of the counter. A "Time Stamps Counter" signal generated by G&D module 13 is connected to the gate input of the counter. When trigger arrives, the current value of the counter is stored in one of the registers of the card, while counter continues to count clock pulses. At the same time, interrupt request is set to inform the DAQ computer about the arrival of a new trigger event. Responding to the interrupt request, the DAQ computer reads the value of the register. If the next trigger event occurs while the previous interrupt request has not been cleared, the error flag is set and recorded with the next event. The specified accuracy of the clock signal is 5 ppm.

Digital input/output line of the same Multifunction DAQ card are used to control the NG6-U neutron beam shutter, slider, PMT power supplies and also to produce Veto signal for the Discriminator 3.

---

[7] A second master card, on loan from HMI, was graciously provided by R. Golub.

[8] National Instruments PCI-6025E.

[9] Stanford research Systems DS345.

A GPIB interface[10] is used for controlling and monitoring the superconducting magnet power supply.

A NaI gamma detector was installed in the vicinity of the PMTs α and β in order to monitor the external gamma background, as shown in Figure 2.3. A signal from the detector passes to the charge preamplifier, shaping amplifier and into the single channel analyzer (SCA). NIM output pulse of the SCA is converted to TTL by the level adapter module to be compatible with the counter input requirements.

A counter/timer card[11] provides 8 32-bit multi-purpose counters. The counters are used to track the muon detector rates (the output of Fan In module 6), the NaI detector counting rate and the counting rate of channels 1 and 3 of the Discriminator 3. The values of the counters are read roughly once every 5 seconds.

Concerns over the reliability of the Signatec cards (see Section 3.2) made us look for an alternative way to digitize PMT pulses. This task is fulfilled by using KamFEE boards that are designed for PMT waveform digitization and timing for the KamLand experiment [96]. One of the boards, on loan from LBL, was used in our experiment for similar purposes.

The addition of the KamFEE boards required the modifications of electronics hardware shown in Figure 3.3. The trigger signal for the KamFEE card is produced the same way as it is done for the Signatec cards. Due to a time delay between the arrival of the trigger pulse and the PMT pulses that need to be digitized, the pulses from the output of Fan In/Out module 1 are delayed by the Module 14 before reaching the Fan In/Out module 16 acting as a gate. As described below, this module

---

[10] National Instrumets PCI-GPIB.

[11] Measurement Computing PCI-DIO-48H/CTR16.

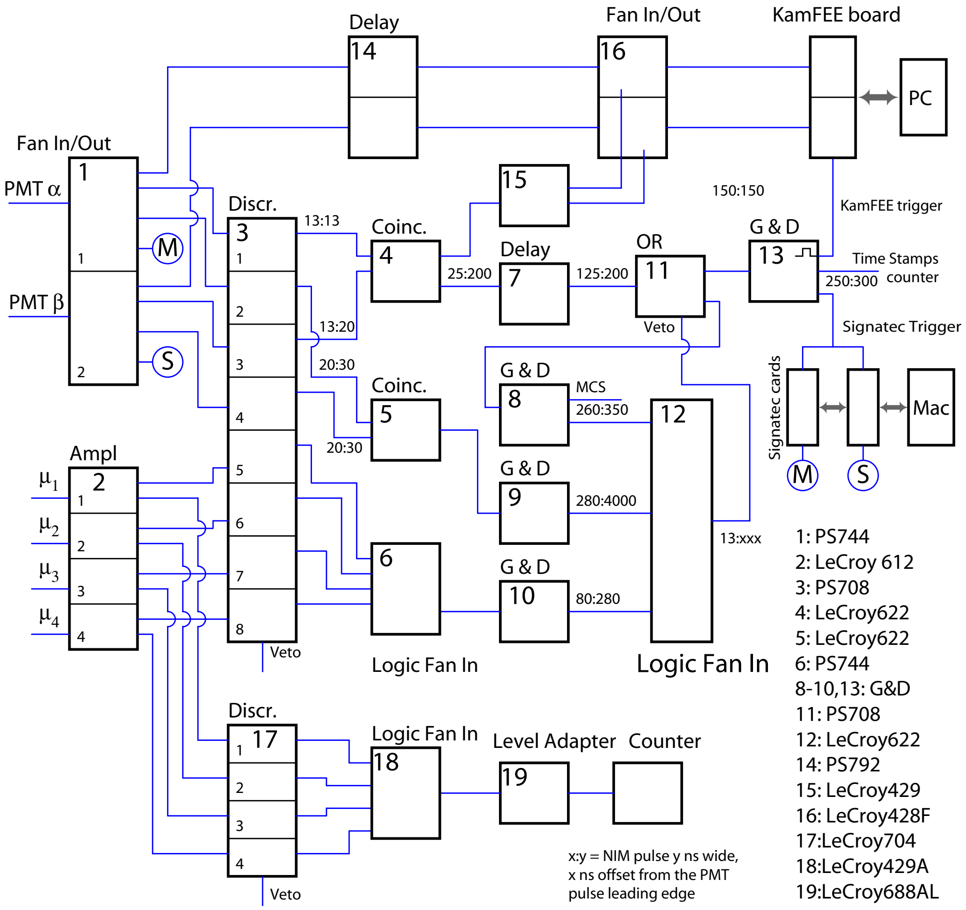

Figure 3.3: Logic schematics of the trigger circuit.

is present in order to decrease the dead time of the KamFEE card.

The KamFEE board has 12 independent input channels, but we use only channels 0 (PMT α) and 1 (PMT β). If the amplitude of the input signal exceeds the threshold level of the on-board discriminator then the waveform is stored in one of the two Analog Transient Waveform Digitizers (ATWD). The thresholds of the on-board discriminators in our setup are set below (smaller absolute value) the threshold of the Discriminator 3, so that the signal that is passed to the KamFEE board by the Fan In/Out module 16 (see diagram in Figure 3.3) will produce a trigger. The acquired waveform is digitized by a 10bit ADC upon the arrival of a trigger signal produced by a circuit shown in Figure 3.3 and discussed below. If no trigger signal arrives within 200 ns after the acquisition of the waveform, ATWD is cleared and re-armed within 1 μs. If trigger arrives, a high gain ($\times 20$) digitization is tried. If the amplitude of the pulse is out of the range, medium ($\times 4$) or low ($\times 0.5$) gain digitizations are attempted, giving the board a wide dynamic range. Each waveform contains 128 samples with an interval between samples of 1.5 ns. It takes about 30 μs to acquire and digitize the waveform. A design with two ATWDs minimizes the dead time of the channels, since acquisition in one ATWD may occur while the digitization on the other ATWD takes place. Still, since a single photoelectron rate in our setup varies in time and may exceed 100 kHz, a time-dependent dead time on the order of several percent may arise. Gating a signal with Module 16 decreases the dead time to less than 0.05 %.

In addition to digitizing the waveforms, KamFEE board performs time tagging of the events using a signal from a 40 MHz clock board installed in the same VME crate. The timing resolution of the KamFEE cards is 25 ns.

The threshold levels of Discriminator 17 are set to give a count rate on the outputs of discriminator roughly equal to the expected muon rates. The output of the logic Fan In module 18, after the conversion from NIM to TTL by the Level Adapter 19, is directed to the DAQ counter.

The voltages on the PMTs α and β ($V_\alpha = +2035$ V, $V_\beta = +2070$ V) can be controlled by the DAQ computer. Due to the intense luminescence in the cell when the neutron beam is open, the voltage on the PMTs is switched off during the loading of the trap. The voltage on the muon detectors is kept constant at $V_\mu = -2400$ V.

3.2 Signatec Cards Data Analysis

The recorded Signatec cards data is divided into blocks. The number of waveforms in each block, typically about 29000, is limited by the size of the 4 MB on-board memory of the card. Once this memory is filled, the DAQ control program issues a command to transfer the 4 MB block of data from the digitizing cards into RAM and then resets the cards. At the same time, in addition to master and slave card data, trigger timestamp and the counter information is saved in separate blocks by the DAQ computer. At the end of the run all data blocks are transferred to the hard disk for post-analysis.

Ideally, one expects an equal number of events in maser, slave and time stamp blocks. In reality, the time between two consecutive triggers may be shorter than the time it takes for DAQ computer to process one time stamp and thus a request to assign a time stamp for the second trigger will not be fulfilled. To ameliorate this situation, if the trigger timestamping is requested while the previous trigger processing is not completed, an "error" flag is set and recorded along with the time stamp information of the next trigger. In the data analysis, "extra" digitizing card triggers may be matched to those triggers that have error flag. For the average trigger rates of about 200 Hz about 1 % of the timestamps have the error flag. In some circumstances it is possible that more than one timestamping request comes during the processing time of the previous timestamp. In this case the number of digitizing card triggers in a block will be larger than the sum of the number of time stamps and the time stamps with error flags (this difference is usually about 0.1 % of the total number of triggers). The additional triggers are then distributed randomly between the trigger events that had an error flag set. Thus, each waveform acquired by the digitizing cards gets a time stamp assigned.

In rare cases the number of waveforms acquired by master card differs from that of the slave card. It may be due to trigger signal "missed" by one of the cards. Although the difference is usually very small, on the order of 10^{-5} of the total number of triggers, the files that exhibit such problem are excluded from the analysis since there is no one-to-one correspondence between the waveforms which makes it impossible to determine which waveforms correspond to the same trigger event.

The analysis of digitized waveforms is done block by block. First, the average pulse is calculated. Let n be the number of samples in each frame, N – the number of frames in each block, y_i – a sequence of digitized voltages within each block ($0 \leq y_i \leq 255$, $i = \{0, nN - 1\}$). Typical values of n and N are $n = 128$, $N = 29000$. Then the average pulse for the block is

$$y_j^{av} = \frac{1}{N} \sum_{k=0}^{N-1} y_{kn+j},$$

where $j = \{0, n - 1\}$.

One may expect to have some "roughness" in y_i due to electronics noise and digitization process itself. If this noise is random, its amplitude should be significantly reduced in the average pulse. This is not what is observed, suggesting that the noise comes from the interference of the components of the digitizing card with each other or with the other hardware. To simplify the pulse analysis, the noise was removed from the data by shifting odd or even channels by one point as shown in Figure 3.4. As we can see, this procedure does a decent job for the Master card and works a little less perfect for the Slave card, but still reduces the noise amplitude.

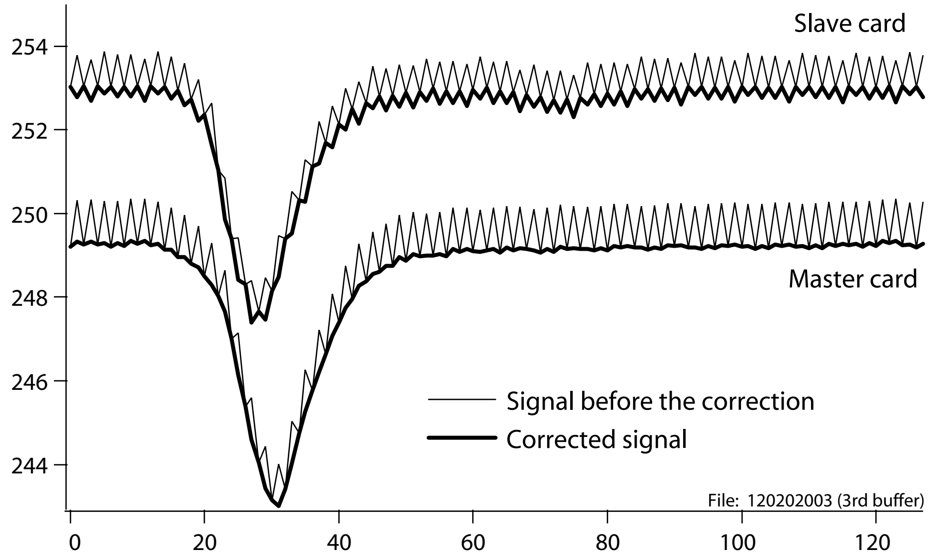

Figure 3.4: Average pulse obtained by the Master and Slave Signatec cards before and after smoothing correction.

The earlier Signatec data exhibit some other unexpected and troubling behavior illustrated in Figure 3.5. A square 35 ns wide pulse from a pulse generator was digitized by both cards in Master/Slave configuration operating at 250 Ms/s sampling rate. While master card produces the expected result, the waveform digitized by the slave cards is obviously incorrect. The problem was confirmed by the manufacturer and seems to be due to a combination of both hardware and firmware issues in the Slave card. A temporary solution consists in using 500 Ms/s sampling rate, where the problem does not disappear, but can be corrected in software. Figure 3.6 shows two different PMT pulses digitized by the Signatec cards. As in the pulse generator test, the Master card behaves as expected – the digitized pulse looks like a typical PMT pulse. The waveform of the Slave card though contains several one-sample spikes. It was noticed that the positions of these spikes are correlated, they are exactly 8

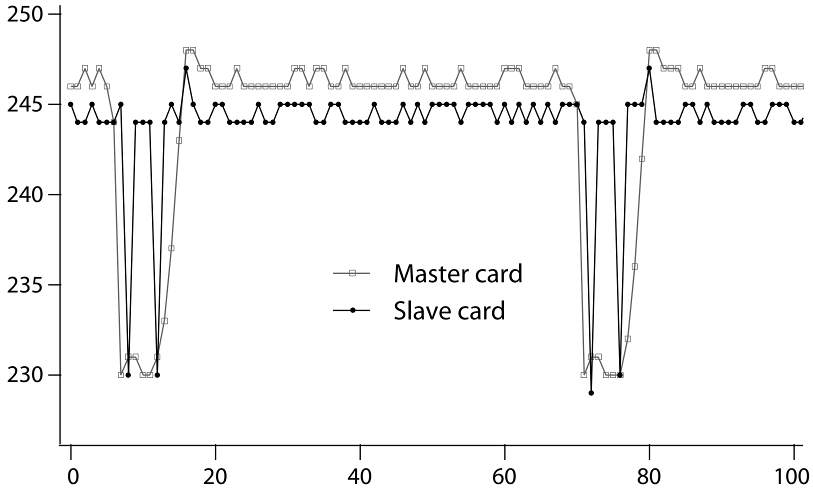

Figure 3.5: Square 35 ns wide pulse digitized by both Master and Slave cards operating in Master/Slave configuration at 250 Ms/s.

channels apart. Shift of every 8^{th} channel by 8 positions to the right with the offset determined by the positions of the spikes in the waveform makes waveform look “smoother”. The problem is further complicated by the fact that different buffers may require shifts with different offsets and sometimes more than one channel (the first buffer usually did not require any corrections). The good news was that the data shifts are consistent within each block. To correct for the byte shifting problem in software, we define “roughness” of the waveform as a sum of squares of the differences between adjacent samples of the average pulse

$$R = \sum_{i=1}^{n} (y_i^{av} - y_{i-1}^{av})^2.$$

There are $2^8 - 1 = 255$ possible combinations of 8 bytes that may require shifts. We find such a combination that minimizes the roughness R of the waveform after the shift. The two-master configuration described in Section 3.1 solved the byte shifting problem.

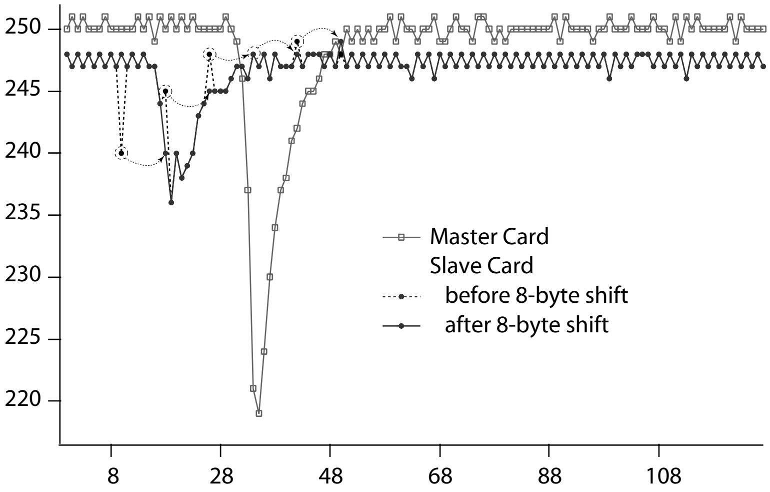

Figure 3.6: Waveforms digitized by a Slave card operating in Master/Slave configuration require corrections by shifting every 8th channel by 8 positions to the right.

The other problem with Signatec cards is their thermal overheating. To cool the cards, we had to use external household fan, but even then the concern of the temperature-dependent gain remained (see Section 4.7 for the gain shift tests).

After the corrections described above, the expected position of the main pulse (pulse that produced the trigger) is calculated for each block. It is done by finding a position of the minimum point in each frame of the block and then finding a median of their distribution.

For each waveform, the analysis program calculates the average of the last 16 channels of the waveform. The base level for the frame, b_k, is then obtained as a running average of the calculated 16-channel averages of the previous 500 frames in the block. This procedure adapts for the situations when the base level changes within a block, but implies that these changes occur gradually.

The next step is to identify PMT peaks in the waveform and calculate their areas.

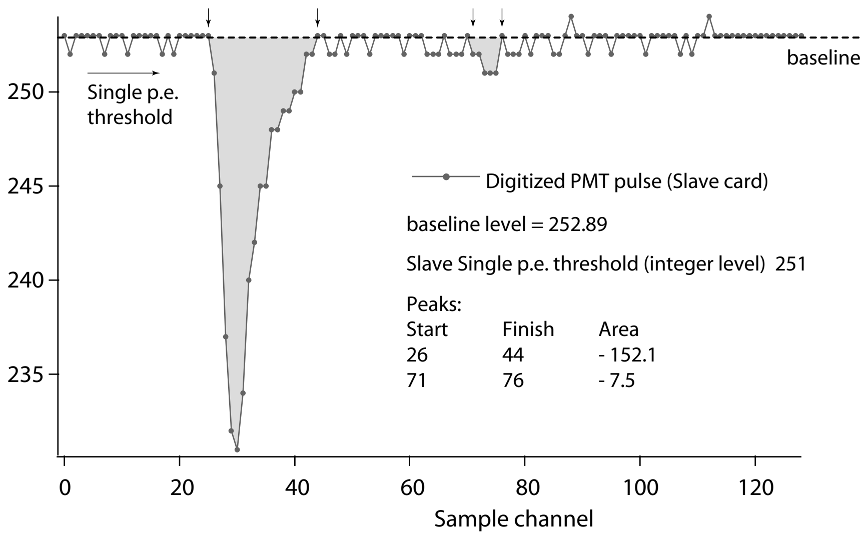

Figure 3.7: Peak identification in the waveform digitized by a Signatec PDA500 card.

The program starts at the beginning of the frame and progresses forward until the single photoelectron threshold level is reached, see Figure 3.7. A threshold level is a parameter that is set manually just below the baseline. If the threshold is set too low, there will be many frames with no pulses at all, if the threshold is too high, the number of pulses in a frame will be too large, since noise may be mistakenly identified as PMT pulses. Once the threshold is reached, the area of the peak is calculated as:

$$A = \sum_{i \in P} (y_i - b_k),$$

where P is a set of channels corresponding to a peak. The end of a peak is considered to be reached when three consecutive channels lay above the threshold level.

The main peak is identified based on the proximity to the expected position calculated from a block average pulse as described above. The area of the main pulse and all other pulses, time trigger information and the position of all peaks with respect to the main peak are stored in a separate file for making further cuts on the data.

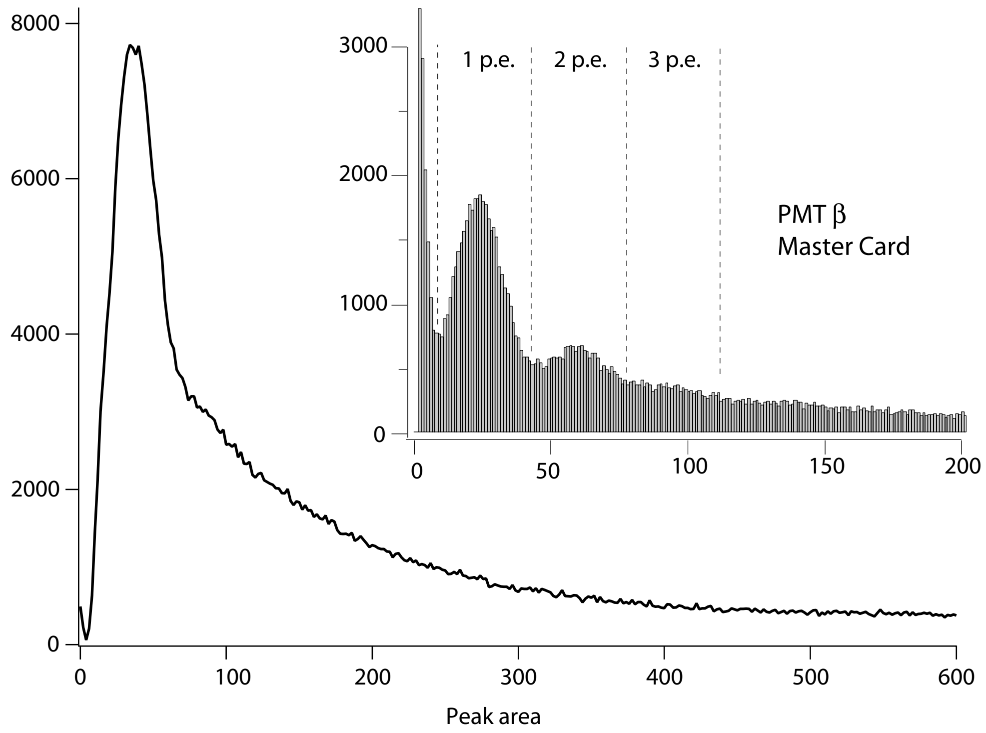

Figure 3.8: Pulse-height spectrum of the PMT β obtained by calculating areas of the pulses digitized by Signatec Master card. Inset: PMT pulse-height spectrum when the PMT is exposed to low intensity LED light.

The pulse-height spectrum of PMT β obtained by histogramming the peak areas calculated from the digitized waveforms is shown in Figure 3.8. The pulse "height" is the area of a main pulse reported by the analysis program. It is proportional to the total charge arriving at the anode of the PMT and thus should be proportional to the amplitude of the output pulse in a standard setup for measuring the pulse-height spectra consisting of a charge sensitive preamplifier and a shaping amplifier. A hint of a second peak in the graph near peak area of 80 is the two-photoelectron peak. The inset shows the pulse-height spectrum of the PMT illuminated by low-intensity bursts of photons produced by the LED. Both one and two photoelectron peaks are clearly resolved in this case.

The calibration of the detector, described in section 4.10, shows that on average we should expect 6 photoelectrons arriving at each cell PMT after the neutron decay. Thus we can introduce cuts on the data based on the area of the main peak of the event. Low-energy cuts, require certain minimum area of each digitized pulse and a minimum sum of two areas, discriminate against luminescence, activation and low-energy gamma backgrounds. High-energy cuts on the data, requiring area of the pulses to be less than certain value help to filter out some activation backgrounds and cosmic rays events that are not vetoed by the muon detectors.

The time stamps of the events that pass the cuts are binned in equal size bins for fitting and further analysis as discussed in Chapter 4. The typical bin width is 5 seconds, but 3 s and 10 s bins produce similar results. Although some information is lost during the binning process, the lifetime estimates produced by this method are very similar to the maximum likelihood estimates based on the exact time stamps of the events [97].

3.3 KamFEE Card Data Analysis

All digitized waveforms, their time tags and information about the input channel, ATWD channel and digitization gain used to acquire each form is stored in binary format.

The data analysis software is similar to that used for Signatec card analysis. One complication arises from the fact that the gains of different ATWD may be different and have to be corrected for.

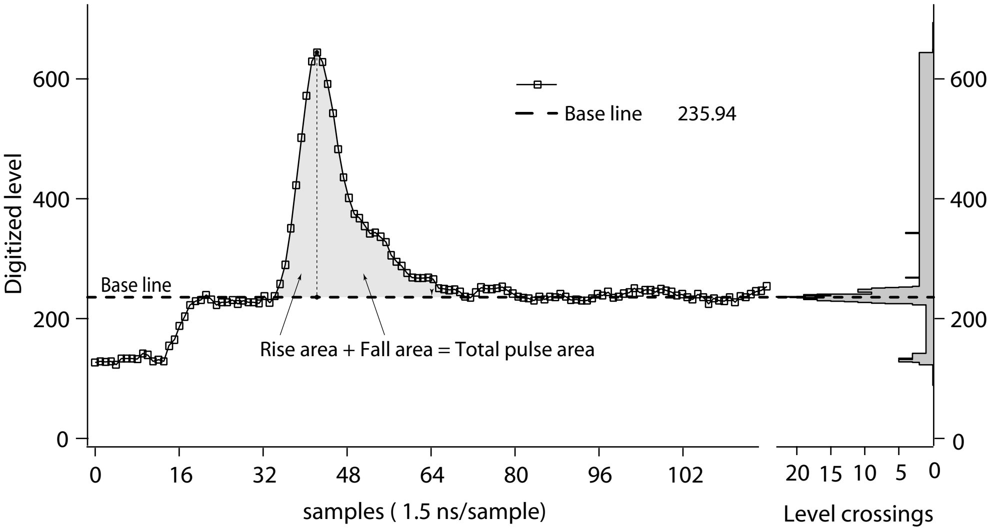

Figure 3.9: A typical pulse digitized by KAMFEE board. The base line is calculates based on the histogram of the number of times each level is crossed shown on the right.

A typical pulse digitized by the KamFEE board is shown in Figure 3.9. The base line of the pulse is determined for each frame separately from a histogram of the frequency of crossing of each of the 2^{10} levels as shown on the right in the same graph. The discontinuity in base line level near sampling point number 20 is due to the shift in DC offset of the module 16 (see Figure 3.3) used as a gate.

To determine the pulse position within a waveform, the analysis program scans looks for 5 or more consecutive points above the base line level. The first of these points is considered the beginning of the pulse. The end of the pulse is defined as a first sample below the baseline level. Once the beginning and the end of the peak are determined, the area of the peak can be calculated and stored for further analysis.

The threshold for software cuts on the KAMFEE card data is chosen by comparing the pulse-height spectra of the PMTs obtained during a calibration run (Section 2.6.2). The positions (in terms of area units) of the beta-peak in the spectrum for a fixed source position, similar to one shown in Figure 4.22, are calculated for pulses digitized by Signatec cards and by KAMFEE card. The ratio of the peak positions is then taken to be the ratio of the software cutting thresholds. The thresholds for the Signatec data are chosen based on the structure of the PMT pulse-height spectrum as discussed in Section 3.2.

In addition to the pulse area, one may consider other characteristics of the digitized pulses, as shown in Figure 3.9. Since KamFEE card uses the 10bit ADC converters and have three gain channel, and have high digitization rates shape analysis was performed only for the data taken with KamFEE cards.

Chapter 4

Results and Discussion

This chapter presents the experimental results. The data collection procedures and the experimental data sets are described in Section 4.1. The time structure of the backgrounds is discussed in Section 4.2. The results of the runs where the temperature of the cell is below 300 mK are presented in Section 4.3. The experimental evidence of neutron upscattering by phonons in the superfluid helium as the temperature of the helium increases is discussed in Section 4.4. The spectrum of the trapped neutrons is changed by ramping the magnetic field of the trap. Lowering the trap and then raising it helps to eliminate the above-threshold neutrons. Section 4.5 shows the results of the experiments with the magnet ramps.

The gain shifts of the detectors during the experimental run present a potential source of the systematic error in the measurements. The results of the experiments to measure the gain shifts and the data correction techniques used to compensate for the gain shifts are presented in Section 4.7. The data obtained by monitoring the external gamma background and its implications for the lifetime estimates is

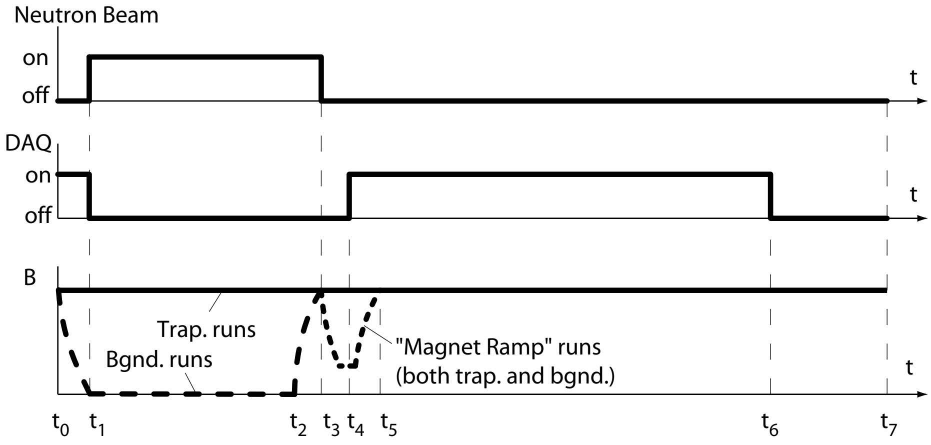

Figure 4.1: Schematic diagram of an individual run schedule. The trap is loaded during the time period t_1 to t_3. The Observation period occurs between times t_4 and t_6. Additional details are given in the text.

presented in Section 4.8. The experiments with the natural abundance helium in the experimental cell are a potent test of the background subtraction methods. Their results are discussed in Section 4.6. An alternative digitization scheme is implemented in order to check the DAQ operation. The results of these checks are presented in Section 4.9. The discussion of the detector calibration data concludes the chapter in Section 4.10.

4.1 Run Schedules and Data Sets

The data is collected in a series of experimental runs. There are two types of runs: neutron trapping runs and background runs[1] The sequence of events during each experimental run is shown schematically in Figure 4.1. The run starts at time t_0 with the neutron beam blocked. In trapping runs, the current of the magnet is

---

[1] The rationale for using two kinds of runs is discussed in Section 4.2.

set to 160 A, creating a 1.1 T deep magnetic trapping field. In background runs, the current of the magnet is set to 5 A. The loading of the neutrons into the trap begins at time t_1: the voltage on the PMTs is set to zero, the lead block "slider" (see Section 2.1.1) is removed from the path and the neutron beam shutter is opened. For background runs, the magnetic trap current starts raising from 5 A back to 160 A at time t_2. At time t_3, the neutron beam is blocked, the lead block slider is lowered into the beam path to reduce backgrounds and high voltage is supplied to the PMTs. In the "Magnet Ramp" runs, the current of the magnet begins decreasing from 160 A to 60 A. Observation of neutron decay events begins at time t_4, after the neutron beam is closed. The short delay between turning the beam off and the start of the data acquisition is necessary in order not to saturate the data acquisition (DAQ) system by fluorine[2] decays that occur in the first minute after the neutron beam is turned off. In the "Magnet Ramp" runs, once the current in the magnet reaches 60 A (this takes approximately 80 seconds), the magnet current is increased back to 160 A, reaching the final value by time t_5. Data acquisition is halted at time t_6 and the next run begins at time t_7.

Values for the parameters t_1 through t_7 are given in Table 4.1 for the four run schedules. The lengths of the loading period and the observation period of schedule "S" (Short) are chosen to minimize the variance in the neutron lifetime estimates [98, 99] for the observed background level (see Section 4.2) and the expected neutron signal. The Schedule "L" (Long) provides a longer observation time to help evaluate the value of the constant y in the 3-parameter exponential fit $A\exp(-t/\tau) + y$. The

---

[2] Fluorine is present in the neutron entrance windows and in the Gore-Tex cell. The half-life of ^{20}F is 11.0 s. The signal due to the fluorine decay is below the other backgrounds after approximately 80 s.

Table 4.1: Run schedules. Times are shown graphically in Figure 4.1 and are given in seconds. Details about the schedules are provided in the text.

Schedule	t_1	t_2	t_3	t_4	t_5	t_6	t_7
S	100	2150	2200	2270	—	4900	4900
L	100	2150	2200	2270	—	7600	7600
I	100	2150	2200	2270	—	4900	7600
MR	100	2150	2200	2270	2380	4900	4900

Table 4.2: A summary of the data sets.

Set Name	Runs	Schedule	Temperature, K	Comments
Cold1	358/358	S	< 0.30	Old and new bases
Cold2	136/136	L	< 0.30	Old and new bases
Cold3	112/112	I	< 0.30	Old bases
500mK	96/93	S	0.50	Old bases
700mK	79/82	S	0.70	Old bases
850mK	161/161	S	0.85	Old and new bases
MagnetRamp	148/125	MR	< 0.30	Old and new bases
He3	109/109	S	< 0.30	Old bases
He3Warm	33/33	S	≈ 1	Old bases

runs with schedule ''I" (Intermittent) are performed to understand some discrepancies that were observed initially between the data taken with schedules "S" and "L".

In order to compensate for possible time variations in the external backgrounds, the trapping and background runs are taken in an alternating manner: $TBBTBTTB$ and so forth. This sequence is chosen so that slowly changing linear and higher order polynomial drifts in the backgrounds are minimized. This technique, however, does not remove background variations that occur on a time scale of the duration of one run. In order to monitor and compensate for these changes in the external background — not so uncommon in the environment of the experimental hall — a NaI gamma detector is used (see Section 4.8).

A summary of the collected data sets is given in Table 4.2. The "Cold" runs are taken non-consequentially over the period of several months (01/03 until 06/03). The $T > 300$ mK runs, discussed in Section 4.4, are taken to study the temperature dependance of the phonon upscattering of neutrons in superfluid helium. In the "MagnetRamp" runs, performed in 11/02 and later, in 08/03, the magnetic field of the trap was lowered and then raised to test for the presence of above-threshold neutrons in the trap. These runs are discussed in Section 4.5.

In the "He3" and "He3Warm" runs, natural abundance, rather than isotopically purified, ^{4}He is condensed into the cell. The ^{3}He/^{4}He ratio of the natural helium is roughly 3×10^{-7}, that is high enough to absorb the trapped neutrons in less than a second. However, all processes that may produce backgrounds in the cell are not changed significantly. The absence of the neutron signal in the "He3" runs is the strongest indication that the background subtraction techniques discussed in Section 4.2 are indeed effective. The "He3" runs are discussed in Section 4.6.

4.2 Backgrounds

The exposure of the experimental cell to the cold neutron beam produces an intense light. A large fraction of this light is produced as a result of prompt neutron capture events. Some light, however, remains once the neutron beam is blocked. This long-term afterglow is attributed primarily to the neutron-induced luminescence and activation [90]. Light from these events and can be detected hours and even days after the neutron beam exposure. As discussed in Section 2.6.1, care is taken to choose materials that have minimal luminescence and activation. The counting rate of a single of PMTs as a function of time during one run is shown in Figure 4.2.

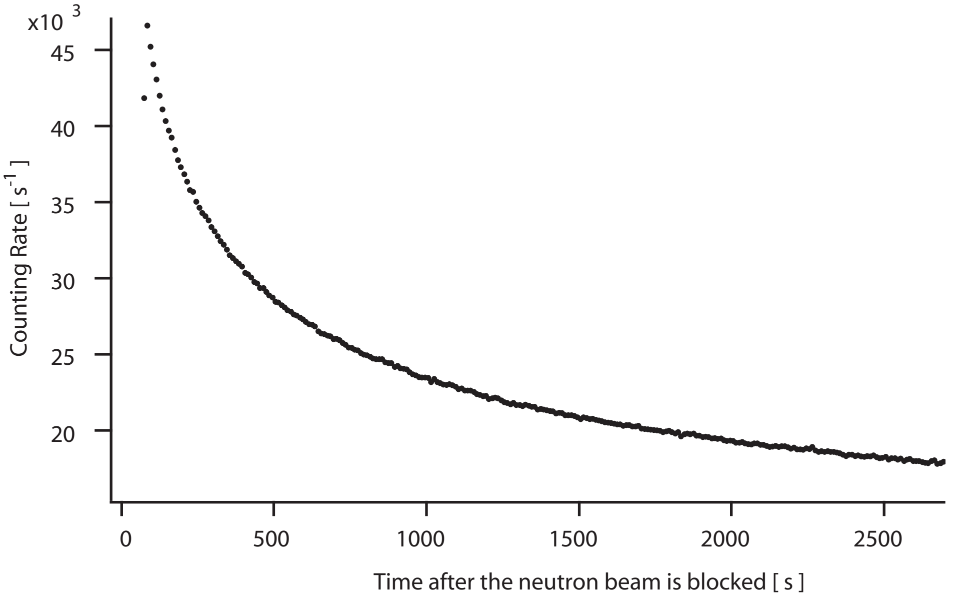

Figure 4.2: The counting rate of the PMT β during the (background) run. The threshold is set at one photoelectron level. The error bars are roughly the size of the markers. The start of data collection corresponds to time t_4 in Figure 4.1.

Although the neutron decays produce multiple photons within a short period of time ($<$ 10 ns) and the photons produced by neutron-induced luminescence are single photoelectron events, discrimination of neutron decays from luminescence using a single PMT is not practical due to the finite gain dispersion and the afterpulsing properties of the PMTs [54]. The afterpulsing is caused by the ionization of residual gas inside the PMT envelope: a single photon arriving at the photocathode may result in a large anode pulse. The probability of such an event is typically 10^{-3} to 10^{-4}. The two-PMT design implemented in our experiment, the light is split between the two PMTs and the coincident arrival of photons to each tube within a time window of 35 ns is required to trigger the data acquisition system.

The DAQ trigger rate as a function of time is shown in Figure 4.3. Due to the large

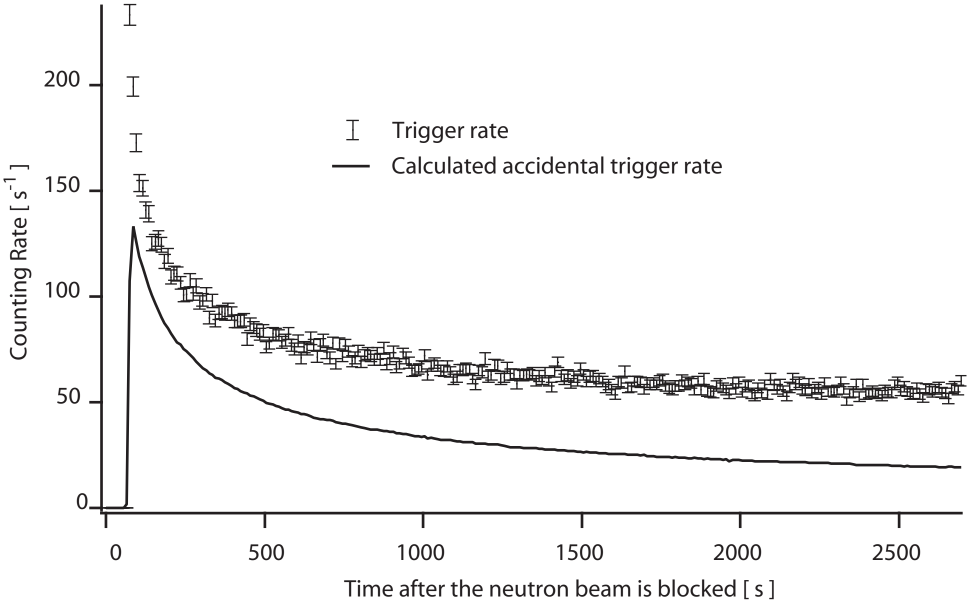

Figure 4.3: The DAQ trigger rate and the calculated accidental coincidence rate during the background run.

single photoelectron counting rate in each PMT, an accidental coincidence between PMTs (two uncorrelated photons arriving at the two tubes within a coincidence time window) is responsible for as much as half of all triggers. The reminder of the triggers arises from the events that produce multiple photons inside the cell or in the light guides.

The probability of an "accidental" trigger event becomes very small with increasing threshold level. The results of studies of the "spillover" effects, where a single photoelectron produced at the photocathode results in an anode pulse size corresponding to several photoelectrons [54], are shown in Figure 4.4. The probability that the accidental coincidence between two single photons will result in an event

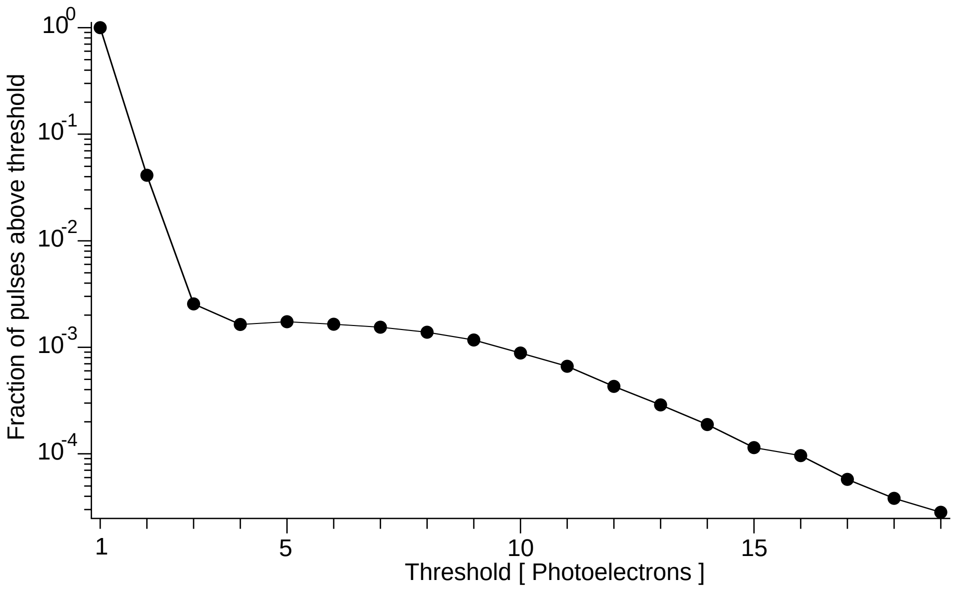

Figure 4.4: The fraction of single photoelectron events at the photocathode of the Burle 8850 PMT that result in an anode pulse that is equal to or larger than the threshold level [54].

that is above the 3+[3] threshold in each PMT is less than 10^{-5}.

The time histogram of the average of all background runs in the "Cold1" data set (new PMT bases only) for several threshold levels is shown in Figure 4.5. The signal can be thought of as having a constant component and a time-varying component. The results of fits of the data to a two-exponential model are shown in Table 4.3. The initial short lifetime exponential decay at the beginning of the run is due to the decays of ^{20}F and thus the decay lifetime is fixed to $\tau_F = 15.9$ s. The relatively high value of $\chi^2|_{\nu=519} = 1.28$ and the fact that the fit results depend on the fit range indicate that the model of the backgrounds is more complicated than the one used. The fits with more complicated models (3-exponents, 2-exponent plus $1/t$, etc.)

---

[3] The notation "n+" means that the size of the anode pulse corresponds to n or more photoelectrons at the photocathode.

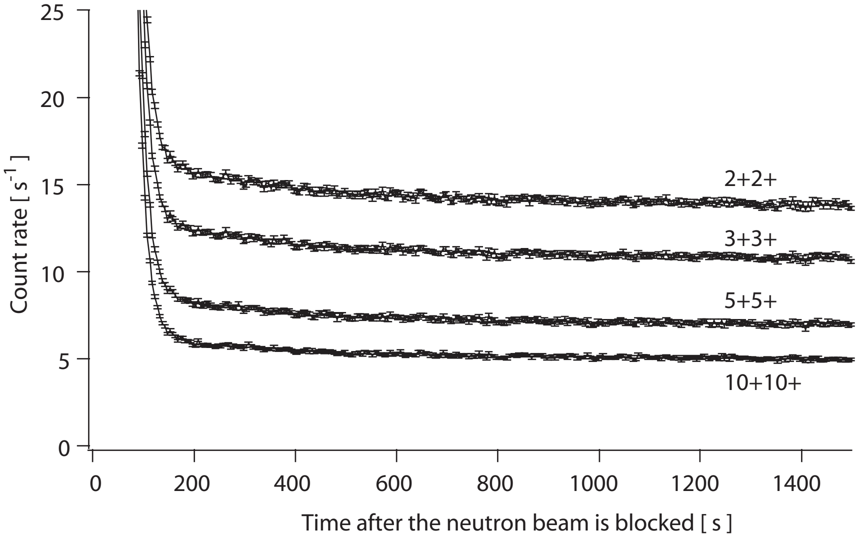

Figure 4.5: The average background run in the "Cold1" data set for different cutter thresholds. Only the first 1500 s of the run are shown.

provide a better match to the data, but the large number of free parameters and the strong correlation between them make it difficult to identify the exact source of the time-dependent backgrounds. We believe that it arises from the activation of several isotopes present as impurities in the materials composing the detection cell.

The primary sources of the constant backgrounds result from operation of the reactor: the background drops by a factor of 4.5 when the reactor is turned off (see Table 4.3). The reactor-off background is caused by decays of the naturally radioactive materials (mostly Uranium, Thorium and Potassium) in the apparatus and lead shielding that surrounds it. In addition, when the reactor is on and the liquid helium is removed from the cell, the background drops by a factor of two (3+3+ cut), indicating that roughly half of the constant backgrounds are produced outside of the helium in the acrylic light guides.

The magnitude of the backgrounds and their complicated nature require us to

Table 4.3: The results of the fits of the average of all background runs in the "Cold1" data set (176 runs, new bases only) to the function $y + A_1 \exp(-t/\tau_F) + A_2 \exp(-t/\tau_2)$. $\tau_F = 15.9$ s is the decay lifetime of ^{20}F. The data is binned in 5 s bins. The fit range is from $t = 75$ s to $t = 2685$ s. A typical χ^2 for the fits is 1.28. The last column shows the average counting rate of the detectors with the reactor off.

Cut level	y, s^{-1}	A_1, s^{-1}	A_2, s^{-1}	τ_2, s	Reactor off, s^{-1}
2+2+	13.70 ± 0.01	6637 ± 24	3.28 ± 0.06	389.1 ± 8.6	3.00 ± 0.03
3+3+	10.67 ± 0.01	6399 ± 23	2.79 ± 0.05	396.2 ± 9.1	2.28 ± 0.03
5+5+	6.91 ± 0.01	5882 ± 20	2.11 ± 0.04	408.5 ± 10.0	1.60 ± 0.03
10+10+	4.91 ± 0.01	5085 ± 18	1.58 ± 0.03	424.1 ± 11.5	0.98 ± 0.03

measure the backgrounds and subtract them from the trapping data. The average of all trapping and background runs and the difference between the two for the data set "Cold1" (new bases only) are shown in Figure 4.6. In the assumption that the backgrounds are identical in the trapping and background runs (see below), their difference is due to the decays of the trapped neutrons.

The difference between the trapping and background runs is that the magnetic field of the trap is off during the loading period in the background runs. Thus, no neutrons are magnetically trapped during the background runs. But this is not the only distinction. In our previous work [79], we observed that the magnetic field partially stabilizes the luminescence. In the background runs the magnetic field is lowered during the loading period and the luminescence is becomes higher. This leads to a higher luminescence intensity during the observation period of a trapping run. The requirement of coincidence between several photoelectrons in each PMT should however eliminate this luminescence component in the backgrounds. The magnetic field of the trap slightly focuses or defocuses the neutron beam in the trapping runs. Although the deflection is small, less than 1 mm for neutrons with a wavelength of 0.89 nm, the inhomogeneity in the impurity distribution in the material of the

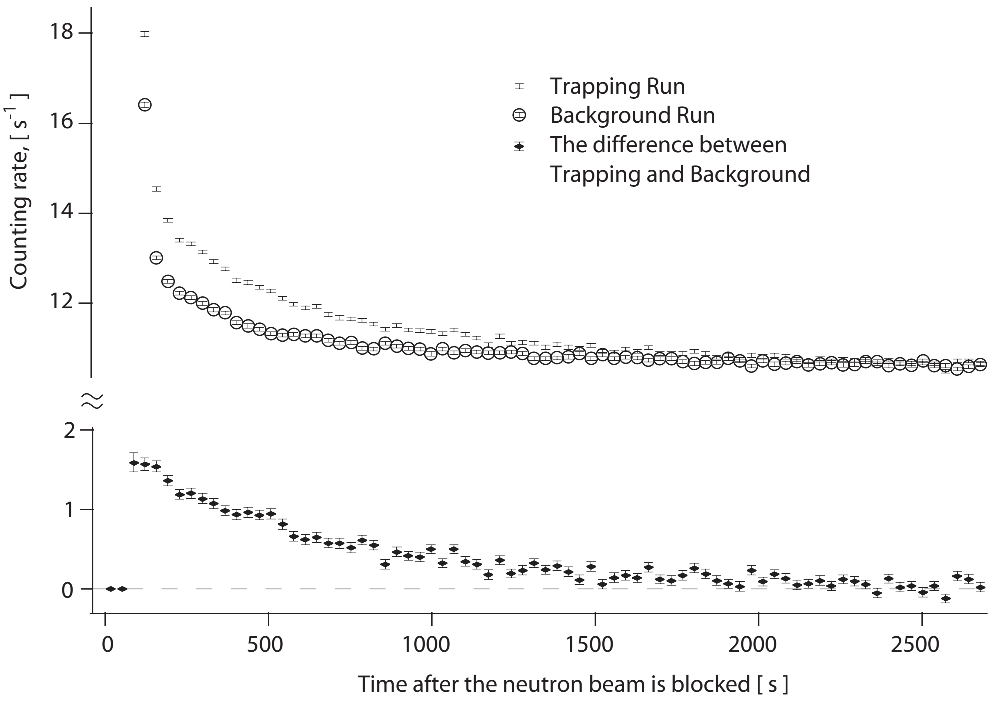

Figure 4.6: The average of the trapping and background runs of the "Cold1" data set (new bases only) and their difference. The bin width is 35 s. If the backgrounds are identical in the trapping and background runs, the difference is due to neutron decays in the trap.

neutron beam shields could conceivably create a difference in the materials activation in the trapping and background runs, thus leading to a non-zero difference. The most convincing test of the viability of the background subtraction technique is provided by the "He3" data set described in Section 4.6. Analysis of this data allows us to set an upper limit on any possible non-perfect compensation of the neutron-induced background. Finally, as described in Section 4.8, the external gamma ray background from neutron capture events in neighboring instruments could be different during the trapping and background runs due to the changing experimental activities at these instruments. If these changes ar uncorrelated with our run schedule, the background

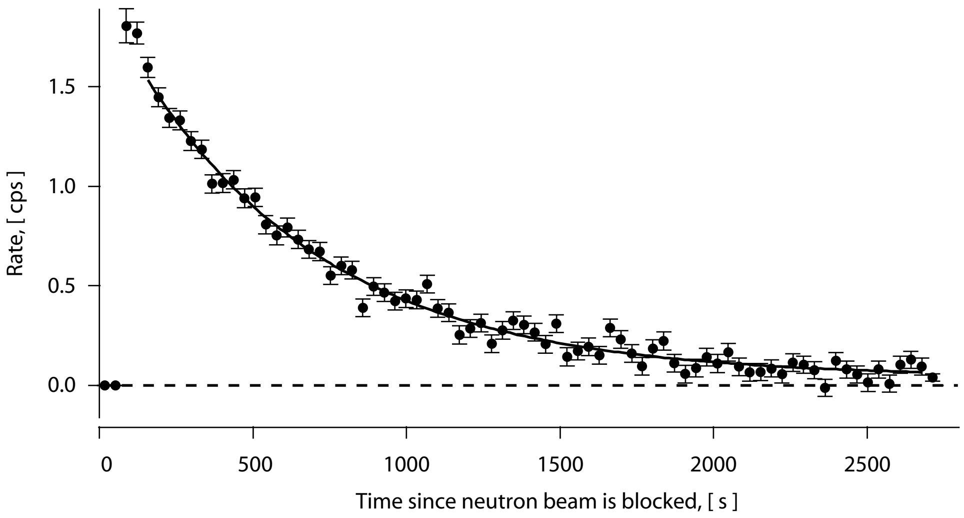

Figure 4.7: The difference between the average trapping and background runs in the "Cold1" data set. The threshold is set to require at least 3 photoelectrons in each PMT. The data is binned in 35 s wide bins.

differences should average out. We monitor the backgrounds during data collection to insure the conditions remain reasonably consistent.

4.3 300 mK Data

The data at 300 mK is taken using three different time schedules. The configuration of the detectors remained the same during all of the runs, but the voltage divider networks (bases) of the PMTs have been changed[4]. The data runs for each experimental condition are pooled together. The difference between the average trapping and background runs after the software threshold requiring at least 3 photoelectrons in each PMT (3+3+ cut) is shown in Figure 4.7.

Two models are used to fit the data: a 2-parameter exponential model, $A \exp(-t/\tau)$,

---

[4] This leads to somewhat different detection efficiencies, but this should not effect the lifetime estimates.

Table 4.4: The results of the fits of the deference between trapping and background runs for data taken at $T = 300$ mK. Fits are to $y + A\exp(-t/\tau)$, starting at $t_0 = 150$ s. The data is binned in 5 s bins.

Data Set	y, s^{-1}	A, s^{-1}	τ, s	χ^2
Cold1 (“S”) old bases	0.05 ± 0.02	2.03 ± 0.06	$627.8^{+33.8}_{-30.5}$	0.99
Cold1 (“S”) new bases	0.03 ± 0.02	1.79 ± 0.05	$623.6^{+34.6}_{-31.1}$	1.10
Cold1 (“S”) combined	0.04 ± 0.01	1.91 ± 0.04	$625.3^{+23.8}_{-22.1}$	1.02
Cold2 (“L”)	0.03 ± 0.01	1.96 ± 0.07	$586.1^{+25.8}_{-23.7}$	1.02
Cold3 (“I”)	0.03 ± 0.03	1.97 ± 0.06	$676.2^{+48.0}_{-42.0}$	0.98
All 300 mK data combined	0.04 ± 0.01	1.94 ± 0.03	$621.2^{+18.1}_{-17.1}$	0.96

and a 3-parameter model that includes a constant offset, $A\exp(-t/\tau) + y$. If the neutron signal is purely exponential and the backgrounds are identical in the trapping and background runs, the value of the parameter y in the 3-parameter model should be consistent with zero. However, in some data sets, this is not the case. Thus, using a 2-parameter model for these data sets is not justified. As shown in Section 5.1.2, a positive offset y may be an indication of the presence of above-threshold neutrons in the trap.

The results of the fits of the 300 mK data to a 3-parameter model are shown in Table 4.4. The “Cold2” runs have an observation period that extends from 2700 s to 5400 s. This provides more time to measure the constant offset y in the data; the longer run reduces the correlation between y and τ, thus reducing the error in the estimates of τ obtained in the 3-parameter fits. The schedule of data set “Cold3” has a digitizing card “cool-down” period of 2700 s after each run in order to test the effects of a different operating condition of the DAQ cards on the obtained results. The fit values for the trap lifetime τ obtained from each of the data sets taken at 300 mK agree within the statistical errors, and we can thus combine all of the data sets. The results of a fit to the combined data set are also shown in Table 4.4.

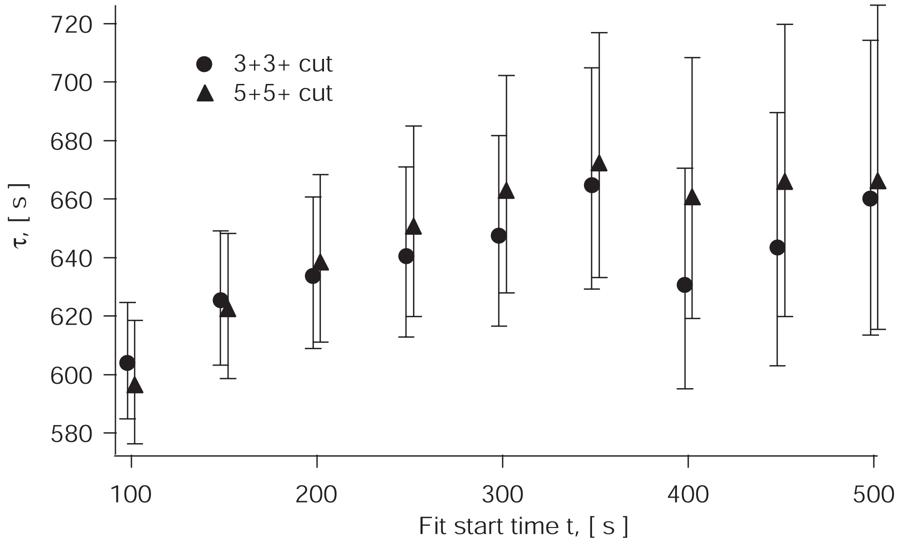

Figure 4.8: The dependance of the parameter τ in fits of the "Cold1" data set to the function $y + A\exp(-t/\tau)$. The fit range is $[t, 2680]$ s. The results of two different threshold cut levels are shown.

The sensitivity of the lifetime estimates on the fit range is shown in Figure 4.8. Although within the error bars, the values tend to become larger as fits start at a later time, that may be an indication of a non-single exponential character of the data. The higher cut produce similar results, but with increased error bars.

Monte-Carlo simulations [54] used to calculate the expected neutron production rate in the trap predict an initial decay rate of 6.7 s^{-1}. The detection efficiency of the cell for the 3+3+ threshold is roughly 48 % (see Section 4.10). Thus, the expected amplitude, A, of the neutron decay signal is 3.2 s^{-1}. If some neutrons leave the trap through mechanisms that do not produce light and thus not detected by the PMTs, the theoretical amplitude of the signal should be reduced by a factor of $\tau_{trap}/\tau_n \approx 1.4$. This predicts an initial decay rate of 2.3 s^{-1}, in rough agreement with the observed amplitude of 1.9 s^{-1}.

Table 4.5: The results of the fits of the deference between trapping and background runs at several helium bath temperatures. The values of the 2-parameter fits to $A\exp(-t/\tau)$ are used for those data sets that have value of y in a 3-parameter fit to $y + A\exp(-t/\tau)$ consistent with zero. The data is binned in 5 s bins. The range of the fit is $[150, 2680]$ seconds.

Data Set	y, s^{-1}	A, s^{-1}	τ, s	χ^2
300 mK	0.04 ± 0.01	1.94 ± 0.03	$621.2^{+18.1}_{-17.1}$	0.96
500 mK	fixed to 0	1.80 ± 0.07	$569.1^{+26.0}_{-23.9}$	1.03
700 mK	0.06 ± 0.02	1.65 ± 0.11	$437.4^{+42.8}_{-35.8}$	0.98
850 mK	fixed to 0	0.96 ± 0.09	$381.8^{+37.1}_{-31.0}$	0.96

4.4 Phonon Upscattering

As the temperature of the helium bath increases the probability of a neutron upscattering by excitations in the helium increases. To observe this effect, data was taken at helium bath temperatures of 500 mK, 700 mK and 850 mK. Results to the fits of the data are shown in Table 4.5.

The loss rate of the neutrons from the trap due to thermal upscattering should be negligibly small at 300 mK [58]. At this temperature, the total neutron loss rate may be expressed as $\tau_{0.3}^{-1} = \tau_n^{-1} + k_{loss}$, where τ_n is the neutron's lifetime and k_{loss} is the neutron loss rate due to mechanisms other than beta decay. At higher temperatures, the loss rate is $\tau_T^{-1} = \tau_n^{-1} + k_{loss} + \tau_{upsc}^{-1}$, where τ_{upsc} is the phonon upscattering lifetime in the helium.

Then, the value of τ_{upsc} can be calculated using

$$\tau_{upsc}^{-1} = \tau_T^{-1} - \tau_{0.3}^{-1}.$$

The values of τ_{upsc} extracted from the fits presented in Table 4.5 are shown in Figure 4.9. It should be noted that we use the error bars on τ without corrections for gain shifts, changes in the external background and possible non-perfect background

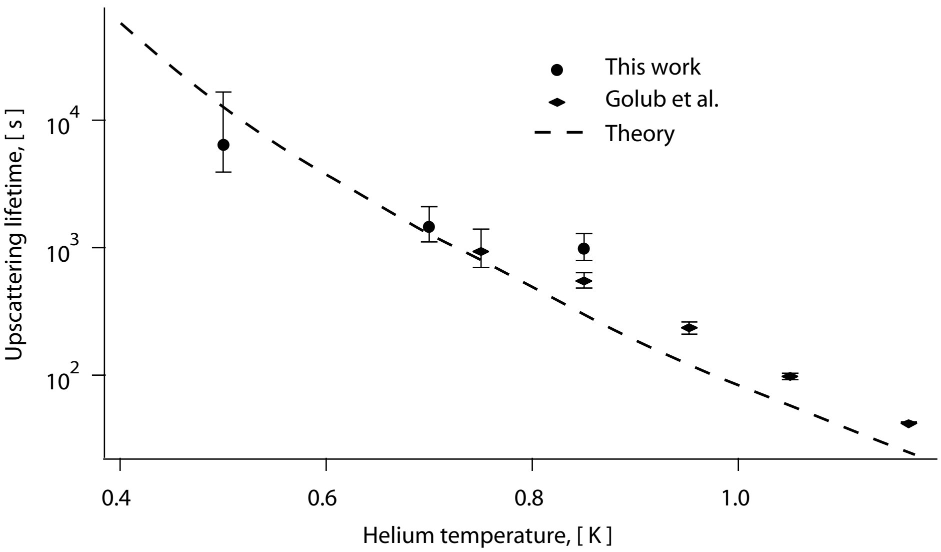

Figure 4.9: The temperature dependance of the neutron upscattering time in the helium. Also shown is the experimental data by Golub [59]. The total (including one and multiphonon events) upscattering theoretical curve [59, 58] is extrapolated as T^{-7} for $T < 0.6$ K.

subtraction. As shown in Sections 4.6, 4.7, and 4.8, these corrections give results consistent with the reported values of τ but with somewhat larger error bars.

Also shown in Figure 4.9 is the higher temperature data reported by Golub et al. [59] and the theoretical loss rate calculated in Refs. [58, 59] using Landau's Hamiltonian. Although the error bars on our lower temperature measurements are large, the data is in general agreement with theory. It is interesting to note that both our data and Golub's data suggest consistently higher values of the upscattering lifetime at higher temperatures where the roton scattering and one phonon absorbtion start playing a larger role [59].

4.5 Magnet Ramp Runs

Some neutrons with a kinetic energy larger than the magnetic trap depth can be confined in the trap for an extended period of time either magnetically, on special kinds of orbits, or materially, by the physical walls of the detector (see Sections 5.1.1 and 5.1.2). The loss of these neutrons reduce the measured trap lifetime and present a systematic error in the measurement.

As shown in Section 5.1.2, decreasing the magnetic field to roughly one third of its maximum value and then raising it back up, helps to remove the neutrons with energies higher than the trap depth (above-threshold neutrons). The magnetic field ramp also removes some of the neutrons with kinetic energy less than the trap depth, so the "purity" of the spectrum is achieved at a cost of the neutron population of the trap.

The schedule of the magnetic field runs is described in Section 4.1. The magnet ramp data is taken in two subsets. The early data ("MagnetRamp1") is taken in November of 2002. Neither the external background information from the gamma detector (Section 4.8) nor reliable information about the status of the neutron beam shutters of nearby instruments is available for these runs. The difference between positive and negative data has a negative offset, most likely due to different constant background conditions during the trapping and background runs. The fit results are shown in Table 4.6. A second subset is taken in August of 2003 and the external gamma background detector allowed us to monitor the changes in the backgrounds (see Section 4.8). The constant offset is consistent with zero in this data subset and we also quote the results of a 2-parameter fit to $A\exp(-t/\tau)$. The difference between

Table 4.6: The results of the fits of the difference between trapping and background runs in the "MagnetRamp" data. Fits are to $y + A\exp(-t/\tau)$, starting at $t_0 = 250$ s. The data is binned in 5 s bins.

Data Set	y, s^{-1}	A, s^{-1}	τ, s	χ^2
MagnetRamp1	-0.12 ± 0.06	0.99 ± 0.08	$920.4^{+286.8}_{-176.7}$	1.08
MagnetRamp2	-0.01 ± 0.05	0.96 ± 0.08	$851.8^{+214.2}_{-142.5}$	1.11
MagnetRamp2	fixed to 0	0.96 ± 0.07	$833.5^{+74.0}_{-62.8}$	1.11

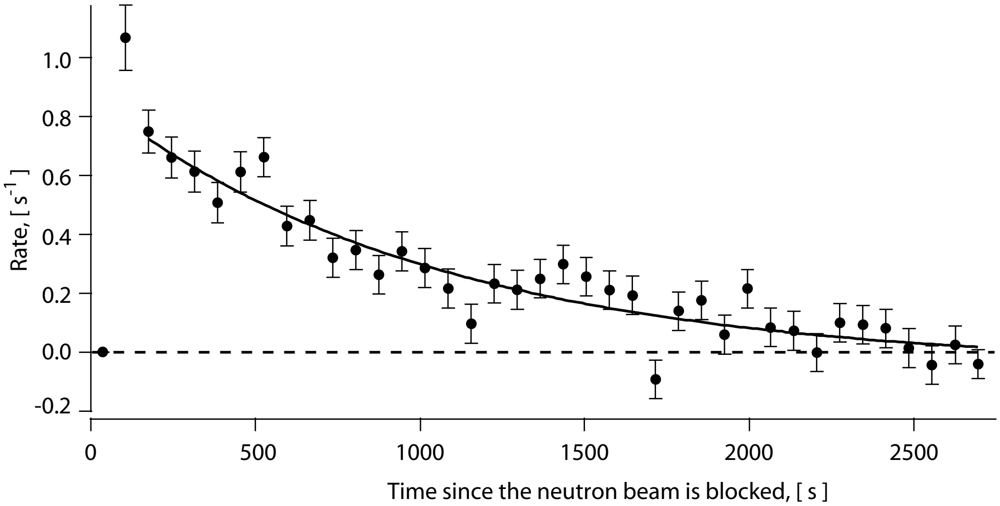

Figure 4.10: The difference between trapping and background runs in the "MagnetRamp2" data set. The solid curve is the 2-parameter fit to the data. At least 3 photoelectrons are required in each PMT. The data is binned in 70 s wide bins.

trapping and background runs for this data set is shown in Figure 4.10.

As can be seen from the fits, the trap lifetime is substantially longer than the trap lifetime in the fits shown in Table 4.4. The lifetime for these data sets is consistent with presently accepted value of the neutron lifetime of (885.7 ± 0.8) s. Although the statistics for these runs is not as good as in the 300 mK data set, the longer lifetime serves as an indication that ramping the magnetic field helps to eliminate the above-threshold neutrons from the trap. The reactor shutdown for maintenance in August of 2003 did not allow additional time for improving the statistics of the magnet ramp data.

These results suggest that magnet ramping will be necessary for future measurements using loading techniques similar to one presently used in our experiment. Elimination of materially trapped neutrons by ramping the magnetic field becomes more efficient as the trap depth increases (see Section 5.1.2).

4.6 Natural Abundance Helium Runs

In this set of runs, the isotopically pure ^{4}He is replaced with natural abundance helium having a ^{3}He/^{4}He ratio of order 3×10^{-7}. The presence of the ^{3}He nuclei in the cell leads to the capture of the magnetically or otherwise trapped neutrons in less than one second due to the large neutron absorption cross section on ^{3}He ($\sigma_{th} \approx 5333$ b). Thus, if any non-zero signal is observed in the difference between trapping and background runs, it should be due to an imperfect background subtraction. The small amount of ^{3}He does not change the luminescing properties of the materials in the cell and causes minimal change in the neutron flux that reaches the beam stop (less than 1 %). Since the cell is kept sealed during all runs, the placement of the materials inside the cell remains the same, and the luminescence and activation of the materials in the cell should be the same in the runs with the isotopically pure helium and the natural helium. The experimental data shows that the time-varying backgrounds in both the isotopically pure and natural abundance helium runs are the same within the statistical uncertainty of the measurements.

The intensity of one of the potential sources of the backgrounds, neutron-induced luminescence, depends on the cell temperature, the natural abundance runs are taken

Table 4.7: The results of the fits of the difference between trapping and background runs with natural abundance helium. Fits are to $y + A\exp(-t/\tau)$. The data is binned in 5 s bins. The range of the fit is $t = 200$ s to $t = 2680$ s.

Data Set	Pairs	y, s^{-1}	A, s^{-1}	τ, s	χ^2
300 mK	109	0.1 ± 0.9	-0.1 ± 0.9	-4420^{+3910}_{-5080}	1.08
1 K	33	0.1 ± 0.6	-0.1 ± 0.5	-2676^{+2860}_{-2520}	0.99
Combined	142	0.04 ± 0.06	0.08 ± 0.05	1134^{+2100}_{-780}	1.02
Combined	142	0 (fixed)	0.04 ± 0.06	395 (fixed)	1.03

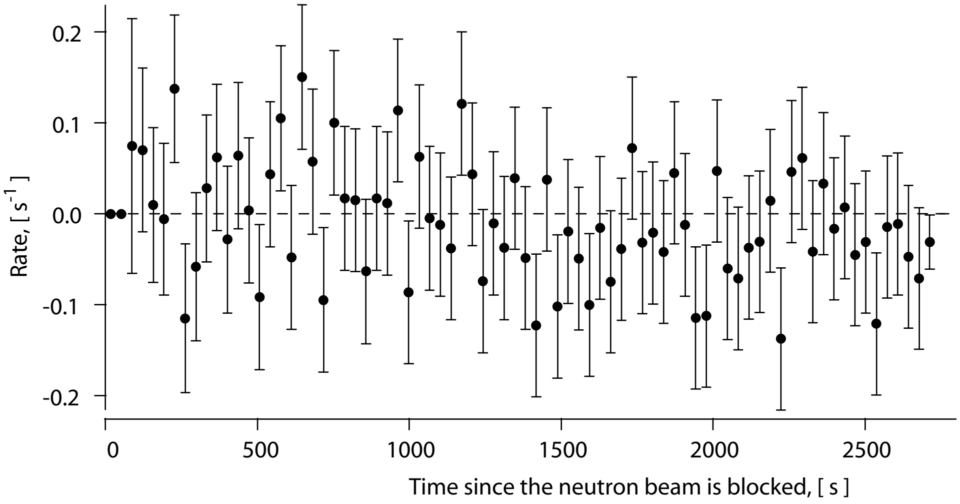

Figure 4.11: The difference between trapping and background runs when the cell is filled with natural abundance helium. The 300 mK and 1 K data sets are combined. At least 3 p.e. are required in each PMT.

at temperatures of 300 mK and 1 K. The results of the fits of the difference between "trapping" and background runs are shown in Table 4.7. All of the fits are consistent with zero. There is no evidence of luminescence in the data in either data set or when the two data sets are combined. The combined data set is shown in Figure 4.11.

To set an upper bound on any possible amplitude of the exponential signal that may be present in the difference data, the parameter y is set to zero and the value of τ is fixed to 395 s. The 395 s lifetime value is obtained by fitting the average background run[5]. If the background subtraction is not complete, we might expect a signal with the same time constant that appears in the difference data. The amplitude of the fit, $A = (0.04 \pm 0.06)$ s^{-1}, sets an upper boundary on the 395 s exponential signal in the isotopically pure helium data. One may estimate a possible shift and the uncertainty in the value of the trap lifetime that are introduced by this signal, but a more reasonable approach that does not depend on the specific model is to subtract the natural abundance helium data from the isotopically pure data. We expect the error bar on the fit to the trap lifetime to become larger, but this accounts for the variety of the models that can be used to fit the data shown in Figure 4.11.

The fit to the data obtained by the subtraction of the natural abundance helium data from the isotopically pure data (all data is taken at 300 mK) produces $((0.09 \pm 0.03) + (1.80 \pm 0.08) \exp(-t/(610^{+56}_{-47})))$ s^{-1}. The estimates of the lifetime are consistent with the reported values before the subtraction (see Table 4.4).

The difference between trapping and background runs for data sets taken at helium bath temperature of 300 mK without magnetic field ramping (Figure 4.7), with the ramping (Figure 4.10) and for the natural helium runs (Figure 4.11) are displayed on the same graph in Figure 4.12.

4.7 Gain Shifts

The knowledge of the overall detection efficiency is not required for measuring the neutron lifetime, although a change in the detection efficiency during the time of

---

[5] As mentioned in Section 4.2, a single exponential model is not sufficient to fully describe the backgrounds. However, the parameter τ of a single exponential fit gives a typical characteristic time constant of the time-varying background.

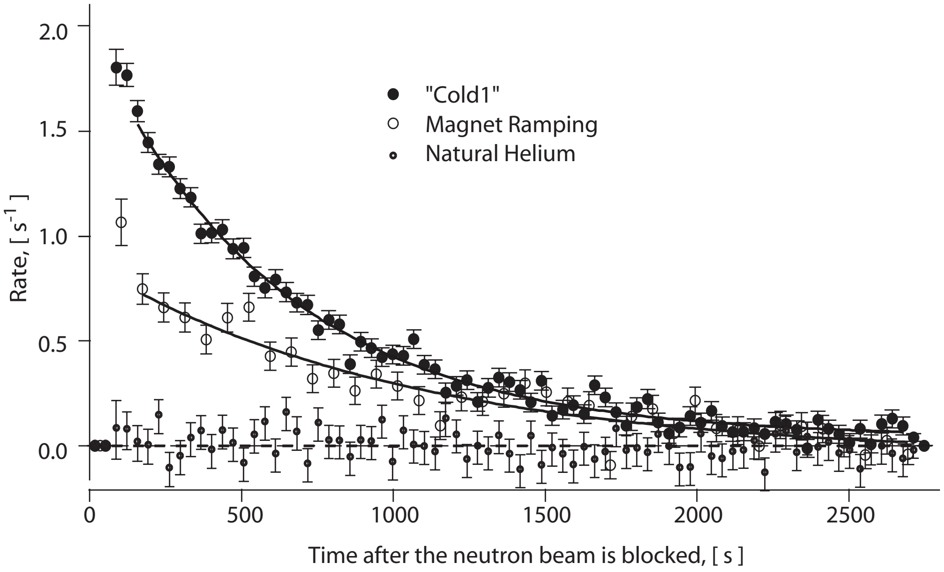

Figure 4.12: The difference between trapping and background runs for data sets taken at helium bath temperature of 300 mK without magnetic field ramping, with the ramping and for the natural helium runs. At least 3 p.e. are required in each PMT. Solid lines are the fits to $y + A\exp(-t/\tau)$. The fit parameters are given in text.

one run does introduce a systematic error. Several things may cause the detection efficiency to drift [88, 100] – the gain of the PMTs may change after their high voltage is switched off during the loading period of the run and then restored during the observation period; the PMT's photocathode performance may be affected by the intense light produced by the neutron beam inside the cell during the loading period; the gain of a PMT may depend on its counting rate; the gain of the digitizing cards may also change due to temperature drifts during the observation period.

In order to characterize the size of any gain shift in our setup, an optical fiber is brought radially into the aluminum can housing of the PMTs, near the light splitter (see Figure 2.31). A red LED is pulsed with a frequency of ≈ 200 Hz producing flashes of light with an amplitude equivalent to several tens of photoelectrons in each

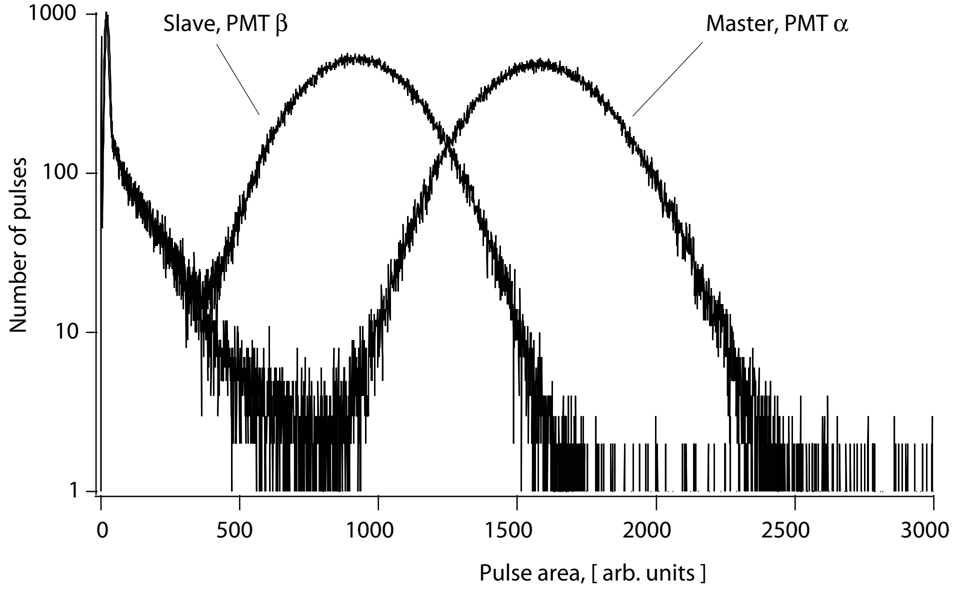

Figure 4.13: Pulse-height spectra of PMTs α and β with a pulsed LED light entering the PMT housing. The LED pulsing rate is $\approx$ 200 Hz.

PMT. The end of the fiber is roughened with sandpaper to make the light source more diffuse. A typical pulse-height spectrum for this configuration is shown in Figure 4.13. The LED peaks are clearly seen in the spectrum in the 500 to 2500 area units range. The difference in the positions of the peaks for two photomultipliers may be explained by the variation of quantum efficiencies between two PMTs and the asymmetry in the fiber entrance geometry.

To quantify the magnitude of any gain shifts, the observation period is divided into 100 s intervals. The position of the LED peak is calculated for each time interval by taking a weighted average of the part of the spectrum in the region of 750 and 2500 area units for PMT α and 350 to 1700 area units for PMT β. The relative position of the LED peak as a function of time since the neutron beam is blocked is shown in Figure 4.14. The gain is normalized to produce unity as an asymptotic value of

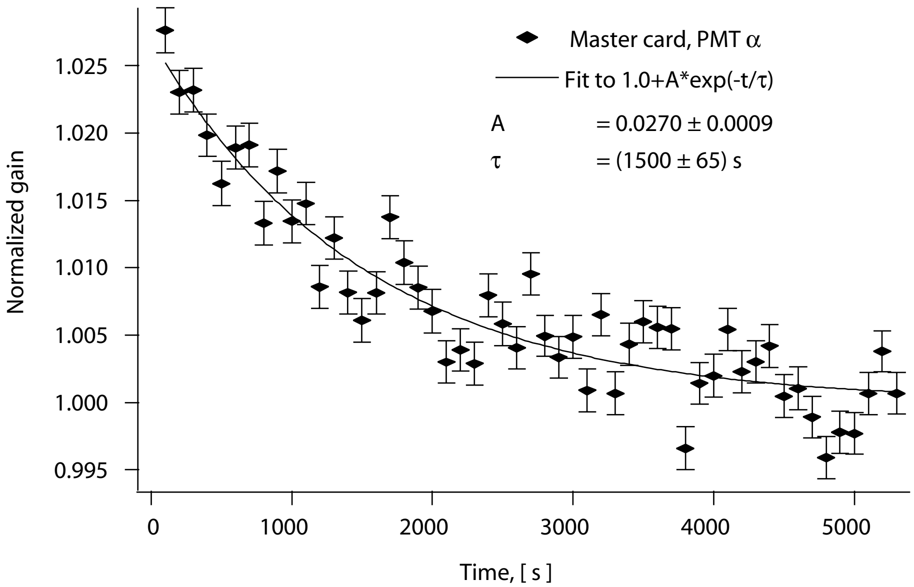

Figure 4.14: The normalized gain shift measured using LED light pulses in PMT α as a function of the time since the neutron beam is blocked from entering the cell. The gain shift is calculated from the shift of the position of the LED peak and is normalized to produce $y_0 = 1.0$ in a fit to $y_0 + A\exp(-t/\tau)$.

y_0 in a fit of the LED peak position to the function $y_0 + A\exp(-t/\tau)$. Although in principle, not only the LED light, but also the light from the other sources inside the cell and acrylic light guides may produce pulses that will be counted in estimating the position of the LED peak, the effect of these other sources is small due to the large number of photoelectrons in a typical LED pulse. The subtraction of the pulse-height spectrum of the run without the LED flashes from a run with the LED flashes (the neutron beam enters the cell in both cases) does not change the gain shift estimates.

When the LED runs are repeated with no neutrons entering the apparatus during the trap loading period but with all other conditions kept identical, gain shifts on the order of 1 % are observed only during the first 100 s after the PMT is biased, as shown in Figure 4.15. This suggests that the effect of the gain shifts is primarily due

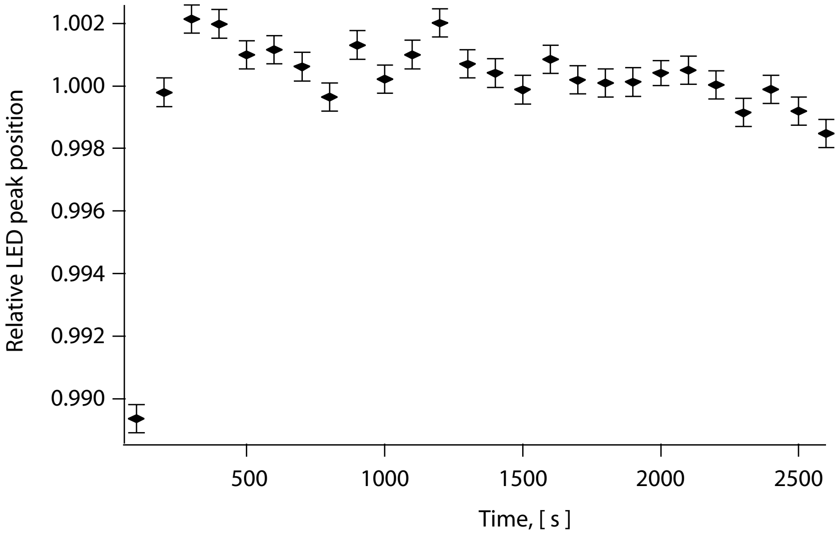

Figure 4.15: The normalized gain shift of the pulses in PMT α as a function of time since the neutron beam is blocked. No neutrons enter the apparatus during the trap loading period.

to photons produced in the cell during the neutron loading period.

In order to estimate the effect of the gain shifts shown in Figure 4.14 on the estimates of the lifetime in the neutron trapping data, we introduce a "floating", time-dependent cutting threshold (see Section 3.2) by using the empirical model of the gain shifts. If X_0 is a "hard" cutting threshold corresponding to the asymptotic value of the PMT gain, then the time-dependent threshold will be: $X(t) = X_0(1 + A\exp(-t/\tau))$, with the values of the parameters A and τ taken from the fit shown in Figure 4.14.

The results of the fits to the "Cold1" data set with and without gain shift corrections are shown in Table 4.8. As expected, the gain shift correction decreases the amplitude of the exponential fit and makes the trap lifetime longer. However, the difference in the fit parameters of the corrected and uncorrected data is less than the error on these parameters.

Table 4.8: The results of the fits of the deference between trapping and background runs for the "Cold1" (old bases only) data set with and without corrections for the detector gain shifts. Fits are to $y + A\exp(-t/\tau)$, starting at $t_0 = 150$ s. The data is binned in 5 s bins.

Data Set	y, s^{-1}	A, s^{-1}	τ, s	χ^2
No corrections	0.05 ± 0.02	2.03 ± 0.06	$627.8^{+33.8}_{-30.5}$	0.99
Gain shift corrected data	0.04 ± 0.02	2.01 ± 0.05	$635.7^{+34.5}_{-31.1}$	1.00

The gain correction will become more important when the statistics of the measurement improve after the new trap is built.

4.8 Ambient Gamma Background Monitoring

A NaI detector is placed next to the cell PMTs inside the lead "house" surrounding the apparatus to monitor changes in the ambient gamma background.

The pulse-height spectra taken both during the reactor shutdown period and while the reactor is in operation are shown in Figure 4.16. The calibration of the detector was performed using a ^{60}Co source that produces gammas with energies 1.17 MeV and 1.33 MeV. In addition, the detector is magnetically shielded, and we have verified in separate measurements that the magnetic field of the trap does not change the shape of the spectrum. As shown in Figure 4.16, the operation of the reactor increases the gamma background by a factor of 4 (with a low energy threshold of roughly 100 keV). If the beam shutter of the nearby (NG6 and NG6M) instruments are open, this creates an additional 20 % increase in the gamma background. The most pronounced feature of the spectrum is a 480 keV peak attributed to prompt gammas produced in neutron capture on ^{10}B. Boron is a common ingredient in the neutron shields. Since the apparatus lead shield thickness (10 cm) is sufficient to attenuate 0.48 MeV gammas

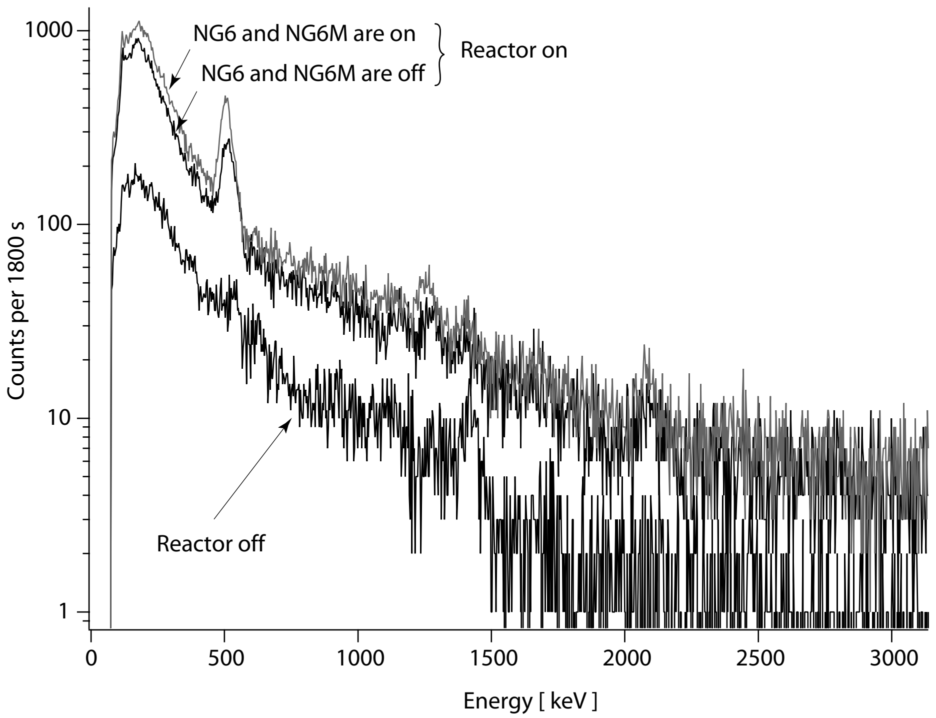

Figure 4.16: The spectrum of the NaI detector described in the text. Energy calibration is performed using a ^{60}Co source. The peak at 480 keV is attributed to neutron capture on ^{10}B.

by a factor of 1000, the presence of this peak is most likely due to the gaps in the coverage of the apparatus by the shield. The number of counts produced in the NaI detector is recorded every 5 s by the DAQ as described in Section 3.1.

The NaI data can be used to monitor the external backgrounds with the goal of selecting the runs with consistent background conditions. An example of a run where the ambient gamma conditions have changed during the course of the observation period is shown in Figure 4.17. The jump at $t \approx 2000$ s corresponds to closing the neutron shutter of the NG6M instrument. Although the status of the neutron beam shutters for the two adjacent experimental installations (NG6 and NG6M) is independently monitored and recorded by the DAQ, the status of the other beam

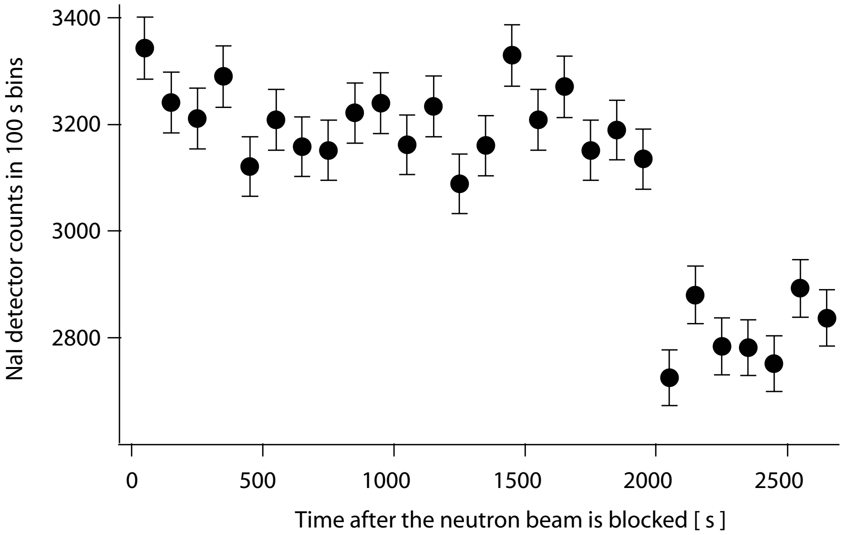

Figure 4.17: The counting rate of the NaI detector during run 071303009. The drop in the rate 2000 s after the start of the observation period is due to the change in beam on/beam off status of the nearby beam line (NG6M).

lines may change without being recorded and may produce a similar shift in gamma background.

The gamma background detected by the NaI detector and the signal detected inside the cell are highly correlated. Figure 4.18 shows the average cell counting rate for the last 400 s of the run versus the average counting rate of the NaI detector over the same period of time. The contribution to the cell signal due to neutron decays (present only in the trapping runs) is at most 0.1 s^{-1}. Although the cell background and NaI counting rates are correlated, the large χ^2 of the linear fit (also shown in Figure 4.18) indicates the presence of background sources in the cell that are not observed by the NaI detector.

The efficiencies of the cell and NaI detectors depend on the energy of the ambient gammas and their source location. Since the NaI detector is placed roughly 1 m from

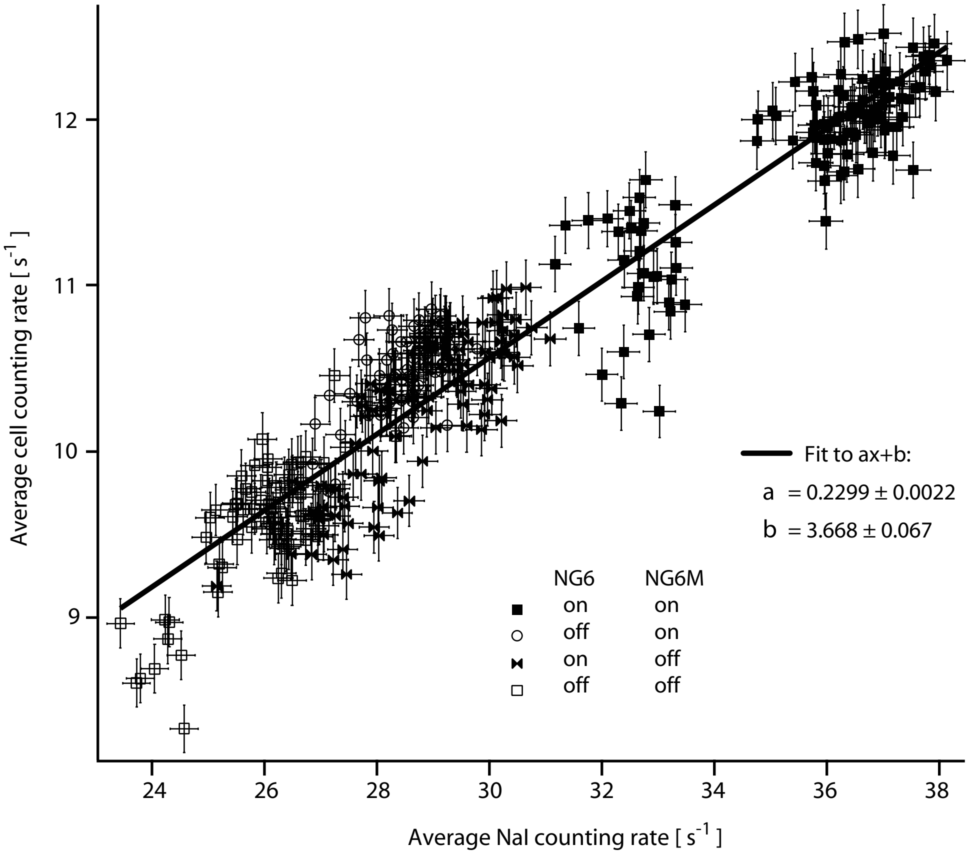

Figure 4.18: The average counting rate (3+3+ cut) from the experimental cell is plotted versus the average NaI detector rate. The rates are averaged over the last 400 s of the 354 "Cold1" runs. The χ^2 of the fit is $\chi^2 \approx 3.26$.

the helium-filled cell, these efficiencies may change when the source of the gamma background changes. The two detectors also subtend different solid angles.

Nevertheless, one can attempt to "correct" the cell signal for changes in the ambient backgrounds using NaI data. Suppose that

$$T(t) = n(t) + b_i(t) + b_e(t)$$

is the cell detector counting rate in a trapping run, and

$$B(t) = b_i(t) + b'_e(t)$$

Table 4.9: The results of the fits of the deference between trapping and background runs for the "Cold1" (old bases only) data set with and without corrections for the changing external backgrounds. Fits are to $y + A\exp(-t/\tau)$, starting at $t_0 = 150$ s. The data is binned in 5 s bins.

Data Set	y, s^{-1}	A, s^{-1}	τ, s	χ^2
No corrections	0.05 ± 0.02	2.03 ± 0.06	$627.8^{+33.8}_{-30.5}$	0.99
Background corrected data	0.06 ± 0.02	1.94 ± 0.06	$645.9^{+39.8}_{-35.4}$	0.99

is the counting rate in a background run. Here, $n(t)$ is the signal due to neutron decay events and, $b_i(t)$ and $b_e(t)$ are "internal" and "external" backgrounds respectively. The "internal" background events may be registered only inside the cell and are thought to be primarily due to the incoming neutron beam (i.e. luminescence or activation of the materials inside the cell). We assume that $b_i(t)$ depends only on the incoming neutron flux and is identical in the trapping and background runs. The change in the "external" backgrounds (i.e. ambient gammas) may be monitored by the NaI and, in general, is not the same in the trapping and background runs, $b_e(t) \neq b'_e(t)$. If $T_G(t)$, the NaI detector counting rate during a trapping run, is proportional to $b_e(t)$, $T_G(t) = kb_e(t) + c$, and the same proportionality holds for the background runs, $B_G(t) = kb'_e(t) + c$, then

$$n(t) = (T(t) - b_e(t)) - (B(t) - b'_e(t)) = \big(T(t) - \frac{1}{k}T_G(t)\big) - \big(B(t) - \frac{1}{k}B_G(t)\big).$$

The coefficient $1/k \equiv a$ is determined from a linear fit to the data shown in Figure 4.18.

The difference between the trapping and background runs in data set "Cold1" with and without the above mentioned background correction is shown in Figure 4.19. The results of the fits to the two data sets are shown in Table 4.9. The estimate of the trap lifetime after this correction is consistent with the estimates using the uncorrected

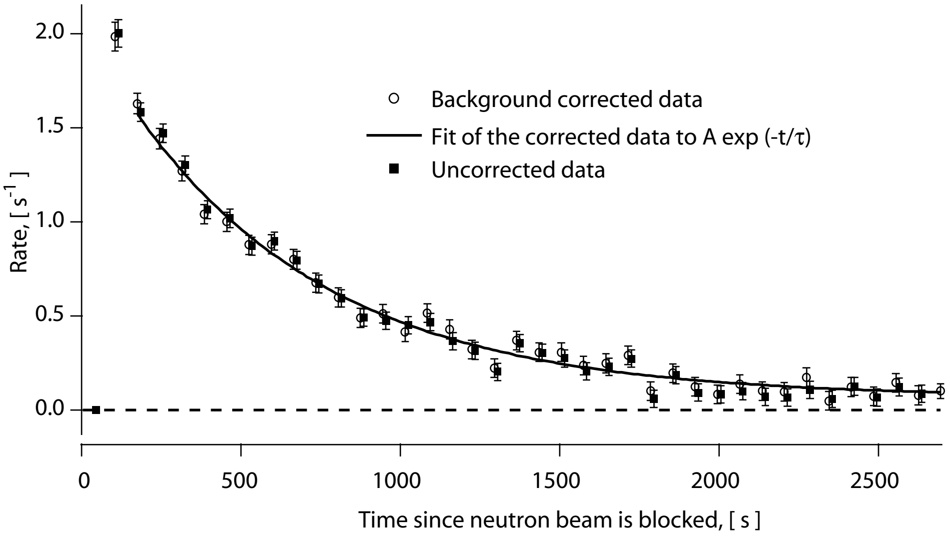

Figure 4.19: The difference between the trapping and background runs in the "Cold1" data set (old bases only) binned in 70 s wide bins. The background corrected data and the data before corrections are shown. The uncorrected data is offset horizontally for visualization purposes.

data, but with somewhat larger error bars.

As is the case with the gain shift corrections discussed in Section 4.7, the corrections for the changes in the external background could become a more important issue when the statistics of the measurements improves.

4.9 KAMFEE Card Data

An alternative digitizing card (KAMFEE card) was added to the DAQ system as an independent check of the data acquired by the Signatec cards. The discovered irregularities in the operation of the Signatec cards are described in more detail in Section 3.2. The hardware setup is described in Section 3.1, the data analysis procedures are discussed in Section 3.3.

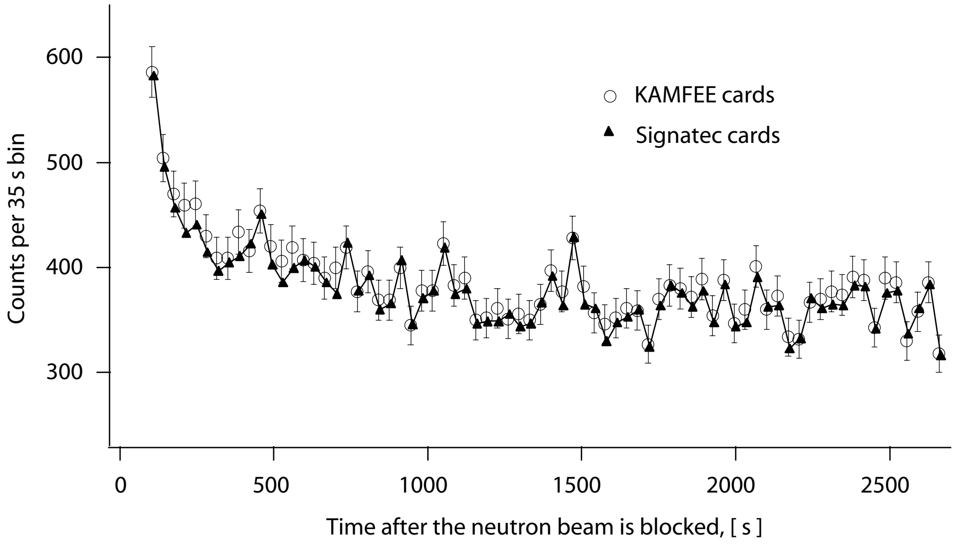

Figure 4.20: The comparison between the KAMFEE and Signatec card data. Shown are the count rates during one run after applying a software cut with a lower threshold of 3 photoelectrons in each PMT.

The PMT pulses are digitized concurrently by both the KAMFEE and Signatec cards. The digitized pulses from each card are parsed and the software cut that requires at least 3 photoelectrons in each PMT is made. The time stamps of the events that pass the cut are then histogrammed. A comparison between the counting rates obtained by the two cards during one run is shown in Figure 4.20. As can be seen, the agreement is quite good. The small difference between the rates can be explained by somewhat different cut levels.

The digitization with both cards was performed during a subset of the "Magnet-Ramp2" data set that consists of 55 trapping and 47 background runs. The results of fits to the difference between the trapping and background runs to a 2-parameter model[6] $A\exp(-t/\tau)$ are consistent for both cards: $(0.95 \pm 0.09)\exp(-t/854^{+91}_{-75})$ s^{-1}

---

[6] The fits to the 3-parameter model $A\exp(-t/\tau) + y$ indicate that the parameter y is consistent with zero.

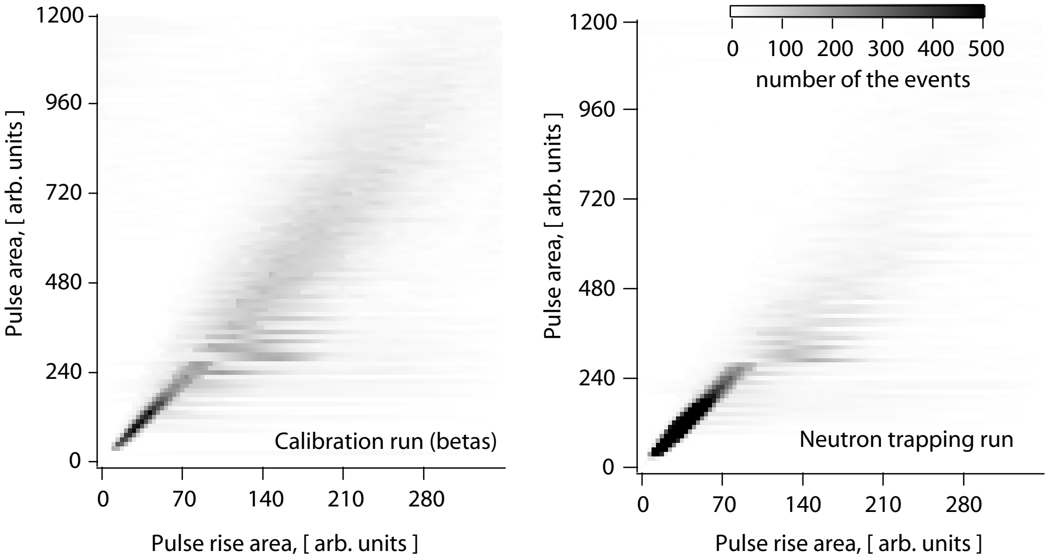

Figure 4.21: The dependence of the total area of the PMT pulse digitized by the KAMFEE card on the "rise area" of the pulse (see Figure 3.9). The total number of events is equal in two graphs. 3+ software cuts correspond to roughly 260 units of the total area.

for the Signatec card data and $(0.84 \pm 0.08)\exp(-t/840^{+100}_{-81})$ s^{-1} for the KAMFEE card data[7].

In order to explore the possibility of distinguishing background events originating in the acrylic from the events that originate in the helium, we histogram and plot the number of pulses with certain "total area" and "rise area" of the digitized pulse, (see Figures 3.9 and 4.21). The fraction of the multiphoton events that are produced in the helium rather than in the acrylic light guide is larger in the calibration run data (beta-active ^{113}Sn source is placed inside the cell in these runs, see Section 4.10; roughly 7 photoelectrons on average are produced at the PMT's photocathode during this run). Unfortunately, we do not observe any features in the graph that would make it possible to discriminate the helium pulses from the acrylic pulses based on their

---

[7] The fit starts 250 s after the neutron beam is blocked. Time t is in seconds.

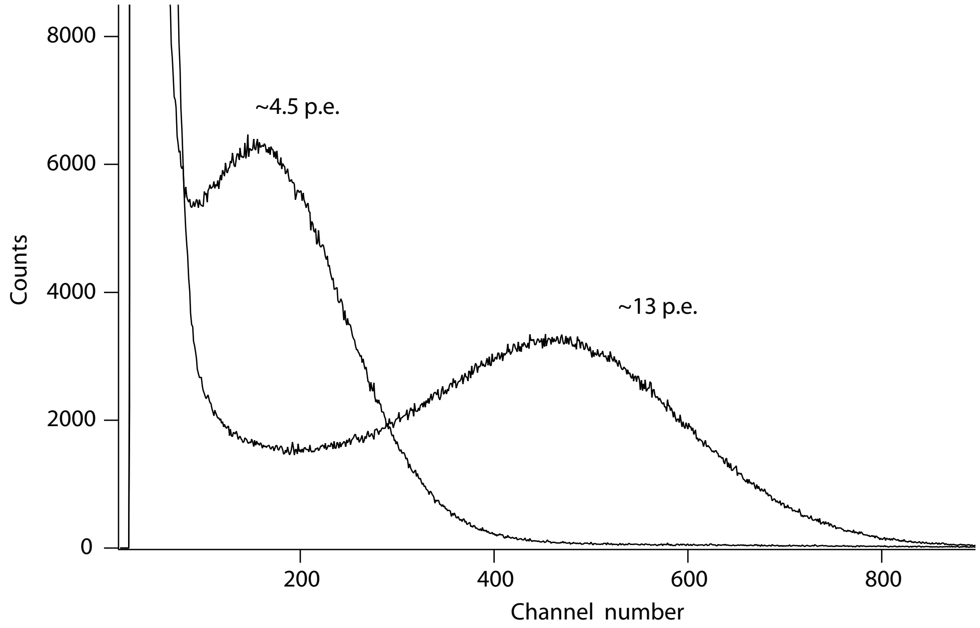

Figure 4.22: The pulse-height spectra of the PMT pulses for two different locations of a calibration beta source inside the detector. Details of the calibration are described in the text.

“total area”/“raise area” ratio.

4.10 Detector Calibration

The setup for calibrating the detector using a beta source mounted on a linear motion stage inside the liquid helium bath is described in Section 2.6.2.

In the first set of measurements, a single PMT (β) is mounted at the end of the 77 K light guide and the pulse-height spectra are observed for different source locations. Typical pulse-height spectra for two source positions are shown in Figure 4.22. As expected, the position of the peak from the 364 keV beta emitted by ^{113} source depends on the position of the source. This dependance is shown in Figure 4.23. The

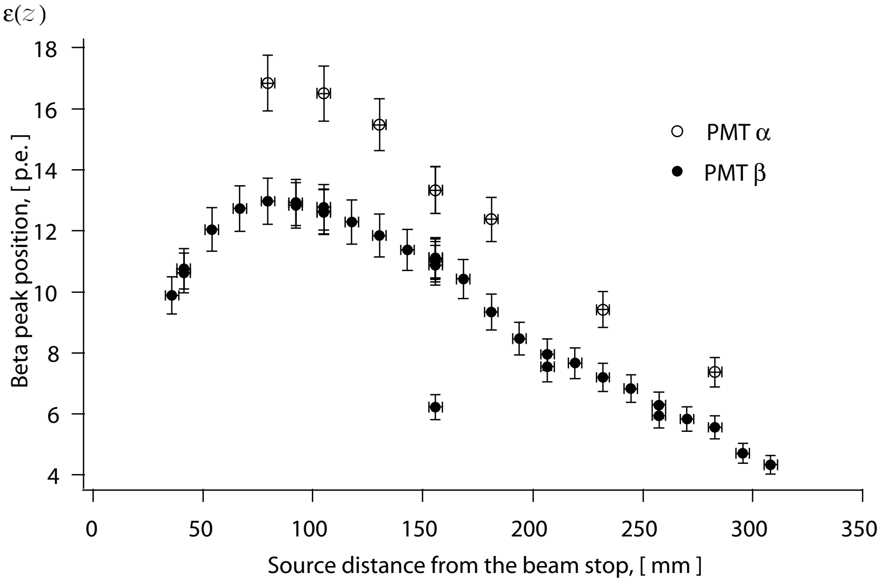

Figure 4.23: The spectrum peak positions from the 364 keV ^{113}Sn beta source. A single PMT (α or β) is mounted to the end of the 77 K. 175 mm corresponds to the center of the trapping region.

position of the beta peak is estimated by fitting the spectra shown, for example, in Figure 4.22 to a Gaussian plus linear function. The peak positions reported by the fitting routine are somewhat sensitive to the fitting region, especially in cases where the beta peak is close to the one-photoelectron peak, but are consistent to within 5 %. In addition, it is observed that the ratio of the positions of the beta peak and 1 p.e. peak decreases with the increase in distance between the source and the beamstop. This is due to light loss from the reflections from the TPB/Gore-Tex. This ratio also drops when the source is positioned very close to the beamstop, corresponding to a decrease in solid angle covered by the TPB. A faster drop in the central part of the cell is possibly due to a less efficient evaporation of the TPB layer at the edges of the two Gore-Tex sheets. PMT α is about 30 % more efficient as compared to PMT β

due to its higher quantum efficiency. The peak in the detection efficiency of PMT α at 16.9 photoelectrons corresponds to roughly 46.4 p.e./MeV.

Since the motor operation for moving the beta source heats up the cell, the temperature of the cell during the position dependance measurements is kept between 1.4 K and 1.6 K, where the cooling power of the refrigerator is higher. To verify that the detection efficiency does not depend strongly on the temperature below 1.6 K, the temperature of the cell is decreased to 300 mK while the position of the source is kept fixed. The location of the beta peak in the pulse-height spectrum did not change within 5 %. Thus, we expect the same position dependance of the detection efficiency at 300 mK as is measured in the 1.4 K to 1.6 K region.

In order to estimate the detection efficiency of the system for neutron beta decay events, a Monte-Carlo simulation similar to one described in Ref. [54] is developed. The axial neutron decay position (z) is drawn from a uniform distribution inside the trapping region. Then the electron energy (E, keV) of the neutron decay event is chosen based on the neutron beta decay spectrum. The total number of photoelectrons that are produced by neutron decay is then $\epsilon_{\alpha,\beta}(z)(E/364)$, where $\epsilon_{\alpha}(z)$ is a relative detection efficiency measured in Figure 4.23. In a two-PMT setup, the light is split between PMTs α and β[8] based on Poisson statistics, but due to the lower quantum efficiency of PMT β, the average number of the photoelectrons detected by this PMT is somewhat smaller.

The chance that a neutron decay is detected when a certain number of photoelectrons are required in each PMT is shown in Table 4.10. The estimates of the

---

[8] A comparison of the peak positions in a single PMT and two-PMT setups shows that ≈ 6 % of the light is lost in the light splitter.

Table 4.10: The neutron decay detection efficiency at different threshold levels.

Cut level, p.e.	Efficiency, %
1+1+	84 ± 4
2+2+	65 ± 5
3+3+	48 ± 6
4+4+	34 ± 7
5+5+	23 ± 7

detection efficiency are used in the calculation of the number of neutrons in the trap and to check the theoretical predictions of the UCN production rate inside the trap (see Section 4.3).

One comment must be made about the results of the calibration run. In order to prepare the apparatus for the calibration run, the PMTs had to be taken off and then remounted to the end of the light guide. Thus the calculation of the detection efficiency relies on a consistent quality in optical coupling of the PMTs to the light guide. Any imperfections in the optical contact made using optical grease to avoid air gaps between the PMT window, acrylic coupler, light splitter, and the light guide, will lead to light attenuation. Since it is not possible to observe directly the quality of the optical contacts between all surfaces, our best effort is made to maintain the same techniques and procedures for mounting the components. Still, the possibility of a somewhat different efficiency of PMT coupling during the neutron and calibration runs remains. Possible improvements to the current setup are discussed in Chapter 6.

Chapter 5

Marginally Trapped Neutrons and Other Systematic Effects

5.1 Marginally Trapped Neutrons

5.1.1 Semi-stable Orbits

Neutrons in low-field seeking spin state with energy less than the trap depth are trapped by a magnetic field of the trap. However, neutrons with energy larger than the trap depth may also be confined in the trap for an extended period of time. Indeed, consider a neutron moving on the circular orbit of radius r in a plane perpendicular to the axis of the trap. The total energy of the neutron on this orbit is

$$E = \frac{mv^2}{2} + \beta r,$$

where $mv^2/2$ is the kinetic energy and $\beta r = \mu_n B(r) = V_p$ is the potential energy due to the magnetic field $B(r) = B_0(r/R)$. The trap depth is $E_T = \mu_n B_0 = \beta R$. For a neutron on the circular orbit

$$\frac{mv^2}{r} = \frac{\partial}{\partial r}(\beta r) = \beta,$$

and the energy of a neutron on such orbit for a case of $(r = R)$ is

$$E = \frac{3}{2}\beta R = \frac{3}{2}E_T > E_T. \tag{5.1}$$

Neutrons with energy above the threshold $(E > E_T)$ that eventually decay inside the trap just increase the effective number of trapped neutrons. The problems arise if neutrons leave the orbit after a period of time comparable to the neutron beta decay lifetime. Then these neutrons may undergo collisions with the material walls and have a chance of leaving the trap through these collisions. This loss mechanism introduces a systematic error in the measurement of the neutron lifetime.

The trajectories of the neutrons in a magnetic field of the trap may be simulated numerically by solving the equations of motion

$$\frac{d\vec{p}}{dt} = -\frac{\partial V_p}{\partial \vec{r}}. \tag{5.2}$$

The numerical solution of these equations using standard Runge-Kutta methods and more specialized symplectic integration [101] encounter problems after tracking neutron trajectories for more than 5 seconds [102]. After 5 seconds the solutions do not converge as the size of the integration steps decrease.

Although we can not reliably track all neutron trajectories for a long time, an experimental procedure can be implemented to remove the above-threshold $(E > E_T)$ neutrons from the trap.

Following Ref. [103], consider lowering the magnetic trap depth $(\beta = \beta_i \rightarrow \beta_f)$ after the trap is loaded. Again, we consider a two-dimensional case. The angular momentum L is conserved in a centrally symmetric field and the energy of the neutron may be expressed as

$$E = \frac{L^2}{2mr^2} + \frac{p_r^2}{2m} + \beta r.$$

Since the system is not closed during the magnetic field ramp, the energy of the neutron is not conserved. However, if the magnetic field is changing slowly ($\dot{\beta} \ll \beta/T$, where $T \sim 0.1$ s is the neutron motion period in the trap), the action is the adiabatic invariant [104] and

$$I = \oint p_r dr = 2\int_{r_{min}}^{r_{max}} \sqrt{2m(E - \beta r) - \frac{L^2}{r^2}} dr = const, \tag{5.3}$$

where r_{min} and r_{max} are the minimum and maximum radii of the neutron trajectory.

One may show that the quantity βr_{max}^3 is conserved during the ramp [103]. As the trap depth decreases, the neutron trajectory "expands". We want to lower the magnetic field to a level that the trajectories of all the neutrons with energy $E > E_T$ expand to $r > R$. Then these neutrons will have a chance of leaving the trap through the wall collisions. Note, that since the total energy of the neutron may be expressed as

$$E = \beta r_{max} + \frac{L^2}{2mr_{max}^2}, \tag{5.4}$$

and L is also conserved, the quantities Er_{max}^2 and $E\beta^{-2/3}$ are also conserved during the slow magnet ramp.

Among all the trajectories that neutrons of energy equal to the trap depth $E_T = \beta_i R$ may have, the circular orbit has the minimum value of r_{max}. From Eq. (5.1) it follows that this value is equal to $2R/3$. In order to lose the neutrons on these trajectories, ramping the magnetic field down must expand the trajectory to $r_{max} =$

R, and

$$\frac{\beta_f}{\beta_i} = \left(\frac{2R/3}{R}\right)^3 \approx 0.3.$$

Thus, lowering the magnetic field to 30 % of its initial value guarantees that after restoring the magnetic field, there will be no neutrons with energy $E > E_T$ that do not undergo collisions with the walls of the trap when the magnetic field is lowered.

In three dimensional Ioffe-type trap the radial and axial motions of the neutrons are coupled [105], which increases the efficiency of the magnet ramps for eliminating the above-threshold neutrons.

5.1.2 Confinement by the Material Walls

Gore-Tex tube with evaporated layer of TPB create a material bottle for UCN. Neutrons with energy less than the trap depth ($E < E_T$) do not collide with the walls, while the neutrons with higher energies (above-threshold neutrons) can undergo collisions (although, as Section 5.1.1 shows, some of these above-threshold neutrons may also be trapped purely magnetically). If neutron kinetic energy at the moment of the collision is small, the probability of reflection is high, but certainly less than unity. The non-zero wall collision loss rate introduces a systematic error in the measurement of the neutron lifetime.

As shown in Section 5.1.1, lowering the magnetic field to roughly 30 % of the initial value leads to collisions of all above-threshold neutrons with the walls. Ideally, we want to keep the magnetic field low for long enough to ensure that none of the neutrons left in the trap after raising the field have sufficient energy to reach the walls of the trap.

The reflection probability for the neutron-wall collision may be estimated by treating the wall as a potential barrier with a complex potential $U = V - iW$ [30]. The real part of the potential, V, is the Fermi potential of the material that depends on the coherent scattering length a of the material and its number density n: $V = 2\pi\hbar^2 na/m_n$. The complex part of the potential, W, describes neutron losses: $W = \hbar n\sigma_l v/2$. Here m_n and v are the mass and the velocity of the neutron respectively, $\sigma_l = \sigma_{abs} + \sigma_{ie}$ is the loss cross section that includes the absorption and inelastic scattering components.

The solution of the Schrödinger equation for the free neutron approaching the barrier with a potential U gives the neutron reflection probability [30]:

$$r = \frac{E_n - \sqrt{2E_n(\alpha - (V - E_n))} + \alpha}{E_n + \sqrt{2E_n(\alpha - (V - E_n))} + \alpha}, \tag{5.5}$$

where $\alpha = \sqrt{(V - E_n)^2 + W}$, and E_n is the perpendicular to the wall component of the neutron's kinetic energy.

To estimate atypical wall loss time constants, consider a neutron on a linear radial trajectory along the x axis that passes through the center of the trap. Assume that the magnetic field of the trap creates a linear potential $V = \beta|x|$ and that the material walls are located at $|x| = R$. If the energy of the neutron E is larger than the trap depth $E_T = \beta R$, then the motion period may be obtained by integrating the equations of motion (5.2) directly:

$$T = 4R\frac{\sqrt{2mE}}{E_T}(1 - \sqrt{1 - E_T/E}).$$

If the reflections are specular and elastic, the neutron stays on the same linear trajectory and the kinetic energy at the moment of the collision with the wall is $E_c = E - E_T$. Based on the per-bounce reflection probability r given by Equation (5.5), we can calculate the wall loss time as $T_{wall} = T/(1 - r)$.

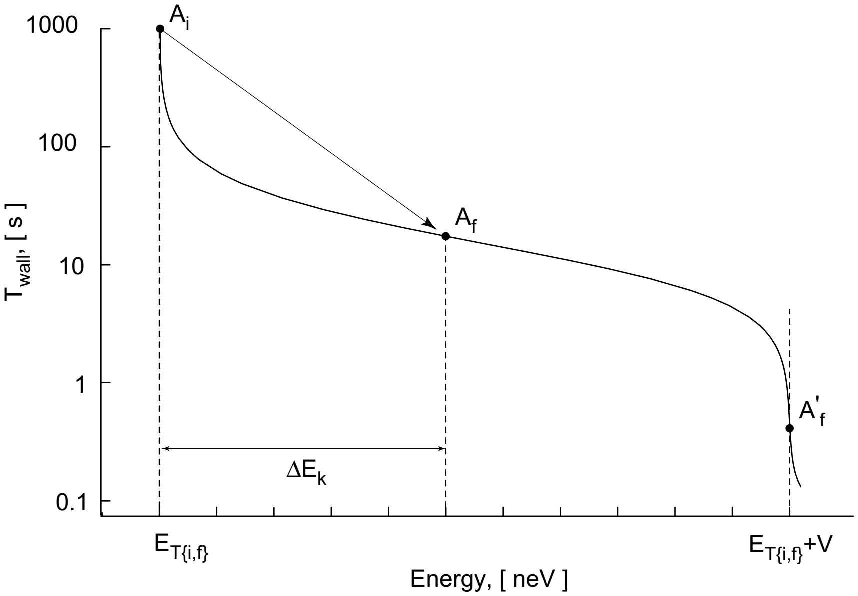

Figure 5.1: The calculated wall loss time for a neutron on a linear trajectory $(z = 0)$ as a function of neutron energy. In calculations we assume the trap depth is $E_T = 66$ neV (1.1 T); the TPB surface/helium potential difference is $V = 22$ neV; the imaginary part of the potential $W = 2 \times 10^{-3}$ neV is determined by the hydrogen content of the TPB.

The estimates of T_{wall} as a function of neutron energy for the linear trajectory discussed is shown in Figure 5.1. Here we assume that the trap is $E_T = 66$ neV deep (1.1 T). The effective potential of the TPB coating on the surface of the Gore-Tex tube that forms a material wall at $R = 4.3$ cm is $V = V_{\text{TPB}} - V_{\text{He}} \approx 42$ neV-20 neV$=$ 22 neV. The loss on the wall at 300 mK is predominantly due to the neutron capture on hydrogen and the imaginary part of the potential may be estimated (using $\sigma_{abs} v \approx 10^3$ b m s^{-1} [30] and $n_{\text{H}} \approx 6 \times 10^{22}$ cm^{-3}) as roughly $W = 2 \times 10^{-3}$ neV [30]. The loss time becomes infinite for $E \leq E_T$, corresponding to no wall collisions, and drops rapidly at $E \geq E_T + V$ as neutrons start penetrating through the material wall. In the intermediate energy region, a typical wall loss time in this case is on the order of ten seconds.

For the discussed linear trajectories, the kinetic energy has only perpendicular to the wall component. The diffusive collisions that occur because of the "waviness" of the surface, provide coupling between normal and tangential to the wall components of energy. For a given neutron energy the average normal to the wall component will be smaller than in the linear trajectory case, leading to higher reflection probability and longer wall loss times.

The phase space available for the production of UCN with energy E is proportional to $\sqrt{E}dE$ (see Appendix A). The calculations of UCN production rates inside the potential defined by the $V = 22$ eV potential of the material wall located at $R = 4.3$ cm in addition to the linear magnetic potential of $E_T = 66$ neV deep trap (see Appendix A) show that the ratio of the number of neutrons produced with the total energy less than E_T to the number of neutrons that have energy less than $E_T + V$, including those that may undergo collisions with the walls, is roughly 0.4. The characteristic time for wall absorption depends on the neutron trajectory and is on the order of tens and hundreds of seconds.

Interesting to note, that if one takes two exponential functions $1.3\exp(-t/885)$ and $0.8\exp(-t/300)$, corresponding to "truly" and "marginally" trapped neutrons, then their sum fits to $1.9\exp(-t/637)+0.05$ (fit range 150 s to 2680 s). Although it is unlikely that a single exponential model provides an adequate description of the time dependance of the wall loses, the positive offset and the value of the lifetime obtained in the fits suggest that the fits of the data taken in the runs without magnetic field ramp ("Cold1" data set described in Section 4.3) may be due to the presence of long-lived above-threshold neutrons in the trap.

As shown in Section 5.1.1, the value of $E\beta^{-2/3}$ remains constant during the magnet ramp and thus the neutron energy after the ramp $\beta_i \rightarrow \beta_f$ becomes $E_f = E_i(\beta_f/\beta_i)^{2/3}$. The kinetic energy of the neutron at the edge of the trap is then $E_{k,f} = E_f - \beta_f R$. For a neutron with initial energy E_i equal to the trap depth $E_{T,i} = \beta_i R$, the minimum kinetic energy at the wall is

$$\Delta E_k = E_{T,i}\Big(\Big(\frac{\beta_f}{\beta_i}\Big)^{2/3} - \frac{\beta_f}{\beta_i}\Big).$$

If the field is ramped to 30 % of its original value, then $\Delta E_k \approx 0.148 E_{T,i}$. This means that above-threshold neutrons will have a kinetic energy of at least 10 neV at the moment of the wall collision (for a 66 neV deep trap). A neutron with initial energy $E_{T,i}$ (point A_i in Figure 5.1) will have kinetic energy of 10 neV at $r = R$ after the magnetic field is lowered (point A_f)[1]. Neutrons corresponding to point A_f are lost from the trap in roughly 15 s.

As one can see, the estimates of the wall loss time even for the liner trajectory are comparable to the duration of the ramp. It should be noted, that the minimum kinetic energy at the edge of the trap for the same fractional filed ramp is proportional to the trap depth. For the trap depth of 150 neV (2.5 T), the neutrons from point A_i will reach point A'_f where they have enough energy to penetrate the wall; at these energies even one collision with the wall may be enough for a neutron to leave the trap. The trap depth of the next generation trap is expected to be 190 neV (3.1 T), corresponding to roughly 28 neV minimum kinetic energy at the edge of the trap.

---

[1] Note that after the field is lowered $E_{T,f} = 0.3 E_{T,i}$, so the energy of the neutron is decreased: $E_{A_f} \approx 0.448 E_{A_i}$

In more general case, the kinetic energy of the neutron at the moment of the collision with the surface has normal and tangential to the surface components. Only the normal component determines the reflection probability that becomes larger as the normal component of the energy decreases.

In a new trap design (see Chapter 6), the minimum kinetic energy of above-threshold neutrons at the edge of the trap after ramping the magnetic field down to 30 % is 28 neV, while normal kinetic energy of 22 neV is required to penetrate the potential barrier. If the reflections from the walls are diffuse, then it takes roughly five collisions for a neutron to get enough normal energy to leave the trap. For a typical collision rate of 10 Hz it means that above-threshold neutrons can be eliminated in several seconds.

5.2 Other Systematics

Neutrons in a low-field seeking spin state that have kinetic energy below the trap depth are confined by the magnetic field until they beta decay. However these neutrons could depolarize, becoming high-field seekers. The neutrons in the high-field seeking spin state are pushed out of the trap by the magnetic field, thus producing loses that can introduce a systematic error in the measurement of the neutron lifetime. The neutron depolarization may occur in the regions of low field magnitude (Majorana spin-flip transitions) or by spin-orbit and spin-spin interactions with the electrons and ions that are present in liquid helium.

The estimates of the depolarization can be made semi-classically by considering the motion of a spin in a magnetic field governed by [106]:

$$i\hbar\frac{d}{dt}\begin{pmatrix}\varphi_1\\ \varphi_2\end{pmatrix} = -\mu_n\vec{\sigma}\cdot\vec{B}\begin{pmatrix}\varphi_1\\ \varphi_2\end{pmatrix},$$

where $\binom{\varphi_1}{\varphi_2}$ is a spinor describing spin orientation. In terms of vector components, the last expression can be written as

$$\frac{d}{dt}\begin{pmatrix}\varphi_1\\ \varphi_2\end{pmatrix} = i\frac{\mu_n}{\hbar}\begin{pmatrix}B_z & B_x - iB_y\\ B_x + iB_y & B_z\end{pmatrix}\begin{pmatrix}\varphi_1\\ \varphi_2\end{pmatrix}. \tag{5.6}$$

A neutron on the trajectory that passes through the center of the trap, where the magnetic field is minimal, has the highest chance of depolarization through the Majorana spin-flip. One may consider a linear radial trajectory, where the magnetic field can be approximated as $\vec{B} = (\beta x, 0, B_0)$, and solve the Equation (5.6) with the initial condition of $\binom{\varphi_1}{\varphi_2} = \binom{1}{0}$. For $B_0 \approx 0.1$ T in our current trap design, the depolarization rate on these linear orbits, presenting an upper bound, is on the level of 10^{-4} of the neutron beta-decay rate. The increase in B_0 to 0.2 T makes the size of the effect due to the Majorana spin-flip transition less than 10^{-5} [53].

The depolarization of neutron due to neutron-neutron dipolar interactions is negligibly small due to the extremely small density of UCN in the trap (roughly 3 cm^{-3}). However, the spin-orbit and spin-spin interactions with other species that may be present in liquid helium, such as ions and electrons, may have larger effect. The electrons and ions are produced during ionization events in the helium. Most of them immediately recombine to form He$_2$ molecules that subsequently decay into helium atoms. Some electrons, however, may escape recombination and form "bubbles" inside the helium. Assume that electron can escape recombination with the ion at a distance r_e such that $e^2/r_e = 3k_BT/2$. For $T = 300$ mK, $r_e \approx 15$ μm.

In the “worst case” scenario, all the energy of the alpha particles produced during the neutron capture on Boron (element present in a beam stop that captures most of the neutrons entering the cell), goes to ionize helium. For roughly 10^8 neutrons entering the cell per second, the energy of the alpha particles of 1.5 MeV and the helium ionization energy of 25 eV, the number of electron-ion pairs produced per second is $P = 10^8 \times 1.5 \times 10^6/25 \approx 6 \times 10^{12}\ \mathrm{s}^{-1}$. If n is the average density of the electrons in the helium during the trap loading, then $P = \sigma_e v n^2 V$, where $\sigma_e \approx r_e^2 = 2 \times 10^{-6}\ \mathrm{cm}^2$ is a recombination cross section, $V \approx 1500\ \mathrm{cm}^3$ is the volume of the trap and $v = \sqrt{3k_B T/m_{eff}} \approx 7\ \mathrm{m\,s}^{-1}$ is the typical velocity of the ions. From this we can estimate the upper bound on the electron density in the helium as $n \sim 10^6\ \mathrm{cm}^{-3}$.

The spin-flip probabilities can be estimated by solving equations (5.6) for the interaction of the magnetic moment of the neutron with the magnetic field produced by moving charge ($B_{so} \propto ev/r^2$) or the electron magnetic moment ($B_{ss} \propto \mu_e/r^3$). The calculations for a typical velocities of $v \sim 10\ \mathrm{m\,s}^{-1}$, give cross sections $\sigma_{so} \sim 10^{-26}\ \mathrm{cm}^2$ and $\sigma_{ss} \sim 10^{-18}\ \mathrm{cm}^2$. Then the characteristic time for the spin-flip is $\tau_f = 1/(n(\sigma_{ss} + \sigma_{so})v) \sim 10^9$ s.

In addition to depolarization, the neutrons can be lost from the trap by neutron capture on ^{3}He nuclei[2], thermal upscattering by the excitations in the liquid helium or due to the magnetic field fluctuations.

The neutron capture cross section for ^{3}He is $\sigma = \sigma_{th} v_{th}/v$, where $\sigma_{th} = 5333$ b is the thermal neutron ($v_{th} = 2200\ \mathrm{m\,s}^{-1}$) capture cross section and v is the ^{3}He velocity with respect to the neutron. The rate of neutron capture events on ^{3}He

---

[2] All other possible impurities should be solidified at 300 mK and stay at the walls.

is $k_3 = \sigma n_3 v = \sigma_{th} n x v_{th}$, where n is the number density of the helium and x is the ^{3}He/^{4}He ratio. Then the ratio of the rate of neutron capture on ^{3}He to the beta-decay rate k_β is

$$\frac{k_3}{k_\beta} = 2.3 \times 10^{10} x.$$

The preliminary results of the measurements of ^{3}He content in the isotopically purified helium that was used in our experiment show $x \approx 2.5 \times 10^{-13}$ [64], but the heat flush technique used for the isotopic purification is capable of producing helium with the isotopic purity of $x < 5 \times 10^{-16}$ [107].

Thermal upscattering at low temperature is dominated by the multiple-phonon events with the theoretical upscattering rate proportional T^7 [58, 59]. Scaling our measured upscatteing rate at 500 mK (see Figure 4.9) to lower temperatures, one may find that thermal upscattering presents a 10^{-5} level correction to the neutron lifetime at helium bath temperatures of $T < 130$ mK. In any case, the upscattering is expected to drop as temperature decreases. The existing experimental techniques allow, in principle, cooling of the helium bath to a temperature below 50 mK.

The fluctuations of the magnetic field may also cause neutron losses. The magnetic field fluctuations lead to the change in potential energy of the neutrons $E_p(r,t) = \mu B = E_{p0}(r)(1+\epsilon(t))$. In case of random fluctuations $\epsilon(t)$ with correlation function $K(t)$, $\overline{\epsilon(t)\epsilon(t')} = \epsilon_0^2 K(t-t')$. The variation of neutron energy during time τ is given by [29]:

$$\overline{(\Delta E)^2} = \iint_0^\tau \epsilon_0^2 K''(t'-t'') E_{p0}(r(t')) E_{p0}(r(t'')) dt' dt''.$$

For the model of $K(t) = \exp(-t/t_0)$, we find $\overline{(\Delta E)^2} < \epsilon_0^2 \tau \max(E_{p0}^2(r))/t_0$. The lifetime τ is then $\tau > t_0/\epsilon_0^2$. For $t_0 = 0.1$ s and $\epsilon_0 = 0.01$ %, $\tau > 10^7$ s.

Table 5.1: Estimates of the errors on the lifetime (in seconds) due to systematic effects. The statistical error of the measured trap lifetime for the data set with magnetic field ramping is (+74/-63) s.

Systematic effect	Current setup	Achievable limit
Marginal trapping	200 (w/o ramping)	
	$\lesssim 30$ (with ramping)	< 0.01
Imperfect background subtraction	21	< 0.01
Detection efficiency drifts	8	< 0.01
Neutron absorption on ^{3}He	5	< 0.01
Neutron depolarization	0.2	< 0.01
Magnetic field fluctuations	< 0.1	< 0.01
Medium (helium) effects	< 0.01	< 0.01

Finally, the fact that the neutron decay occurs in the liquid helium changes the phase space available for the decay products[3]. The change in the neutron beta-decay rate due to the presence of helium is less than $10^{-5}\tau_\beta^{-1}$ [53].

Systematic effects are summarized in Table 5.1. The largest systematic error is due to the presence of neutrons with energy higher than the magnetic trap depth. The majority of the above-threshold neutrons in current setup are removed from the trap by lowering the magnetic field of the trap to 30 % of its maximum value and then raising it back. The field ramping leads to wall collisions of marginally trapped neutrons, including those on semi-stable orbits discussed in Section 5.1.1. In current trap configuration the above-threshold neutrons have kinetic energy of at least 10 neV (see Section 5.1.2) during the wall collision when the field is lowered. This energy may be not enough to penetrate the wall (V=22 neV), but the probability of absorption during this time is increased. The rough estimate of the number of above-threshold neutrons that are left in the trap after the field ramp in current trap configuration may be obtained by assuming the "worst case" wall loss time of 15 s (see

---

[3] The potential barrier that liquid helium presents for an electron is roughly 1 eV.

Figure 5.1) during the time when the field is lowered. Assuming a typical duration of a low-field period of 50 s, we can estimate the upper limit on the fraction of the above-threshold neutrons left after ramping as 4 %. Then, using a two-exponential model from Section 5.1.2 (with the appropriate decrease in signal amplitude) we can estimate the bias in lifetime estimates due to the presence of marginally trapped neutrons not removed by the field ramping as roughly 30 s. These estimates are quite crude, but, fortunately, the next generation of the trap (see Chapter 6) with the trap depth of 3.1 T will provide above-threshold neutrons enough energy to penetrate the walls after the field lowered (see Section 5.1.2) and all the above-threshold neutrons will be eliminated in several seconds.

The effect of the imperfect background subtraction is estimated based on the data with natural helium in the cell (see Section 4.6) and presents an experimental upper bound. The detection efficiency drifts are discussed in Section 4.7.

Additional measurements of the isotopic purity of the helium are necessary to give direct experimental confirmation of the isotopic purity achievable by the heat-flush technique [107].

With the improvements in the experimental setup (see Chapter 6), it should be possible to control the identified systematic effects to 10^{-5} level.

Chapter 6

Conclusions and Prospects

6.1 Summary of the Results

The obtained experimental results conclusively demonstrate the magnetic trapping of neutrons, extend the temperature range of the thermal upscattering rates measurements for UCN in liquid helium and indicate the presence of the above-threshold neutrons in the trap. The experimental data also shows the improvements necessary to make a better measurement of the neutron lifetime.

To perform the measurements, a superconducting 1.1 T deep Ioffe-type trap was built. A cryogenic apparatus housing the magnetic trap and the dilution refrigerator was constructed and successfully operated at NIST Center for Neutron Research in Gaithersburg, MD. The dilution refrigerator is used to cool isotopically purified liquid ^{4}He filling the trapping region to a temperature below 300 mK. Stage-2 potassium intercalated pyrolytic graphite monochromator was built, tested and installed at the end of the NG-6 guide to separate the 0.89 nm neutron beam from a polychromatic cold neutron beam. This installation has increased the number of trapped neutrons compared to the 2002 setup by a factor of 2.5. Many ideas and techniques developed in the course of this work have found applications in other experiments, such as cryogenic neutron EDM search [108] and low energy neutrino and dark matter detection (CLEAN) [109, 110].

Neutron lifetime in the trap with no marginal trapping amelioration is measured to be 620 ± 18 s at helium bath temperature of 300 mK. It is substantially shorter than the currently accepted value of a free neutron lifetime of 885.7 ± 0.8 s. The shorter trap lifetime is attributed to the presence of neutrons with energies higher than the trap depth. These neutrons can leave the trap by colliding with the material walls surrounding the trapping volume. Lowering the magnetic field to 30 % of its maximum value and then raising the field up helps to eliminate the above-threshold neutrons. The trap lifetime in the experimental runs with the field ramping is 833^{+74}_{-63} s. The efficiency of "cleaning" the neutron spectrum by ramping the magnetic field depends on the trap depth. The loss of trapped neutrons during cleaning procedure is as expected.

The measurements indicate an increase in neutron upscattering rate due to the excitations in superfluid helium for the helium bath temperature in $0.85\ \mathrm{K} \geq T \geq 0.5\ \mathrm{K}$ range. The measured rates at low temperatures are in agreement with the theory.

It was observed that the ambient gamma backgrounds are correlated with the signal detected from the trapping region. The monitoring of the ambient backgrounds makes it possible to identify and reject the runs where the external background conditions are changing during the observation period.

The PMT gain shifts in current setup are measured to be on the order of several percent. The gain shifts do not have a significant effect on the estimates of the trap lifetime at a current precision level, but they will become more important when the statistics of the measurement is improved.

6.2 Future Work

The experiment is currently statistics limited. The improvements in statistics can be achieved by both increasing the number of trapped neutrons and by decreasing the backgrounds. If the backgrounds are larger than the signal, which is the case in the current setup, the figure of merit is $Signal^2/Background$.

The number of neutrons in the trap is determined by the trap volume, trap depth, and neutron flux. For a given trap volume and neutron flux, the number of trapped neutrons scales with the trap depth as $B_T^{3/2}$.

In order to increase the trap depth a new magnet assembly is needed. Manufacturing a large high current density quadrupoles is very challenging technically. The bulk of technical expertise in this field is in the high energy physics community, where quadrupole magnets are used as focusing elements for particle accelerators. One of the magnets of this type is currently on loan from KEK, Japan. The magnet has a bore diameter of 14 cm and was tested to create a magnetic field gradient of 70 T/m at operating current of 3400 A. The addition of two solenoids will produce a 3.1 T deep Ioffe-type magnetic trap with a trapping volume of about 4.5 l. As discussed in Section 5.1.2, ramping the field of the 3.1 T deep trap to roughly 0.9 T should eliminate above-threshold neutrons in several seconds.

A new magnetic trap will require a new cryostat. To limit the helium consumption, high-T_c superconducting leads are needed to supply current for the quadrupole.

In addition to increasing the trap depth and volume, one may explore the possibility of increasing the UCN production rate. As shown in Appendix A, the UCN production rate is proportional to the neutron flux spectral density at 0.89 nm. Currently the neutrons produced in the reactor core are delivered to the experiment by a neutron guide. The divergence of 0.89 nm neutrons in NG-6 neutron guide is $\pm 1^\circ$, corresponding to a solid angle of 10^{-3} srad. If the UCN production region is placed closer to the core of the reactor, as for example, in the proposed UCN source for the North Carolina State University reactor, one can gain a factor of 10^4 in solid angle. Calculations show that for this source a UCN production rate on the order of 10^3 UCN cm^{-3}s^{-1} can be achieved [35]. The neutron guides for the Spallation Neutron Source currently under construction in Oak Ridge, TN are using supermirrors, that offer an increase in solid angle by a factor of 10. The statistical estimates for operation of a new magnetic trap at SNS and NCSU are discussed later in this section.

Besides the increase in the number of trapped neutrons, the reduction of backgrounds is another major goal of the next generation design.

Roughly 80 % of the constant background is due to the operation of the reactor. Currently, a 10 cm thick lead housing provides shielding of the apparatus from external gammas. The shielding leaves gaps in the coverage (including the opening directly above the cell, namely the vertical section of the cryostat, see Figure 2.23) that may be eliminated in the next design. More efficient shielding from epithermal neutrons is also needed. Combined, these two measures can decrease the backgrounds due to ambient gammas and neutrons by 40 %. It was observed that the helium scintillation rate is correlated with the ambient backgrounds (see Figure 4.18). Currently the monitoring of the backgrounds is implemented by using a NaI detector mounted roughly 1 m away from the cell. Placing several gamma detectors closer to the cell, possibly inside the apparatus, will make the background monitoring more efficient and will make it possible to correct for the changes in the external backgrounds.

Even if the external backgrounds are not changing, we observe a time-changing background in the cell, most likely due to the activation of the beam stop (see Appendix B). An alternative to the boron oxide beam stop is the acrylic (polymethyl methacrylate, $C_2H_8O_2$) light guide itself. The neutrons would be either captured on hydrogen present in the acrylic or scattered into the boron nitride wall. The neutron penetration length into acrylic is estimated as 3 cm (see Section 2.6) and is larger than the absorption length of < 0.1 mm in the boron oxide. Taking into account that the range of electrons from the aluminum beta decay in acrylic is on the order of 1 cm, we conclude that the requirements for the purity of acrylic are factor of 10^3 stricter than those for boron oxide. However, in one experimental cycle where the boron oxide beam stop was not used[1], we have observed that the time-varying amplitude of the signal was five times lower compared to that in the neutron magnetic trapping runs. Although the detection efficiency during this cycle was 30 % lower due to a different light transport scheme, this result suggests that even regular UVT

---

[1] In these measurements a material bottle made of acrylic coated on the inside with deuterated TPB/polysterene film was placed inside the apparatus.

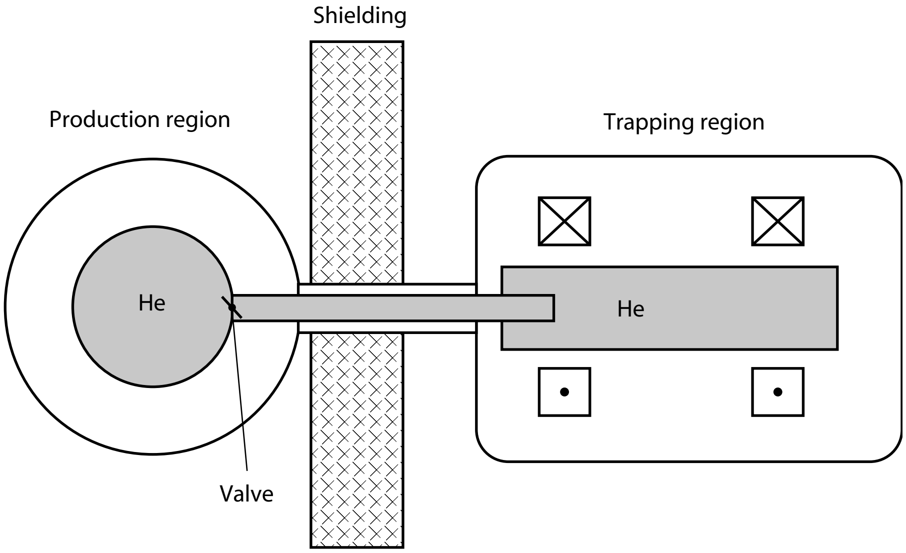

Figure 6.1: Schematic drawing of a setup with a separate production and detection regions [55].

acrylic that was used to manufacture the light guide may be a viable alternative as a material of the beam stop. Even lower levels of impurities should be achievable by selecting a low-impurity grade of acrylic. For example, the concentrations of the radioactive isotopes of Th and U in the acrylic used for SNO experiment are on the order of 1.1 pg/g [111]. An additional benefit from using acrylic as the beam stop is that it can scatter cold neutrons back into the liquid helium region, thus increasing the overall UCN production rate. The size of the effect depends on geometry, but for some configurations an enhancement by a factor of two is possible [112].

The most drastic reduction in time-varying backgrounds can be achieved by separating the UCN production and detection regions [55, 54]. The schematics of this approach is shown in Figure 6.1. The production region, possibly part of the dedicated UCN source located near the thermal column of the reactor [35], is separated from the detection region by heavy gamma shielding. The UCN are produced by superthermal method and are confined by the material walls of the production region. The detection and production regions are connected with a neutron guide that transports UCN from the production region into the detection region. A mechanical or magnetic valve can be installed at the entrance into the guide in order to accumulate neutrons in the production region. Once the valve is opened, the neutrons enter the guide and diffuse towards the trapping region. In order to load the magnetic trap with neutrons, the field of one of the solenoids needs to be lowered (opening the “trap door”). The field of the quadrupole will prevent collisions of the UCN in low-field-seeking spin states with the walls of the detector[2]. After the magnetic field of the solenoid is raised and the valve of the neutron guide is closed, the detection of the neutron decays in the trapping region may start.

Since cold neutrons are not entering the detection region, the activation and luminescence backgrounds are practically eliminated (or at least reduced by the ratio of the neutron fluxes of 10^8). Combined with high UCN fluxed of the new sources, this system has a potential of improving the precision of the measurement dramatically.

The statistical predictions for operating a new trap at different experimental facilities are shown in Table 6.1. As in our present setup, we assume that the background measured in the “background” runs will be subtracted from the “trapping” runs to give the neutron signal. The level of constant background observed in current setup is scaled up by the ratio of the detection region volumes to make an estimate of the expected level of constant background in a new setup at NIST. Also, a conservative

---

[2] In order to maintain the polarization of these neutrons, the walls of the neutron guide and the production region need to be coated with the material that has low collision depolarization rate ($<\sim 10^{-5}$), for example beryllium or diamond-like carbon coating[113]. Also, a weak holding field is necessary to preserve spin orientation.

Table 6.1: Statistical estimates for operating a new 3.1 T deep magnetic trap at different neutron facilities. SNS is the Spallation Neutron Source under construction in Oak Ridge, TN. NCSU is the site of the proposed dedicated UCN source. The number of trapped neutrons takes into account a factor of 2 loss due to the magnetic field ramp.

	NIST	SNS	NCSU
Number of neutrons trapped	4×10^4	1.1×10^6	1.3×10^7
Initial neutron signal amplitude (s^{-1})	20	550	6500
Constant bgnd. amplitude, (s^{-1})	22	4	11
Time-dep. bgnd. amplitude, (s^{-1})	5.5	150	0.1
Statistical error in τ in 40 days, (s)	3.0	0.2	< 0.1
Days to achieve $\epsilon_\tau = 0.5$ %	9.0	< 0.1	< 0.1

20 % reduction in constant backgrounds due to improved shielding is assumed. A factor of 5 gain in constant backgrounds that can be achieved at SNS corresponds to a reactor-off value of backgrounds measured at NIST. These conditions can be achieved if the proposed shielding structure is constructed for the fundamental physics experiments. The time-dependent backgrounds are assumed to be a decaying exponential with a time constant of 400 s, similar to values observed in current setup. The amplitude of the time-dependent backgrounds observed in current setup is scaled up by the ratio of the expected neutron fluxes.

The effects of the PMT gain shifts will become more important for a new setup. In order to make these effects smaller, instead of removing the power from the PMTs during the loading period, one may change the voltage on the first dynode of the PMT so that the operating condition of the rest of the voltage divider network is not changed and also to prevent the photocathode from depletion.

It will be beneficial to install a pulsed light source inside the apparatus, on the detector side of the cell. The light pulses from this source may be synchronized with the DAQ system to distinguish them from the neutron decay pulses. Using the light source not only allows one to measure the changes in the detection efficiency, but also to measure the DAQ dead time. An additional benefit is that the light pulser makes it possible to check quality of optical coupling between the light guide, light splitter, and the PMTs, a feature that was not available in current design.

The improvements in detection efficiency may come from larger solid angle for detecting light from the cell and from locating a photodetector closer to the cell. The most likely candidate for such detector is Multichannel Plate (MCP) based PMT[3]. These devices can operate in magnetic fields up to 1 T. The anode of the MCP-based PMT may be sectioned, so the coincidence techniques may be implemented without the need for the light splitter. The major concern is the structural stability of the PMT envelope during the cooldown. Using MCP PMT will allow us to avoid using a 77 K light guide and thus not only to decrease the light losses, but also to reduce backgrounds and to decrease the liquid helium boil-off.

The other detector options include solid-state devices such as Avalanche Photodiodes (APD) and Visible Light Photon Counters (VLPC). They have higher detection efficiency but their noise characteristics and, especially, small size (typically 1 cm^2) limit their use for detecting the light emerging from the large diameter cell [114].

The design of a new magnetic trap and a cryostat is currently underway. An increase in the number of trapped neutrons and better control of the backgrounds should make it possible to perform at NIST a measurement of the neutron lifetime with the uncertainty of several seconds. The operation of this trap at new UCN facilities that are being developed will lead to an improvement in the neutron lifetime measurement by an order of magnitude.

---

[3] The prototype of this PMT is developed by Burle Industries.

Bibliography

[1] J. Chadwick. Possible existence of a neutron. *Nature* **129**, 312 (1932).

[2] H. Abele and D. Mund, editors. *Proceedings of the workshop "Quark-Mixing, CKM-Unitarity"*. Heidelberg, Germany, 2002.

[3] R E. Lopez and M S. Turner. Precision prediction for the big-bang abundance of primordial 4he. *Phys. Rev. D* **59**, 103502/14 (1999).

[4] I. B. Khriplovich and S. K. Lamoreaux. *CP Violation Without Strangeness.* Springer-Verlag, Berlin Heidelberg, 1997.

[5] L. J. Lising, S. R. Hwang, J. M. Adams, T. J. Bowles, M. C. Browne, T. E. Chupp, K. P. Coulter, M. S. Dewey, S. J. Freedman, B. K. Fujikawa, A. Garcia, G. L. Greene, G. L. Jones, H. P. Mumm, J. S. Nico, J. M. Richardson, R. G. H. Robertson, T. D. Steiger, W. A. Teasdale, A. K. Thompson, E. G. Wasserman, F. E. Wietfeldt, R. C. Welsh, and J. F. Wilkerson. New limit on the d coefficient in polarized neutron decay. *Phys. Rev. C* **62**, 055501/11 (2004).

[6] T. Soldner, L. Beck, C. Plonka, K. Schreckenbach, and O. Zimmer. New limit on t violation in free neutron decay. *Nucl. Phys. A* **721**, 469–472 (2003).

[7] M. Baldo-Ceolin et al. A new experimental limit on neutron — anti-neutron oscillations. *Z. Phys.* **C64**, 409–416 (1994).

[8] K. Hagiwara et al. Review of Particle Physics. *Phys. Rev. D* **66**, 010001+ (2002).

[9] K. Grotz and H. V. Klapdor. *The Weak Interaction in Nuclear, Particle and Astrophysics.* 2nd edition. Adam Hilger, Bristol, Philadelphia and New York, 1990.

[10] D. Dubbers. Particle physics with cold neutrons. *Progress in Particle and Nuclear Physics* **26**, 173–252 (1991).

[11] J. D. Jackson, M. Treiman, and H. W. Wyld Jr. New limit on the d coefficient in polarized neutron decay. *Nucl. Phys.* **4**, 206 (1957).

[12] I. S. Towner and J. C. Hardy. Calculated corrections to superallowed fermi decay: New evaluation of the nuclear-structure-dependent terms. *Phys. Rev. C* **66**, 035501/13 (2002).

[13] I. S. Towner and J. C. Hardy. The evaluation of v_{ud}, experiment and theory. *J. Phys. G* **29**, 197–211 (2003).

[14] D. Wilkinson. Fundamental interactions and nuclear structure: an impressionistic overview. *Nucl. Phys. A* **A374**, 649–664 (1982).

[15] H. Abele, M. Astruc Hoffmann, S. Baeßler, D. Dubbers, F. Glück, U. Müller, V. Nesvizhevsky, J. Reich, and O. Zimmer. Is the unitarity of the quark-mixing ckm matrix violated in neutron β-decay? *Phys. Rev. Lett.* **88**, 211801 (2002).

[16] V. Cirigliano, M. Knecht, H. Neufeld, and H. Pichl. The pionic beta decay in chiral perturbation theory. *Eur. Phys. J. C* **27**, 255–262 (2003).

[17] D. Počanić, E. Frlež, V. A. Baranov, W. Bertl, C. Bröennimann, M. Bychkov, J. F. Crawford, M. Daum, N. V. Khomutov, A. S. Korenchenko, S. M. Korenchenko, T. Kozlowski, N. P. Kravchuk, N. A. Kuchinsky, W. Li, R. C. Minehart, D. Mzhavia, B. G. Ritchie, S. Ritt, A. M. Rozhdestvensky, V. V. Sidorkin, L. C. Smith, I. Supek, Z. Tsamalaidze, B. A. VanDevender, Y. Wang, H.-P. Wirtz, and K. O. H. Ziock. Precise measurement of the $\pi^+ \to \pi^0 e^+ \nu$ branching ratio. *hep-ex/0312030* (2003).

[18] V. Cirigliano, H. Neufeld, and H. Pichl. k_{e3} decays and ckm unitarity. *hep-ph/0401173* (2004).

[19] A. Sher et al. New, high statistics measurement of the $k^+ \to \pi^0 e^+ \nu$ (k^+_{e3}) branching ratio. *hep-ex/0305042* (2003).

[20] K. A. Olive, G. Steigman, and T. P. Walker. Primordial nucleosynthesis: theory and observations. *Phys. Rep.* **333–334**, 389–407 (2000).

[21] D. Kirkman, D. Tytler, N. Suzuki, J. M. O'Meara, and D. Lubin. The cosmological baryon density from the deuterium to hydrogen ratio towards qso absorption systems: D/h towards q1243+3047. *Astrophys. J. Suppl.* **149**, 1 (2003).

[22] M. Pettini and D. V. Bowen. A new measurement of the primordial abundance of deuterium: Toward convergence with the baryon density from the cosmic microwave background? *Astrophys. J.* **560**, 41–48 (2003).

[23] D. N. Spergel, L. Verde, H. V. Peirisa, E. Komatsu, M. R. Nolta, C. L. Bennett, M. Halpern, G. Hinshaw, N. Jarosik, A. Kogut, M. Limon S. S., Meyer,

L. Page, G. S. Tucker, J. L. Weiland, E. Wollack, and E. L. Wright. First-year wilkinson microwave anisotropy probe (wmap) observations: Determination of cosmological parameters. *Astrophys. J. Suppl.* **148**, 175 (2003).

[24] G. Huey, R. H. Cyburt, and B. D. Wandelt. Precision primordial ^{4}he measurement with cmb experiments. *astro-ph/0307080* (2003).

[25] Y. I. Izotov, F. H. Chaffee, C. B. Foltz, R. F. Green, N. G. Guseva, and T. X. Thuan. Helium abundance in the most metal-deficient blue compact galaxies: I zw 18 and sbs 0335-052. *Astrophys. J.* **527**, 757 (1999).

[26] V. Luridiana, A. Peimbert, M. Peimbert, and M. Cervi no. The effect of collisional enhancement of balmer lines on the determination of the primordial helium abundance. *Astrophys. J.* **592**, 846–865 (2003).

[27] K. .A. Olive and E. D. Skillman. On the determination of the he abundance in extragalactic $\mathrm{H_{II}}$ regions. *New Astronomy* **6**, 119–150 (2001).

[28] J. A. Tauber. The planck mission. In *The Extragalactic Infrared Background and its Cosmological Implications,* M. Harwit and M. Hauser, editors, Volume 204 of *IAU Symposium*, 2000.

[29] V. K. Ignatovich. *The physics of Ultracold Neutrons*, Volume 5 of *Oxford series on neutron scattering in condensed matter.* Oxford University Press, 1990.

[30] R. Golub, D. Richardson, and S. K. Lamoreaux. *Ultra-Cold Neutrons.* Adam Hilger, 1991.

[31] Yu. B. Zeldovich. *Sov Phys JETP* **9**, 1389 (1959).

[32] A. Saunders et al. Demonstration of a solid deuterium source of ultra-cold neutrons. *nucl-ex/0312021* (2003).

[33] B. W. Wehring and A. R. Young. Ultracold neutron source at the north carolina state research reactor. *Tech. Phys. Lett.* **84**, 120–121 (2000).

[34] Y. Masuda, T. Kitagaki, K. Hatanaka, M. Higuchi, S. Ishimoto, Y. Kiyanagi, K. Morimoto, S. Muto, and M. Yoshimura. Spallation ultracold-neutron production in superfluid helium. *Phys. Rev. Lett.* **89**, 284801 (2002).

[35] E. Korobkina, R. Golub, B. W. Wehring, and A. R. Young. Production of ucn by downscattering in superfluid ^{4}He. *Phys. Lett. A* **301**, 462–469 (2002).

[36] M. S. Dewey, D. M. Gilliam, J. S. Nico, F. E. Wietfeldt, X. Fei, W. M. Snow, G. L. Greene, J. Pauwels, R. Eykens, A. Lamberty, and J. Van Gestel. Measurement of the neutron lifetime using a proton trap. *Phys. Rev. Lett.* **91**, 152302/1–4 (2003).

[37] Z. Chowdhuri, G. L. Hansen, V. Jane, C. D. Keith, W. M. Lozowski, W. M. Snow, M. S. Dewey, D. M. Gilliam, G. L. Greene, J. S. Nico, A. K. Thompson, and F. E. Wietfeldt. A cryogenic radiometer for absolute neutron rate measurement. *Rev. Sci. Inst.* **74**, 4280–4293 (2003).

[38] W. Mampe, P. Ageron, C. Bates, J. M. Pendlebury, and A. Steyerl. Neutron lifetime measured with stored ultracold neutrons. *Phys. Rev. Lett.* **63**, 593–596 (1989).

[39] A. Pichlmaier, J. Butterworth, P. Geltenbort, H. Nagel, V. Nesvizhevsky, S. Neumaier, K. Schreckenbach, E. Steichele, and V. Varlamov. Mambo ii: neutron lifetime measurement with storage of ultra cold neutrons. *Nucl. Instr. Meth. A* **440**, 517–521 (2000).

[40] V. V. Nesvizhevskii, A. P. Serebrov, R. R. Tal'daev, A. G. Kharitonov, V. P. Alfimenkov, A. V. Strelkov, and V. N Shvetsov. Measurement of the neutron lifetime in a gravitational trap and analysis of experimental errors. *Sov. Phys. JETP* **75**, 405–412 (1992).

[41] S. Arzumanov, L. Bondarenko, S. Chernyavsky, W. Drexel, A. Fomin, P. Geltenbort, V. Morozov, Yu. Panin, J. Pendlebury, and K. Schreckenbach. Neutron life time value measured by storing ultracold neutrons with detection of inelastically scattered neutrons. *Phys. Lett. B* **483**, 15–22 (2000).

[42] V. V. Vladimirskiĭ. Magnetic mirrors, channels and bottles for cold neutrons. *Sov Phys JETP* **12**, 740–746 (1961).

[43] Yu. G. Abov, S. P. Borovlev, V. V. Vasil'ev, V. V. Vladimirskii, and E. N. Mospan. Measurement of the time of storage of ultracold neutrons in a magnetic trap. *Sov. J. Nucl. Phys.* **38**, 122–128 (1960).

[44] N. Niehues. *Untersuchungen an einer magnetischen flasche zur speicherung von neutronen.* PhD thesis, Friedrich Wilhelm University of Bonn, 1983.

[45] K.-J. Kügler, K. Moritz, W. Paul, and U. Trinks. Nestor a magnetic storage ring for slow neutrons. *Nucl. Instr. Meth. A* **228**, 240–258 (1985).

[46] P. R. Huffman, C. R. Brome, J. S. Butterworth, K. J. Coakley, M. S. Dewey, S. N. Dzhosyuk, R. Golub, G. L. Greene, K. Habicht, S. K. Lamoreaux, C. E. H. Mattoni, D. N. McKinsey, F. E. Wietfeldt, and J. M. Doyle. Magnetic trapping of neutrons. *Nature* **403**, 62–64 (2000).

[47] F. Anton, W. Paul, W. Mampe, L. Paul, and S. Paul. Measurement of the neutron lifetime by magnetic storage of free neutrons. *Nucl. Instr. Meth. A* **284**, 101–107 (1989).

[48] C. R. Brome, J. S. Butterworth, S. N Dzhosyuk, C. E. H. Mattoni, D. N. McKinsey, J. M. Doyle, P. R. Huffman, M. S. Dewey, F. E. Wietfeldt, R. Golub, K. Habicht, G. L. Greene, S. K. Lamoreaux, and K. J. Coakley. Magnetic trapping of ultracold neutrons. *Phys. Rev. C* **63**, 055502 (2001).

[49] V. F. Ezhov, B. A. Bazarov, P. Geltenbort, N. A. Kovrizhnykh, G. B. Krygin, V. L. Ryabov, and A. P. Serebrov. Permanent-magnet trap for ultracold neutron storage. *Tech. Phys. Lett.* **27**, 64–70 (2001).

[50] O. Zimmer. A method of magnetic storage of ultra-cold neutrons for a precise measurement of the neutron lifetime. *J. Phys. G.* **26**, 67–77 (2000).

[51] I. Altarev, A. Frei, F. J. Hartmann, S. Paul, G. Petzoldt, R. Picker, W. Schott, D. Tortorella, U. Trinks, and O. Zimmer. A magnetic trap for neutron-lifetime measurements. In *Proceedings of the workshop "Quark-Mixing, CKM-Unitarity",* H. Abele and D. Mund, editors, 91–96. Heidelberg, Germany, 2002.

[52] J. M. Doyle and S. K. Lamoreaux. On measuring the neutron beta-decay lifetime using ultracold neutrons produced and stored in a superfluid-^{4}he-filled magnetic trap. *Europhys. Lett.* **26**, 253–258 (1994).

[53] C. R. Brome. *Magnetic Trapping of Ultracold Neutrons.* PhD thesis, Harvard University, 2000.

[54] C. E. H. Mattoni. *Magnetic trapping of ultracold neutrons produced from a monochromatic cold neutron beam.* PhD thesis, Harvard University, 2002.

[55] D. N. McKinsey. *Detecting magnetically trapped neutrons: Liquid helium as a scintillator.* PhD thesis, Harvard University, 2002.

[56] L. Landau. Theory of the superfluidity of helium ii. *Phys. Rev.* **60**, 356–358 (1941).

[57] R. Golub and J. M. Pendlebury. Super-thermal sources of ultra-cold neutrons. *Phys. Lett.* **53A**, 133–135 (1975).

[58] R. Golub. On the storage of neutrons in superfluid ^{4}he. *Phys. Lett.* **72A**, 387–390 (1979).

[59] R. Golub, C. Jewell, P. Ageron, W. Mampe, B. Heckel, and I. Kilvington. Operation of a superthermal ultracold neutron source and the storage of ultracold neutrons in superfluid helium-4. *Z. Phys. B* **51**, 187–193 (1983).

[60] P. Ageron, W. Mampe, R. Golub, and J. M. Pendlebury. Measurement of the ultra cold neutron production rate in an external liquid helium source. *Phys. Lett. A* **66A**, 469–471 (1978).

[61] H. Yoshiki, K. Sakai, M. Ogura, T. Kawai, Y. Masuda, T. Nakajima, T. Takayama, S. Tanaka, and A. Yamaguchi. Observation of ultracold-neutron production by 9 åcold neutrons in superfluid helium. *Phys. Rev. Lett.* **68**, 1323–1326 (1992).

[62] C. A. Baker, S. N. Balashov, J. Butterworth, P. Geltenbort, K. Green, P. G. Harris, M. G. D. van der Grinten, P. S. Iaydjiev, S. N. Ivanov, J. M. Pendlebury, D. B. Shiers, M. A. H. Tucker, and H. Yoshiki. Experimental measurement of ultracold neutron production in superfluid ^{4}he. *Phys. Lett. A* **308**, 67–74 (2003).

[63] H. S. Sommers Jr., J. G. Dash, and L. Goldstein. Transmission of slow neutrons by liquid helium. *Phys. Rev.* **97**, 855–862 (1955).

[64] R. Pardo. Personal communication. 2003.

[65] P. C. Hendry and P. V. E. McClintock. Continuous flow apparatus for preparing isotopically pure ^{4}He. *Cryogenics* **27**, 131–138 (1987).

[66] R. L.Cappelletti, C. J.Glinka, S. Krueger, R. A. Lindstrom, J. W. Lynn, H. A. Prask, E. Prince, J. J. Rush, J. M. Rowe, S. K. Satija, B. H. Toby, A. Tsai, and T. J. Udovic. Materials research with neutrons at nist. *Journal of Research of the National Institute of Standards and Technology* **106**(1), 187–230 (2001).

[67] R. E. Williams and J. M. Rowe. Developments in neutron beam devices and an advanced cold source for the nist research reactor. *Physica B* **311**, 117–122 (2002).

[68] C. E. H. Mattoni, C. P. Adams, K. J. Alvine, J. M. Doyle, S. N. Dzhosyuk, R. Golub, E. Korobkina D. N. McKinsey A. K. Thompson, L. Yang, H. Zabel, and P. R. Huffman. A long wavelength neutron monochromator for superthermal production of ultracold neutrons. *Physica B* **344**, 343–357 (2004).

[69] M. E. Misenheimer and H. Zabel. Stage transformation and staging disorder in graphite intercalation compounds. *Phys. Rev. Lett.* **54**, 2521–2524 (1985).

[70] R. Stedman. *Rev. Sci. Inst.* **31**, 1156 (1956).

[71] D. N. Batchelder and R. O. Simmons. Lattice constants and thermal expansivities of silicon and of calcium fluoride between 6 and 322 k. *Journal of Chemical Physics* **41**, 2324–2329 (1964).

[72] P. Trucano and R. Chen. Structure of graphite by neutron diffraction. *Nature* **258**, 136–137 (1975).

[73] P. A. Egelstaff and R. S. Pease. *Journal of Scientific Instruments* **31**, 207 (1954).

[74] Weston, Young, Poenitz, and Lubitz. Endf/b-vi. *http://www-nds.iaea.or.at/* .

[75] S. Gov, S. Shtrikman, and H. Thomas. Magnetic trapping of neutral particles: Classical and quantum-mechanical study of a ioffe-pritchard type trap. *J. App. Phys.* **87**, 3989–3998 (2000).

[76] O. V. Lounasmaa. *Experimental principles and methods below 1 K.* Academic Press, 1974.

[77] F. Pobell. *Matter and Methods at Low Temperatures.* 2nd edition. Springer-Verlag, Berlin, 1996.

[78] J. S. Butterworth, C. R.Brome, P. R. Huffman, C. E. H. Mattoni, D. N. McKinsey, and J. M. Doyle. A removable cryogenic window for transmission of light and neutrons. *Rev. Sci. Inst.* **69**, 3998 (1998).

[79] P. R. Huffman, C. R. Brome, J. S. Butterworth, S. N. Dzhosyuk, R. Golub, S. K. Lamoreaux, C. E. H. Mattoni, D. N. McKinsey, and J. M. Doyle. Magnetically stabilized luminescent excitations in hexagonal boron nitride. *J. Lumin.* **92**, 291–296 (2001).

[80] J. Wilks. *The Properties of Liquid and Solid Helium.* Oxford Press, London, 1967.

[81] D. N. McKinsey, C. R.Brome, S. N. Dzhosyuk, R. Golub, K. Habicht, P. R. Huffman, E. Korobkina, S. K. Lamoreaux, C. E. H. Mattoni, A. K. Thompson, L. Yang, and J. M. Doyle. Time dependence of liquid-helium fluorescence. *Phys. Rev. A* **67**, 62716 (2003).

[82] A. V. Benderskii, R. Zadoyan, N. Schwentner, and V. A. Apkarian. Photodynamics in superfluid helium: Femtosecond laser-induced ionization, charge recombination, and preparation of molecular rydberg states. *J. Chem. Phys.* **110**, 1542–15557 (1998).

[83] D. N. McKinsey, C. R.Brome, J. S. Butterworth, S. N. Dzhosyuk, P. R. Huffman, C. E. H. Mattoni, J. M. Doyle, R. Golub, and K. Habicht. Radiative decay of the metastable $\mathrm{He}_2(a^3\sigma_u^+)$ molecule in liquid helium. *Phys. Rev. A* **59**, 200–204 (1999).

[84] J. S. Adams, Y. H. Kim, R. E. Lanou, H. J. Maris, and G. M. Seidel. Scintillation and quantum evaporation generated by single monoenergetic electrons stopped in superfluid helium. *J. Low Temp. Phys.* **113**, 1121–1128 (1998).

[85] D. N. McKinsey, C. R.Brome, J. S. Butterworth, R. Golub, K. Habicht, P. R. Huffman, S. K. Lamoreaux, C. E. H. Mattoni, and J. M. Doyle. Fluorescence

efficiencies of thin scintillating films in the extreme ultraviolet spectral region. *Nucl. Instr. Meth. B* **132**, 351 (1997).

[86] D. N. McKinsey, C. R.Brome, J. S. Butterworth, S. N. Dzhosyuk, R. Golub, K. Habicht, P. R. Huffman, C. E. H. Mattoni, L. Yang, and J. M. Doyle. Detecting ionizing radiation in liquid helium using wavelength shifting light collection. *Nucl. Instr. Meth. A* **516**, 475–485 (2004).

[87] W. M. Burton and B. A. Powell. Fluorescence of tetraphenyl-butadiene in the vacuum ultraviolet. *App. Opt.* **12**, 87–89 (1973).

[88] Burle Technologies. *Photomultiplier Handbook*. 1980.

[89] Burle Technologies. Burle 8854 specification sheet.

[90] S. N. Dzhosyuk, C. E. H. Mattoni, D. N. McKinsey, A. K. Thompson, L. Yang, J. M. Doyle, and P. R. Huffman. Neutron-induced luminescence and activation in neutron shielding and scintillation detection materials at cryogenic temperatures. *Nucl. Instr. Meth. B* **217**, 457–470 (2004).

[91] M. L. G. Leite, L. Maia, A. C. M. Rodrigues, and E. D. Zanotto. Vitreous materials laboratory, federal university of sao carlos. Personal communication.

[92] J. R. Parrington, H. D. Knox, S. L. Breneman, E. M. Baum, and F. Feiner. *Nuclides and Isotopes: Chart of the Nuclides*. General Electric Co. and KAPL, Inc., 1996.

[93] M. H. Schleier-Smith, L. D. van Buuren, J. M. Doyle, S. N. Dzhosyuk, D. M. Gilliam, C. E.'H. Mattoni, D. N. McKinsey, L. Yang, and P. R. Huffman. The production of nitrogen-13 by neutron capture in boron compounds. *Nucl. Instr. Meth. B* **215**, 531–536 (2004).

[94] J. Blachot. Nuclear data sheets for a = 113. *Nuclear Data Sheets* **83**, 647–788 (1998).

[95] F. S. Porter, S. R. Bandler, C. Enss, R. E. Lanou, H. J. Maris, T T. More, and G. M. Seidel. A stepper motor for use at temperatures down to 20 mk. *Physica B* **194–196**, 151–152 (1994).

[96] B. E. Berger, F. S. Bieser, D. A. Dwyer, S. J. Freedman, B. K. Fujikawa, K. M. Heeger, K. T. Lesko, K. B. Luk, T. Stezelberger, T. Walker, , and L. A. Winslow for the KamLAND Collaboration. Kamland front-end electronics. Technical report, LBNL Nuclear Science Division Annual Report, 2002. LBNL-52643.

[97] G. L. Yang and K. J. Coakley. Likelihood models for two-stage neutron lifetime experiments. *Phys. Rev. C* **63**, 014602/1–16 (2001).

[98] K. J. Coakley. Statistical planning for a neutron lifetime experiment using magnetically trapped neutrons. *Nucl. Instr. Meth. A* **406**, 451–463 (1998).

[99] K. J. Coakley and G. L. Yang. Estimation of the neutron lifetime: Comparison of methods which account for background. *Phys. Rev. C* **65**, 064612/1–7 (2002).

[100] M. Yamashhita. Anomalous gain changes in photomultiplier tubes for use in scintillation counting. *Rev. Sci. Inst.* **49**, 499–502 (1978).

[101] Y. K. Wu, E. Forest, and D. S. Robin. Explicit symplectic integrator for s-dependent static magnetic field. *Phys. Rev. E* **68**, 46502/9 (2003).

[102] K. J. Coakley. Personal communication., 2004.

[103] S. K. Lamoreaux. Note of the effect of lowering the trap potential to throw out maginally trapped neutrons. 1995.

[104] L. D. Landau and E. M. Lifshitz. *Mechanics.* 3rd edition. Butterworth-Heinemann Ltd, 1976.

[105] E. L. Surkov, J. T. M. Walraven, and G. V. Shlyapnikov. Collisionless motion of neutronparticles in magnetostatic traps. *Phys. Rev. A* **49**, 4478–4486 (1994).

[106] L. D. Landau and E. M. Lifshitz. *Quantum mechanics: non-relativistic theory.* 3rd edition. Butterworth-Heinemann Ltd, 1991.

[107] P. V. E. McClintock. An apparatus for preparing isotopically pure ^{4}He. *Cryogenics* **18**, 201–208 (1978).

[108] R. Golub and S. K. Lamoreaux. Neutron electric-dipole moment, ultracold neutrons and polarized ^{3}he. *Physics Reports* **237**, 1 (1994).

[109] D. N. McKinsey and J. M. Doyle. Liquid helium and liquid neon-sensitive, low background scintillation media for the detection of low energy neutrinos. *J. Low Temp. Phys.* **118**, 153–165 (2000).

[110] C. J. Horowitz, K. J. Coakley, and D. N. McKinsey. Supernova observation via neutrino-nucleus elastic scattering in the clean detector. *Phys. Rev. D* **68**, 23005/7 (2003).

[111] The SNO Collaboration. The sudbury neutrino observatory. *Nucl. Instr. Meth. A* **449**, 172–207 (2000).

[112] P. D. Bangert, M. D. Cooper, and S. K. Lamoreaux. Enhancement of superthermal ultracold neutron production by trapping cold neutrons. *Nucl. Instr. Meth. A* **410**, 264–272 (1998).

[113] M. G. D. van der Grinten, J. M. Pendlebury, D. Shiers C. A. Baker, K. Green, P. G. Harris, P. S. Iaydjiev, S. N. Ivanov, and P. Geltenbort. Characterization and development of diamond-like carbon coatings for storing ultracold neutrons. *Nucl. Instr. Meth. A* **423**, 421–427 (1999).

[114] L. Yang, S. N. Dzhosyuk, J. M. Gabrielse, C. E. H. Mattoni, S. E. Maxwell, D. N. McKinsey, and J. M. Doyle. Performance of a large-area avalanche photodiode at low temperature for scintillation detection. *Nucl. Instr. Meth. A* **508**, 388–393 (2003).

[115] M. Cohen and R. P. Feynman. Theory of inelastic scattering of cold neutrons from liquid helium. *Phys. Rev.* **107**, 13–24 (1957).

[116] A.-J. Dianoux and G. Lander, editors. *Neutron Data Booklet.* Institut Laue-Langevin, 2002.

Appendix A

Superthermal UCN Production

The UCN are produced in liquid helium bath as a result of scattering of a cold neutron beam. We will derive general expressions for the UCN production rate and make estimates for the expected number of trapped neutrons in our magnetic trap. In this derivation we will follow approach of Ref. [35].

Consider a neutron with initial momentum $\hbar\vec{k}_i$ scattering in superfluid helium to a final momentum $\hbar\vec{k}_f$. The energy of the neutron is given by $E_{i,f} = \hbar\omega_{i,f} = (\hbar k_{i,f})^2/2m$, where m is the neutron mass. Scattering event produces excitations in the helium with the momentum $\hbar\vec{q}$ and energy $\hbar\omega$ given by the momentum and energy conservation laws:

$$\begin{aligned} \hbar\vec{q} &= \hbar(\vec{k}_i - \vec{k}_f), && \text{(A.1)} \\ \hbar\omega &= \hbar^2(k_i^2 - k_f^2)/2m. && \text{(A.2)} \end{aligned}$$

These equations, together with the helium excitations dispersion curve $\omega(q)$ set the kinematics of the UCN production. Following Ref. [115] we can write in Born approximation a differential cross section for scattering into an element of solid angle $d\Omega$ as:

$$\frac{d\sigma}{d\omega} = a^2 \frac{k_f}{k_i} S(q,\omega) d\Omega, \tag{A.3}$$

where a is a neutron-helium scattering length and $S(q,\omega)$ is a structure factor.

Integration over azimuthal angle gives $d\Omega = 2\pi \sin\theta \, d\theta$, where θ is an angle between $\vec{k}_f$ and $\vec{k}_f$. Taking a square of Equation (A.1) we get,

$$q^2 = k_i^2 + k_f^2 - 2k_i k_f \cos\theta,$$

that, after differentiating with fixed k_i and k_f, gives

$$\sin\theta \, d\theta = \frac{q \, dq}{k_i k_f},$$

and Equation (A.3) can be written as

$$\frac{d\sigma}{d\omega} = 2\pi a^2 S(q,\omega) \, \frac{k_i \, dq}{k_i^2}.$$

For the produced UCN $k_f \ll k_i$ and it follows from Equation (A.1) that $q \sim k_i$ and $k_i - k_f < q < k_f + k_i$. Introducing $k_u \equiv k_f$ we get:

$$\frac{d\sigma}{d\omega} = 4\pi a^2 S(k_i, \omega_i) \frac{k_u}{k_i}.$$

Let $\Phi(E)$ be the incoming neutron beam energy spectrum. Then the production rate of the UCN with energy E_u is

$$\begin{aligned} P(E_u) dE_u &= \int \frac{d\Phi}{dE}\Big|_{E_i} N \frac{d\sigma}{d\omega}\Big(E_i \to E_u\Big) dE_i dE_u = \qquad (A.4) \\ &= 4\pi a^2 N \int \frac{d\Phi}{dE}\Big|_{E_i} S(k_i,\omega_i) \frac{k_u}{k_i} dE_i dE_u \qquad (A.5) \end{aligned}$$

If maximum energy of the UCN that can be stored in the trap is $E_c = \hbar^2 k_c^2/2m$, than the total UCN production rate is

$$P(E_c) = \int_0^{E_c} P(E_u) dE_u = 4\pi a^2 N \frac{\hbar^4}{m^2} \frac{k_c^3}{3} \int \frac{d\Phi}{dE}\Big|_{E_i} S(k_i, \omega_i) dk_i. \tag{A.6}$$

Here a factor of $\hbar^4/m^2$ appears due to the change of the integration variables from E_i and E_u to k_i and k_u.

For UCN production in the linear radial potential of the trap $E_c(r) = E_T(1-r/R)$, where R is the diameter of the trap defined by the material wall. Than the production rate inside the magnetic trap is

$$P_M(E_T) = \frac{1}{\pi R^2} \int_0^R P(E_c(r)) 2\pi r dr = 2P(E_T) \int_0^1 (1-y)^{3/2} y dy = \frac{8}{35} P(E_T), \tag{A.7}$$

where we also make an assumption that the neutron flux density is constant in the beam ($\Phi(\vec{r}, E) = \Phi(E)$).

In a case of a magnetic trap with additional material walls that create a potential V at $r = R$, the production rate is

$$\begin{aligned} P_M(E_T, V) &= \frac{1}{\pi R^2} \int_0^R P(E_c(r) + V) 2\pi r dr = 2P(E_T) \int_0^1 (1 - y + \frac{V}{E_T})^{3/2} y dy = \\ &= P_M(E_T)\Big((1+f)^{7/2} - f^{5/2}\Big(\frac{7}{2} + f\Big)\Big), \end{aligned}$$

where $f = V/E_T \approx 22/66 = 1/3$. Then $P_M(E_T, V) \approx 2.5 P_M(E_T)$.

The one-phonon production rate is obtained by taking integral in Equation (A.6) over the one phonon peak, giving

$$\int_{P_1} \frac{d\Phi}{dE}\Big|_{E_i} S(k_i, \omega_i) dk_i \approx \frac{m}{\hbar^2} \frac{1}{k^*} \frac{d\Phi}{dE}\Big|_{E^*} \int_{P_1} S(k_i, \omega_i) d\omega_i = \frac{m}{\hbar^2} \frac{1}{k^*} \frac{d\Phi}{dE}\Big|_{E^*} \beta S^*, \tag{A.8}$$

where $k^* = 0.71$ Å^{-1} corresponds to the intersection point between spectrum of elementary excitations in the helium and spectrum of a free neutron (see Figure 1.6),

$\beta = v_n^*/(v_n^* - c^*) = 1.45$ is a numerical coefficient that takes into account the fact that curves in Figure 1.6 cross at an angle [30, 35] (v_n^* is the neutron velocity corresponding to k^*, c^* is the group velocity on the phonons at the same point), $S^* = 0.12$ [35].

Using Equations (A.6) to (A.8) and the expression for the trap depth $E_T = \mu_n B_T$ we get

$$P_M(B_T) = (1.3 \times 10^{-10})(B_T)^{3/2} \frac{d\Phi}{dE}\bigg|_{E^*} \ (\mathrm{cm}^{-3}\,\mathrm{s}^{-1}),$$

where $d\Phi/dE$ is in units of $(\mathrm{cm}^{-2}\,\mathrm{s}^{-1}\,\mathrm{meV}^{-1})$ and we have used $N = 2.17 \times 10^{22}\ \mathrm{cm}^{-3}$, $a = 3.3$ fm. Since only one spin-state of the UCN gets trapped, the production rate takes into account a factor of 1/2.

The width of a region that contributes to the one-phonon production is determined by k_u and is given by $\Delta k = \pm 0.0054\sqrt{B_T}\ \text{Å}^{-1}$.

As we can see, the production rate depends on the trap depth as $B_T^{3/2}$.

Monte-Carlo simulations are developed in order to estimate the production rates at the location of the apparatus [54]. The simulations take into account the divergence of the neutron beam, reflections from the potassium GIC monochromator, air scatter. The neutron path is traced from the exit of the neutron guide to the trapping region. The predicted UCN production rate in the trap is $6.8 \pm 1.4\ \mathrm{UCN\,s^{-1}}$. A detailed description of the simulations can be found in Ref. [54].

Following Ref. [35], we can estimate the multi-phonon production by performing an integration in the equation (A.6) using values of S from Ref. [35] and the experimentally determined neutron spectrum of NG-6 guide [53, 54]. The neutron beam spectrum of the NG-6 is shown in Figure A.1. Also shown are the values of structure factor S [35] and the spectrum of the neutron beam reflected by the potassium GIC

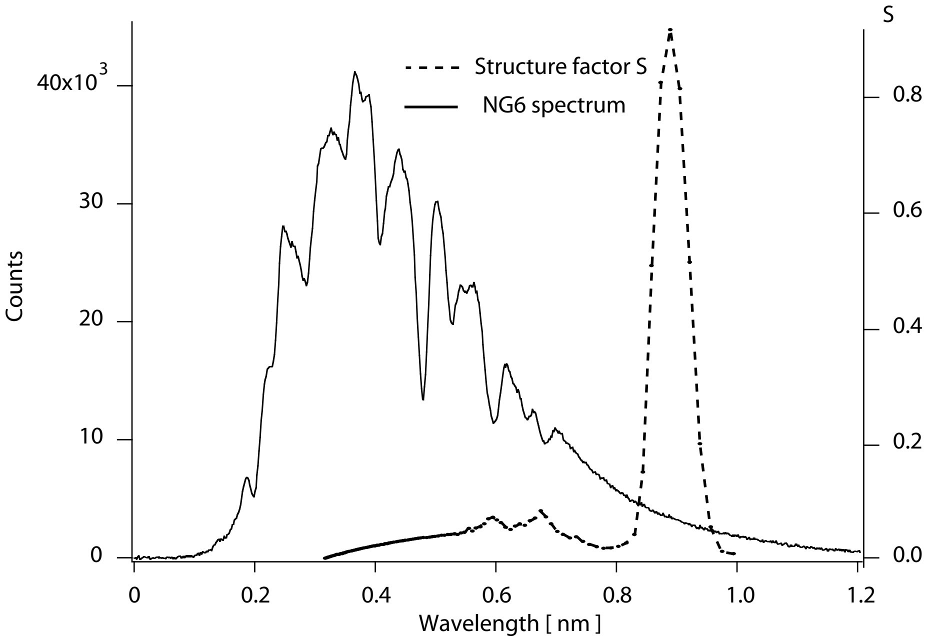

Figure A.1: Spectrum of the neutron beam delivered by NIST NG-6 guide [54]. Also shown are the values of structure factor S from Ref. [35].

monochromator (NG6U). The numerical integration shows that the neutron production rate is higher by a factor of 2.2 in the polychromatic NG6 beam. The loss in UCN production rate at NG6U is compensated by the reduction in neutron-induced backgrounds and by creation of a separate neutron beam line.

Appendix B

Beam Stop Activation

The certificate of analysis supplied by the manufacturer of the boron trioxide that is used as a material of the neutron beam stop inside the cell indicates the amount of impurities that are present in this material, see Table B.1. The quoted density of the material is $\rho = 2.46\,\mathrm{g\,cm^{-3}}$. The boron number density can be estimated as $n_B = 2\rho N_A / A_{B_2O_3} \approx 4.2 \times 10^{22}\,\mathrm{g\,cm^{-3}}$.

Using the thermal neutron absorbtion cross section for natural Boron of $\sigma_{B,th} = 767$ bn [116] (cross section for 0.89 nm neutrons is then $\sigma_B = 3800$ bn), the mean free path of the 0.89 nm neutron in the beam stop can be calculated as $\lambda_{abs} = 1/(\sigma_B n_B) \approx 63\,\mu\mathrm{m}$.

Roughly $\Phi \approx 10^8$ neutrons enter the cell per second during the trap loading. The majority of the neutrons (99 %) are absorbed by the beam stop. Among the materials listed in Table B.1, the strongest activation is due to Aluminum. The number of decays at the end of the loading period is $\dot{N}_{Al} = \Phi \tau_{Al} \frac{\rho x N_A}{A_{Al}} \sigma \lambda_{abs} \approx 5.8\ \mathrm{s}^{-1}$, where $A_{Al} = 27\ \mathrm{g\,mole^{-1}}$ is the aluminum atomic mass, $\sigma \approx 1.16$ b is the neutron

Table B.1: Level of impurities in the boron oxide beam stop. (Lot#A3015)

Material	Impurity level x, (ppm)
Al	< 0.75
Ca	< 0.5
Cr	< 0.05
Cu	< 0.02
Fe	< 0.25
Mg	< 0.1
Mn	< 0.02
Na	< 0.15
Ni	< 0.02
Pb	< 0.05
Si	< 0.04
Zn	< 0.04

absorption cross section for 0.89 nm neutrons and $\tau_{Al} = 195$ s is the aluminum lifetime. Neutron activation of the ^{27}Al leads to the emission of gamma and an electron with energy up to 2.9 MeV. These decays may be partially responsible for the time-varying backgrounds observed in neutron trapping experiment.